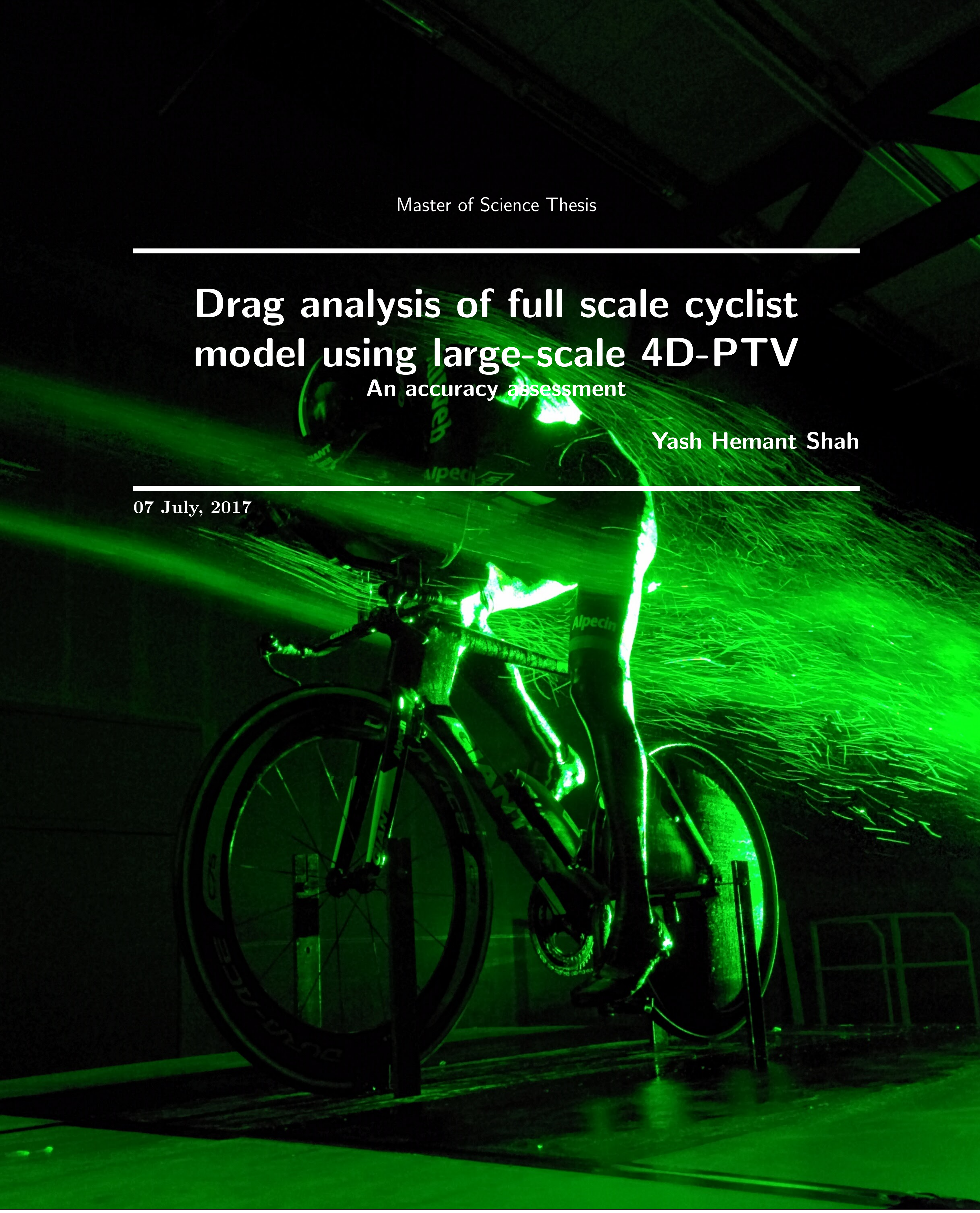

Master of Science Thesis

Drag analysis of full scale cyclist model using large-scale 4D-PTV

An accuracy assessment

Yash Hemant Shah

07 July, 2017

Aerodynamics

TUDelft

Faculty of Aerospace Engineering

Delft University of Technology

Drag analysis of full scale cyclist model using large scale 4D-PTV

An accuracy assessment

by

YASH HEMANT SHAH

to obtain the degree of Master of Science
at the Delft University of Technology,
to be defended publicly on Friday July 7, 2017 at 09:30 AM.

Student number:	4453255		
Project duration:	October 17, 2016 – July 7, 2017		
Thesis committee:	Prof. Dr. Ir. F. Scarano,	TU Delft-Aerodynamics	
	Dr. A. Sciacchitano,	TU Delft-Aerodynamics	supervisor
	Dr. B. W. van Oudheusden,	TU Delft-Aerodynamics	
	Ir. W. A. Nando Timmer,	TU Delft-Wind Energy	
	Ir. W. Terra,	TU Delft-Aerodynamics	supervisor

Delft University of Technology

Front cover page image credits: Wouter Terra

Preface

Master's in aerodynamics at a highly reputed University such as the TU Delft was a dream for me. I am highly grateful to my parents for supporting me in pursuing this dream despite the difficult conditions at home. In the past two years I have learnt some of the most interesting concepts in aerodynamics and experienced them through my experiments with immense enthusiasm. But, not a moment has passed by when I have not missed them in this exciting journey. This thesis is a culmination of all the efforts taken by me and all those who have been a part of this unforgettable experience over the past 9 months. I would like to dedicate this thesis to my parents Mr. Hemant Shah and Mrs. Manasi Shah.

I would like to express my deepest gratitude to my supervisors Dr. Andrea Sciacchitano and Mr. Wouter Terra for giving me this opportunity to work on one of the most exciting topics in the company of the leading experts in the field of PIV. I also thank them for involving me in the conference paper, wind tunnel tests of Team Sunweb and the research exhibition at TU Delft. I am grateful to Prof. Scarano and all the members of the Large scale PIV group for including me in the group and providing their valuable inputs and assistance during the course of this thesis. Special mention for my dear colleagues Constantin, Alexander and Kahin for their most valuable opinions and resourcefulness.

I would like to thank Peter Duyndam, Nico van Beek, Frits Donker, Dennis Bruikman, Henk-Jan, Stefan Bernardy, Colette Russo and rest of the support staff at the Aerodynamics Lab. for their help with setting up the test bench and easing out the daily activities for me.

Finally, the numerous friends that I made during the past two years deserve a mention. Without them life after working hours would be utterly boring. Anil, Chandrashekhar, Priyanshu, Subhajeet, Nga, Yash Raka, Sumedh, Sagar, Prateek and all the others, thank you for being there and keeping my spirits up.

YASH HEMANT SHAH
Delft, July 2017

Abstract

Laser diagnostic techniques such as Particle Image Velocimetry and Particle Tracking Velocimetry to measure the flow of a fluid around an object have been in prevalence for a few decades. Typically, the fluid, whose motion is of interest, is seeded with micron scale particles and illuminated with a laser. Due to scattering inefficiencies of these micron scale particles the maximum measurement volumes were about a few litres. Development of the neutrally buoyant sub-millimetre scale Helium-Filled Soap Bubbles allows for much larger scattering cross-sections thus enabling large-scale measurements in air [11].

Large scale Particle Tracking Velocimetry has been used to study the flow in the wake of a cyclist at typical time-trial speeds. A novel PTV algorithm known as Shake-The-Box (STB) [61] has been used to obtain the particle tracks from the images acquired in a thin volume in the cyclist's wake using the wake-scanning method. The Lagrangian particle tracking technique was found to be more accurate than the Time Resolved Tomographic PIV through another experiment. Particularly for large field of views involving scanning at different positions, it produces whole-field results free from the boundary effects that arise between different positions of the scans. This yields accurate velocity components and their gradients that are crucial for pressure reconstruction.

Flow-field results from 4D-PTV show that the wake structure is similar to those found in the literature. Two large regions of momentum deficit are present, one behind the thighs and one near the lower legs and the wheel axis. Furthermore, they reveal the presence of some vortices which were not reported previously. Based on the observed signs of the vortices the points of origination of these vortices are identified based on separation mechanisms. There is a good agreement in the flow-field results with the literature. Pressure fields reconstructed from the velocity flow-field show low pressure pockets in the regions of the vortex cores and separated flow over the lower back.

Wake flow-field is utilised to compute the drag using the control volume approach [73] and compared with the drag forces obtained from an external balance measurement to obtain the accuracy of large scale 4D-PTV. In total, five measurements at different velocities in the range of $13 m/s$ to $15 m/s$ are analysed. The accuracy of the drag estimates from 4D-PTV is obtained within 5%. Out of the three terms of the drag force, the momentum term contributes approximately 95% and the contribution from the pressure term is less than 0.3%. Rest is contributed by the Reynolds stresses in streamwise direction. Almost all the variation in the drag force comes from the momentum term.

Contents

Nomenclature

α	Angle of attack of torso with flow direction	deg
δ_z	Focal depth	m
ϵ_N	Nozzle blockage correction factor	-
ϵ_s	Jet expansion correction factor	-
λ	Wavelength of laser light	m
μ	Dynamic viscosity of air	kg/ms
ν	Kinematic viscosity of air	m^2/s
$\overline{u},\overline{v},\overline{w}$	Time averaged velocity components	m/s
ρ	Density	kg/m^3
ρ_f	Fluid density	kg/m^3
ρ_p	Tracer particle density	kg/m^3
σ_w	Standard deviation in the streamwise velocity	m/s
τ_f	Flow characteristic time	s
τ_p	Tracer particle response time	s
θ	Crank angle	deg
θ_x	Pitch angle	deg
θ_y	Yaw angle	deg
$\vec{\omega}_x,\vec{\omega}_y,\vec{\omega}_z$	Vorticity components in x, y and z respectively	$1/s$
$\vec{n}$	Normal vector	-
$\vec{u},\vec{v},\vec{w}$	Velocity components in x, y and z respectively	m/s
A	Frontal area	m^2
a	Poisson matrix	-
C_D	Drag coefficient	-
$C_D A_{bal}$	Drag area measured by balance measurements	m^2
$C_D A_{PTV}$	Drag area measured by 4D-PTV	m^2
C_p	Coefficient of pressure	-
C_{rr1}, C_{rr2}	Coefficients of rolling resistance	-
D	Diameter of sphere/cylinder	m
d_p	Tracer particle diameter	m
$f_\#$	f-number	-

f_c	Focal length of objective	m
f_s	Sampling frequency	$1/s$
f_{acq}	Acquisition frequency	$1/s$
$F_{Drag_{bal}}$	Drag force measured by balance measurements	N
$F_{Drag_{mom}}$	Momentum term of Drag equation	N
$F_{Drag_{Pr}}$	Pressure term of Drag equation	N
$F_{Drag_{PTV}}$	Drag force measured by4D-PTV	N
$F_{Drag_{RS}}$	Reynolds stress term of Drag equation	N
F_{Drag}	Drag force	N
F_{fr1}, F_{fr2}	Rolling friction force	N
F_{N1}, F_{N2}	Normal force	N
L_x	Length of Measurement plane	m
l_x	Length of camera sensor	m
M	Magnification	-
N	Number of samples considered for time-averaging	-
p	Static pressure	N/m^2
p_∞	Freestream pressure	N/m^2
PPE	Pressure Poisson Equation	-
Q	Q-criterion	-
$q_{\infty_{PTV}}$	Dynamic pressure measured at measurement plane	N/m^2
Re	Reynolds Number	-
Re_{crit}	Critical Reynolds Number	-
Re_D	Reynolds Number based on diameter D	-
Re_{TT}	Reynolds Number for time-trialists	-
RHS	Right hand side of discretised PPE	-
S_k	Stokes Number	-
t	Time	s
u', v', w'	Fluctuating part of velocity components respectively	m/s
V_∞	Freestream velocity	m/s
W_∞	Corrected freestream velocity on incoming plane	m/s
$W_{\infty_{OJF}}$	Freestream velocity measured near tunnel exit	m/s
$W_{\infty_{PTV}}$	Freestream velocity on measurement plane	m/s
X_M	Mie's parameter	-
Z_0	Distance from lens to Measurement Plane	m
z_0	Distance from lens to Image Plane	m

List of Figures

List of Tables

1

Introduction

Cycling, at the highest level of the sport, is a combination of speed and endurance. Road cycling races, such as the Tour de France and Giro d'Italia that span for more than three weeks and cover roughly 3500 km and 2500 km respectively, test the limits of the cyclist's physical and mental fitness. To remain competitive at this level it is crucial to take the aid of science and technology in order to have an upper hand over other athletes. Realizing this, the cyclists have utilized the abundance of technological advancements made in the field of cycling and have continuously raised the bar for the sport. In the past 40 years, the top speeds achieved at the Tour de France has steadily risen by almost 20%. In fact, they are about 60% higher than the speeds achieved a century ago [81]. A large portion of this enormous improvement can be attributed to the growing amount of research in cycling aerodynamics.

Figure 1.1: Tom Dumoulin (Team Sunweb, previously Team GIANT-Alpecin) in Time-trial position. Source: http://teamgiantalpecin.tumblr.com/

Long cycling tour races, such as the Tour de France, are comprised of several stages such as the flats, hilly, mountain and the time-trial stages. As a general observation, the top speeds achieved on mountainous terrains are roughly 35km/hr during the climb and 110 km/hr during descents, 45km/hr on flats and 55km/hr on the time-trials. Each stage presents a different challenge and the cyclists are required to have different strategies to stay ahead in the race. These strategies include the type of bike to be used, aerodynamic accessories and, most importantly, the position of the rider. Typically, the riders take the conventional positions of cycling which are categorized as the Upright position (tops), Dropped position (drops), the Time-trial or the Aero-position [29] and the Hill descent position (see Fig1.2). More recently, the riders have tried several innovative positions, such as the Obree's position (World Hour Record, 1993) and Froome's position (Tour de France, 2016) to gain an additional aerodynamic advantage. The aerodynamic advantage that a rider can gain plays a greater role when the speeds are higher, such as in the time-trial stages [26].

A close look at the past records of the Tour de France [81] suggests that the winning margins over a distance of approximately 3500 kilometres is barely a minute. Some of the closest wins are within differences of seconds. What is even more surprising is that the greatest differences are most likely to arise during the time-trial stage of the tour given that they are the smallest stages in terms of the distance. For instance, the famous 1989 race where Greg Lemond emerged victorious by just 8 seconds over his opponent Laurent Fignon. The difference came during the final 25 km time-trial stage, where from trailing Fignon by 50 seconds at the start Lemond with his aero-helmet and aero-tri bars raced to victory leaving Fignon 58 seconds behind. In 1968, again, the time-trial stage of 55 km made the difference where Jan Janssen gained 54 seconds during the stage to finally win by a margin of 38 seconds over Herman van Springel. Following this realization that the time-trial stage is likely to be the *make or the break* of the race, researchers have turned their attention to the time-trial position in the recent past.

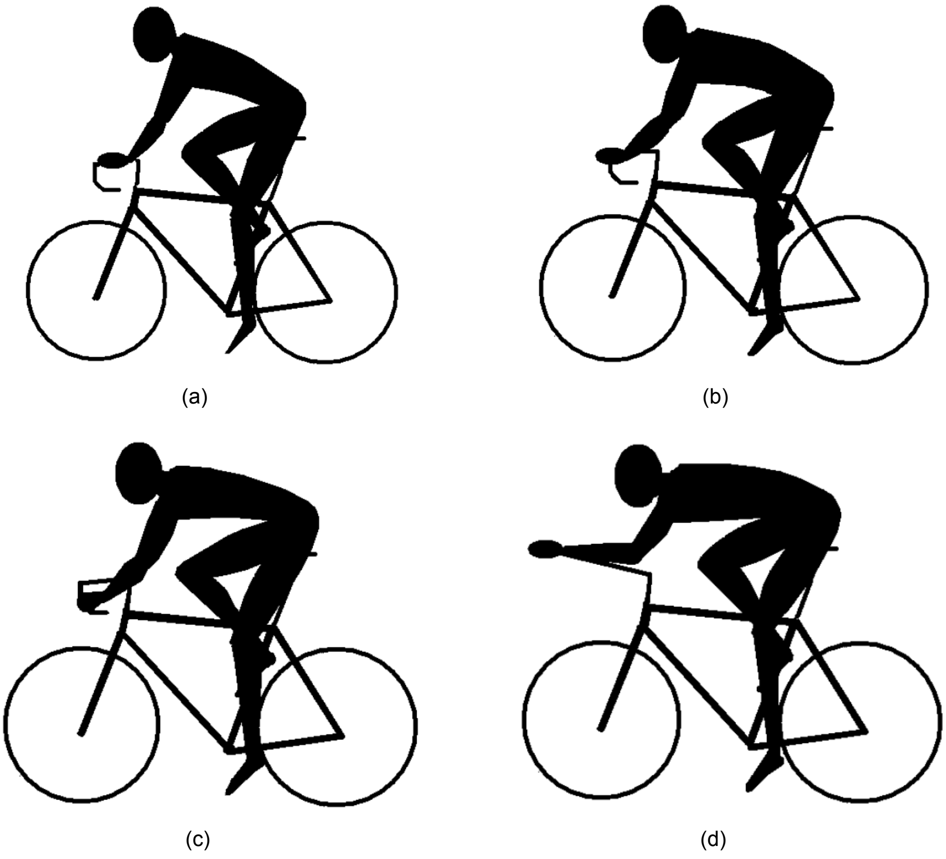
(a) (b) (c) (d)

Figure 1.2: (a) Upright Position (b) Hoods (c) Drops (d) Time-trial position. Adapted from Gibertini et.al.[26]

1.1. Cycling Aerodynamics

Drag of a cyclist

The force exerted in the streamwise direction on a body in relative motion with a surrounding fluid is known as the drag force. In this case, a cyclist moving relative to the surrounding air at a speed of V_∞ is acted upon by an aerodynamic drag force denoted by F_{Drag} (Fig.1.3). In reality, this force acts on the cyclist at the center of pressure, but for simplicity it is shown at the center of gravity. Further, the aerodynamic lift and side forces are also neglected as the drag force is of primary interest.

The drag force is given by [3]:

$$F_{Drag} = \frac{1}{2}\rho V_\infty^2 C_D A \tag{1.1}$$

Here, ρ is the density of air, V_∞ is the relative velocity of air with respect to the cyclist

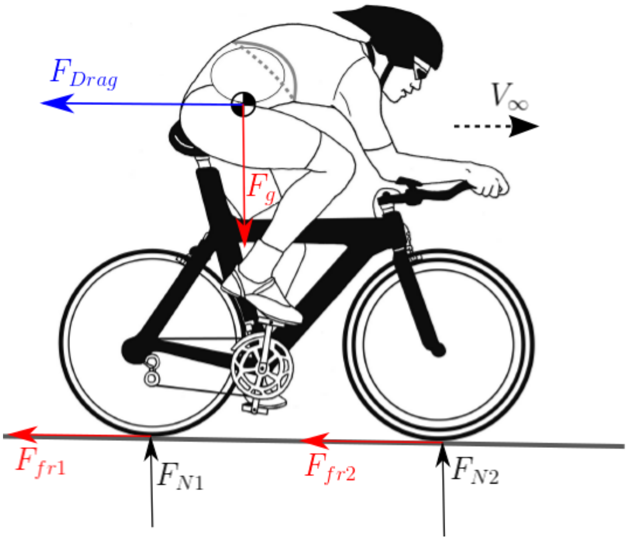

Figure 1.3: Free body diagram of a cyclist. Sketch of cyclist adapted from URL: https://goo.gl/cZh7GP

(parallel to the ground), C_D is a dimensionless number called the drag coefficient and A is the frontal area of the cyclist. The drag coefficient and frontal area, both, depend on the position of the cyclist. Therefore, the term C_DA (drag area) is a useful quantity while comparing different cycling positions. Table 1.1 shows the variation of the drag area, drag force and required power output for different positions of the cyclist. F_{Drag} is obtained from C_DA using Eq. 1.1 and $Power = F_{Drag}V_\infty$ is obtained at a speed of $14m/s$. From this experimental data it is clear that the aerodynamic benefit for the time-trial position can be as high as 12% with respect to the upright position. (Note, that the power calculated here does not represent the actual power that the rider must put in since this neglects the mechanical efficiencies of the bike and rolling friction ($F_{fr1} = C_{rr1}F_{N1}$ & $F_{fr2} = C_{rr2}F_{N2}$, using first approximation) from the ground. $C_{rr1} = C_{rr2} = 0.0023$ [26] are the coefficients of rolling resistance including bearing and tire losses. This shows that more than 90% of the force is aerodynamic drag for a 75kg time-trialist. The friction terms can be assumed constant and the differences in power arise solely from the aerodynamic drag force.)

Position	C_DA [m^2]	F_{Drag} [N]	Power [W]
Upright	0.299	35.89	502.46
Drops	0.276	33.13	463.82
Time-Trial	0.262	31.45	440.3
Obree's	0.216	25.93	363.02

Table 1.1: Preview of typical C_DA values for different positions obtained through in field experiments by Grappe et. al [29]. Drag force (F_{Drag}) and Power are computed at a speed of $14m/s$.

The flow around a cyclist can be compared to the flow around other bluff-bodies such as cylinders and spheres, thus making it a part of the widely studied branch of aerodynamics known as the bluff-body aerodynamics. Eventhough, a large portion of the bike frame and handlebars are streamlined for professional cycling, the drag coefficient C_D of cyclists has been previously measured to be very close to 1 as found for other bluff bodies [26].

Apart from the position of the cyclist, the C_D also varies weakly with the velocity V_∞, or more appropriately the Reynolds Number, defined as $Re = V_\infty D/\nu$. Here, D, a characteristic length, is the diameter of the cylinder and ν is the kinematic viscosity of air. At typical time-trial speeds, the Reynolds Numbers (Re_{TT}) are approximately in the range 2×10^5 to 3×10^5 based on the width of the hips of the cyclist (as the diameter, D). Fig. 1.4 shows that there is a minute variation in the drag coefficient of a cylinder in the aforementioned range. This variation is commonly referred to as the Reynolds Number effect in experimental aerodynamics. Fig. 1.4 also shows the “drag crisis” (shown by blue dotted line) experienced by the object at a slightly higher Reynolds Number than Re_{TT} known as the critical Reynolds Number (Re_{crit}). At this Reynolds Number, the drag coefficient suddenly drops as the boundary layer undergoes an early transition and the wake becomes narrower due to delayed separation. It is beneficial for the cyclists to achieve the critical Reynolds Number by either increasing their speed or by strategically placing roughness elements on their cycling suits.

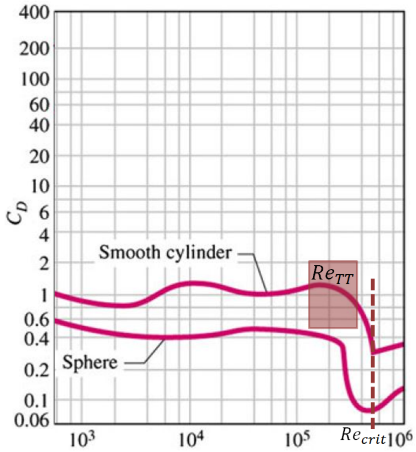

Figure 1.4: Variation of drag coefficient C_D with Reynolds Number for a smooth cylinder and sphere. Adapted from Flay [23], original work by Cengel et.al. [12]. Note, the plot has been cropped to highlight only the relevant Reynolds Numbers (>1000).

Bluff body aerodynamics

A peculiar aspect of this branch of aerodynamics is that the geometries are non-streamlined and the flow undergoes separation. This leads to the formation of a large wake. The wake is a region of low pressure and slow moving air formed right behind the bluff object. The pressure difference created between the front and the rear due to the formation of this low pressure wake causes a large drag force and is known as pressure drag or form drag. In the case of bluff-bodies the pressure drag is the most dominant component of the drag force, the other component being friction drag. Friction drag arises due to the viscous nature of the air. Fig. 2.9 shows that the pressure drag increases rapidly as the bluffness (thickness ratio D/L) increases. If the thickness ratio becomes equal to 1, the object takes the shape of a cylinder. At a Reynolds Number of 4×10^4, the drag coefficient (C_D) of a cylinder is 1.2 and the contribution from friction drag is negligible [3].

As mentioned earlier, the flow over a sphere or a cylinder undergoes separation leading to the formation of a low pressure wake (Fig. 1.6(a)) with unsteady motions. The unsteady motions are typically of the form of a series of vortices which are convected in the downstream direction. Flow visualization studies on cylinders (Fig. 1.6(b)) clearly show the formation of an unsteady wake (where the streamlines are no more visible). Further, it also shows the periodic movement of the wake in the lateral direction as it convects downstream.

These flow features are also observed in the case of cycling aerodynamics as the cyclist’s body and limbs are almost cylindrical in shape. As the torso of the cyclist gets more aligned with the flow (such as Fig. 1.2(d)) it reduces not only the size of the wake but also the amount of unsteadiness induced in the flow. Thus, such positions lead to a massive reduction in the aerodynamic drag. This fact was also verified by by Grappe et.al. [29] where they concluded that the drag area decreased as the trunk was made more horizontal.

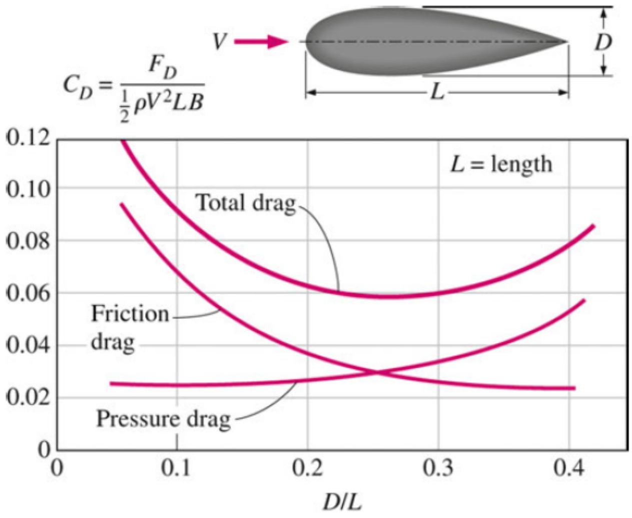

Figure 1.5: Variation of the components of the drag force with the increase in bluffness of an object. Here, the thickness of a streamlined strut is increased with respect to the chord at $Re = 4 \times 10^4$. Note, B is along the width of the strut aligned perpendicular to the plane of the paper. Adapted from Flay [23], original work by Cengel et.al. [12]

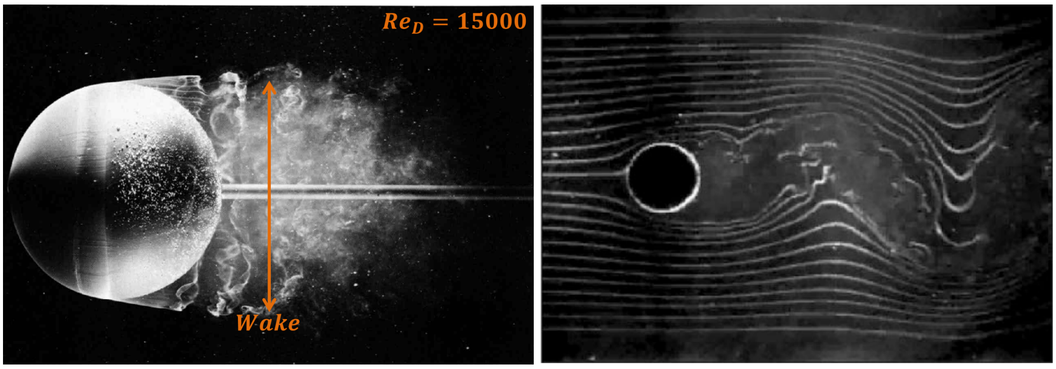

(a) (b)

Figure 1.6: (a) Flow over a sphere undergoes laminar separation and forms a wake (Reynolds Number 15000) Reproduced from van Dyke 1982 [71] Courtesy: ONERA (b) Flow visualization studies performed on cylinder showing laminar separation and formation of Kármán vortex street. Adapted from Cengel et.al. [12], original work by Homsey et.al. [34]

1.2. Drag measurement studies

Aerodynamic research using wind tunnels on cycling dates as far back as the early 50's when Kawamura [38] tested cyclists in upright position and obtained a drag coefficient (C_D) of 0.992. Since then researchers have used a range of measurement techniques from measuring oxygen consumption [18, 56] to towing cyclists in open air [20]. Several studies using other field measurement techniques such as the deceleration method and the dynamometric had been performed prior to that, however, their accuracy is questionable [29]. Thereafter, a wealth of research has been carried out in the wind tunnels on various postures, speeds, bike accessories and apparels with the intention of measuring and reducing the aerodynamic drag.

Kyle and Burke [43] performed exhaustive studies on improving the aerodynamics of the bicycle and the cyclist's posture. Their finding was that most of the aerodynamic drag was caused due to the cyclist whereas the bike contributed about 31%-39% depending on the position of the cyclist. Considering the major design changes of the race bikes in the late

90's, such as streamlining of frame parts, wheels and spokes, and subsequent improvement over the years, the contribution of the drag from the bike would be lower today. Streamlining of bike frame and have resulted in the reduction of the drag by at least 4 N according to the tests performed at California Institute of Technology, 1986 and Texas A&M, 1990 [10]. Garcia-Lopez et. al. [24] too have reported their findings on the drag area of the bike (without the cyclist) to be 0.122 m^2 which is about 35% of the maximum drag area found in that study. These values, however, do not consider the effect of the presence of cyclist and thus they should be only considered as rough estimates. Their study also found that the benefit of using a aero-helmet was applicable only for some cyclists whereas for others it either had negative effect or no effect at all. Although, it can be speculated that the negative effects may be due to a non-optimal head position maintained by the cyclist.

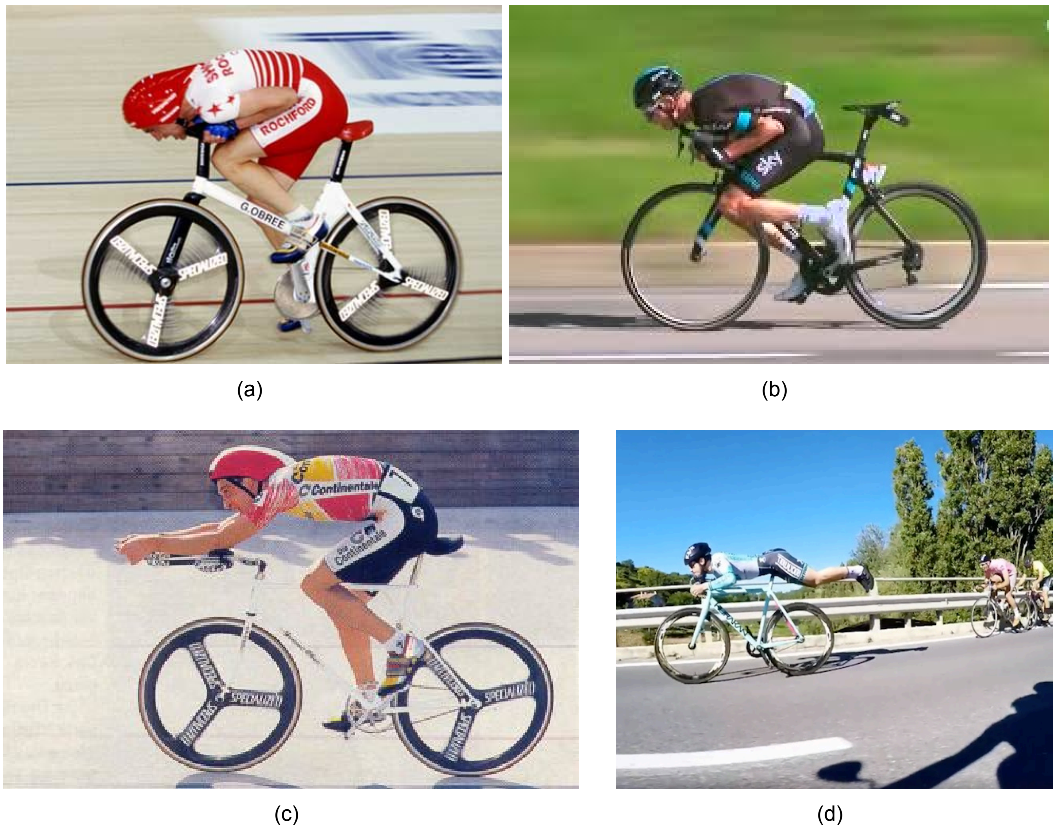

(a) (b)

(c) (d)

Figure 1.7: Extreme aerodynamic positions (a) Obree's position, 1993 (b) Froome's position, 2016 (c) Superman position - Obree, 1995. Source (a,b,c):http://www.cyclingweekly.com (d) Full Superman position (cyclist unknown) Credit (d): DailyMail UK

Studies on helmets and clothing [7, 44, 45] have shown that aero-helmets reduce the drag by about 1 N (roughly 15 watts at TT speed) as compared to wearing no helmets. Lycra skin-tight suits with long sleeves were found to have drag savings of up to 3 N (roughly 45 watts) as compared to polypropylene suits [10]. Brownlie et. al.[8] also showed the benefit of carefully placing roughness elements on the suit to force the transition of the flow over the limbs causing the size of the wake to reduce thereby reducing the drag. Similar studies were performed by Terra et.al. at TU Delft [68] using a cylinder wrapped with fabrics consisting of roughness elements. Drag reduction of almost 30% was found. Streamlined shoes with smooth upper surface are known to reduce the drag by approximately 2 N (30 watts) as compared to the standard strapped shoes [42].

Given the best combination of the accessories for a particular cyclist, the room for reduction of drag still lies in the position that the rider takes. Reducing the combined frontal area of the rider and the bike can always reduce the aerodynamic drag. In this regard, the extreme positions such as Obree's position, Superman position or the Full Superman position are good examples (see Fig. 1.7). Apart from these exceptions (most of them are banned by the Union Cycliste Internationale), the cyclist's position may be optimized by maintaining the head, elbows and arm positions such that they have minimum frontal area. The arch made by the back is also critical. The structure of the bike is closely related to the position that a rider can take. Thus, an adequate attention is required for optimizing the positions of the saddle, handlebars and arm-rests for each rider individually.

1.3. Flow visualization studies

Previous drag reduction studies were carried out primarily using the force balance in a wind tunnel. This method of testing is one of the most accurate one. However, it requires a large number of measurements, by means of extensive parameter sweeps, to optimize the position of rider individually. Availability of more information in terms of the flow variation with changes in accessories and positions can help to alleviate these time losses and improve the optimization process. With the present state of art of flow measurement techniques, it is possible to not only visualize the flow but also derive the forces from it.

There have been very few studies where quantitative flow visualization has been performed on a large-scale. One of the first such study was done by Crouch et.al. [16] using the conventional flow measurement techniques on a full-scale dynamic mannequin (movable legs). They used four hole dynamic pressure probes for the wake measurement over the upper body as they expected large-scale flow structures to be present only in that region. In total 32 complete wake measurements were carried out at the 5 downstream locations in the wake (starting from the trailing edge of the helmet going up to a torso chord behind the saddle) at different leg positions. Each wake plane contained on an average 1000 measurement points giving a resolution of 10mm to 20mm in various positions in the wake (Fig.1.9(a)). The results clearly showed the presence of various flow structures such as hip vortices (Fig.1.8) and roll-up behind the helmet (Fig.1.9(b)).

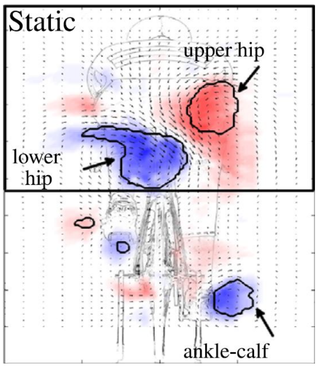

Figure 1.8: Wake measurements by Crouch et.al. [14–16] for the cyclist in the time-trial position with asymmetrical leg position (Right leg down). The bold-box shows the measurement region from Crouch et.al. [16]

Surface pressure measurements were carried out with the help of 125 pressure taps on the back of the mannequin in order to compute the pressure drag component. The drag area was obtained from the flow field data with the wake-integral approach and showed excellent agreement on the variation with the crank angle as compared to the force balance. Due to the absence of data in the lower part of the wake the overall drag area values were about 25% lower than those obtained from the force balance. In order to visualize the complete wake, they conducted similar measurements in a later study [15]. Drag areas obtained with the wake integral method in that study were within 3% of the balance measurements. Further, they revealed the presence of vortical structures in the lower part of the body including the ankle-calf vortex from the stretched leg. Since the dynamic pressure probes are intrusive and have a limited measurement zone (45° forward facing cone), they are not well suited for capturing the highly three-dimensional topology such as in this case. Furthermore, traversing of a pressure probe and acquisition of unsteady data for more than 1000 measurement points is a time-consuming process.

The same group has also conducted PIV experiments on 1:4.5 scaled cycling model using a water tunnel [17]. However, the Reynolds Numbers in this experiment were an order of magnitude less than the full-scale model at typical time-trial speeds. The flow-fields for different leg positions were observed to be qualitatively comparable to the full-scale tests from the earlier study [16]. To obtain an accurate quantitative estimate of the drag force and C_dA from flow measurement, the scale-down approach might not be suitable as the Reynolds Number effects are appreciable. Furthermore, surface roughness, which is critical in determining the separation points (and therefore the size of the wake), cannot be scaled down easily.

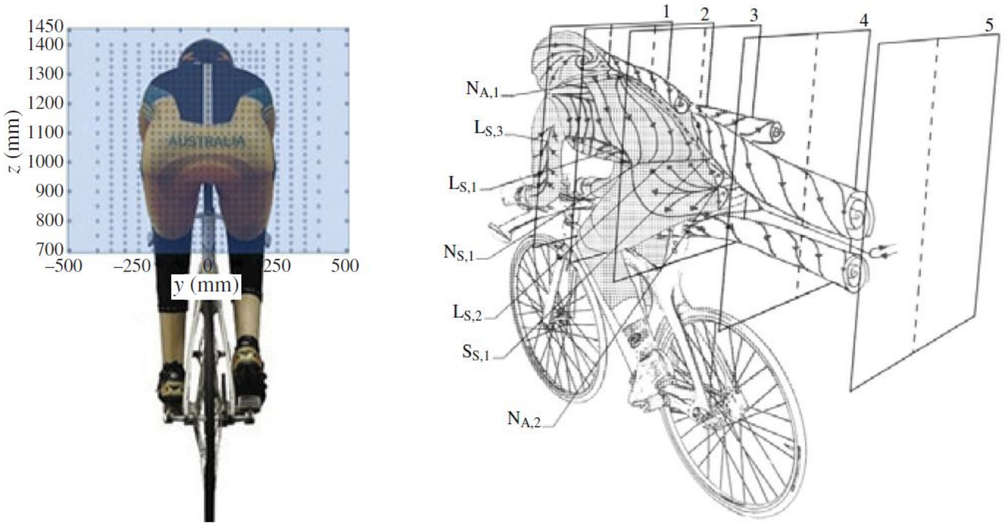

(a) (b)

Figure 1.9: (a) Measurement plane dimensions and wake survey measurement points (b) Flow topology of the streamwise vortex structures. Reproduced from Crouch et. al. [16]

Another study with Tomographic PIV was recently performed at TU Delft. It was used to capture the complete wake of a 3D printed static full-scale cycling mannequin in the time-trial position at 4m/s (14.4km/hr)[67]. The legs were oriented in the asymmetrical position, with the left-leg stretched down. A thin volume (30 mm in thickness) was illuminated with a laser and the particles flowing through the volume were captured in double frame mode by 3 cameras positioned far downstream. The results were found to be in agreement with those of Crouch et. al [16] as the hip vortices were observed in similar locations (Fig.1.10). These results also showed the presence of vortices from the feet for the first time, as they were not available from the data obtained by Crouch et.al.[16]. Another notable observation from Fig.1.8 and Fig.1.10(a) is that the stronger of the two hip vortices occurs on the side of the stretched leg.

An advantage was that PIV allowed for similar resolution or even finer in certain locations as compared to the resolutions obtained by Crouch et.al. [16]. The drag force computed from the PIV data using the control volume approach was within one standard deviation of the balance measurements (see Table 1.2). The drag area (C_dA) for the cycling mannequin and the time-trial bike used in these experiments is 0.244.

Contributions are evaluated by considering sum of absolute values of individual terms. For example, contribution of $F_{Drag_{mom}}$ is evaluated as follows:

$$\frac{100 \times |F_{Drag_{mom}}|}{|F_{Drag_{mom}}| + |F_{Drag_{RS}}| + |F_{Drag_{Pr}}|} \tag{1.2}$$

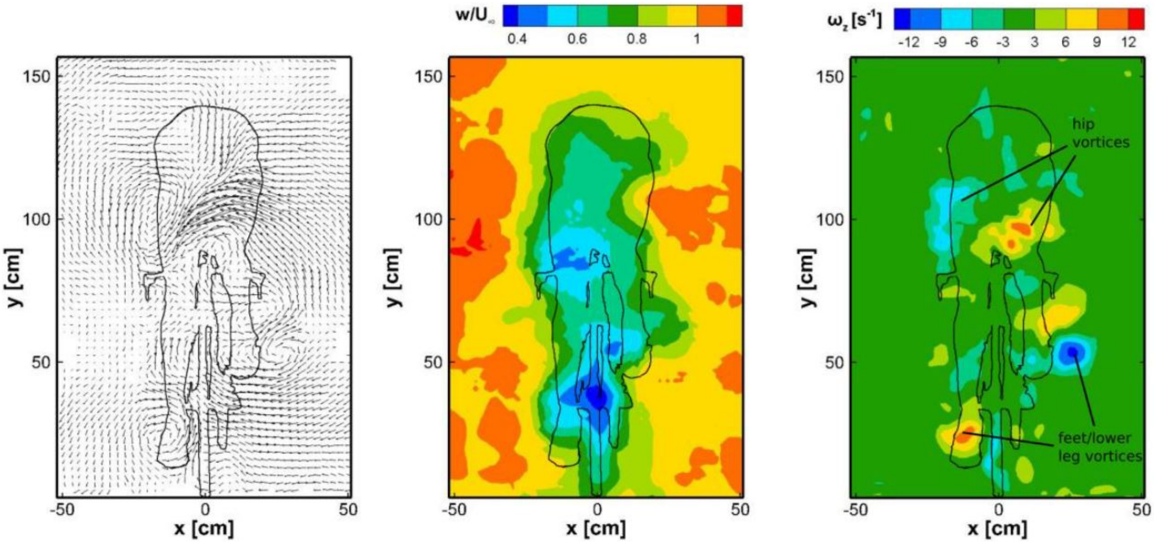

Figure 1.10: Velocity fields obtained in the wake of the cycling mannequin (a) In-plane velocities, (b) non-dimensionalized streamwise velocities (c) streamwise vorticity. Reproduced from Terra et. al. [67]

Method	F_{Drag}	$F_{Drag_{mom}}$	$F_{Drag_{Pr}}$	$F_{Drag_{RS}}$
PIV (Control Volume) [N]	2.39	2.60	0.11	-0.32
Force balance	2.38 ($\sigma_{bal} = 0.04$)	-	-	-
Contribution (%)	3.03 N (100%)	85.8	3.6	10.6

Table 1.2: Comparison of aerodynamic drag measured from PIV using the control volume approach with the force balance measurements. Reproduced from the study of Terra et.al. [67].

The flow visualization experiments clearly yield much more information for the optimization of the rider's position. The lowest streamwise velocities occur behind the hips and the stretched leg ([67]). The low velocity and high vorticity regions contribute the most to the aerodynamic drag. Large counter-rotating hip vortices are observed to be the strongest, followed by the vortices from the feet underlining the importance of hip and back positions as well as the need for using smooth upper surface for shoes.

CFD studies

Apart from experimental studies in the wind-tunnels, several researchers have studied cycling aerodynamics using the advanced computational fluid dynamics tools. One such study shown here (Fig.1.11(a)) shows the flow topology observed in the wake of the cyclist in time-trial position [30]. Fig.1.11(a) clearly show the presence of the aforementioned hip vortices. Since the right leg is stretched in this case, the vortex on the right side appears to be stronger in this case. It also shows the presence of multiple vortex pairs in the lower part, which were not visible from the studies of Crouch et. al. [16] (due to absence of data). They are partially consistent with the results of Terra et.al. [67]. Although, the results show similar structures as observed by the flow visualization studies by Crouch et.al. [16], the prediction of drag through CFD is inaccurate. Drag area is under-predicted by at least 15%. Moreover, being such a three-dimensional and complex flow, the results from CFD depend on the choice of turbulence models. Theoretically, Direct Navier-Stokes (DNS) would yield the most accurate results, however, with current state-of-the-art of such methods high-Reynolds Number flows, such as in this case, cannot be solved. Reynolds Averaged Navier-Stokes (RANS) models are widely used, but their accuracy is questionable. Until now there is not a clear consensus in the CFD community on the applicability of such models for such complex geometries. Hence, flow visualization through experimental techniques is the only reliable option for simultaneously visualizing the flow and obtaining accurate forces.

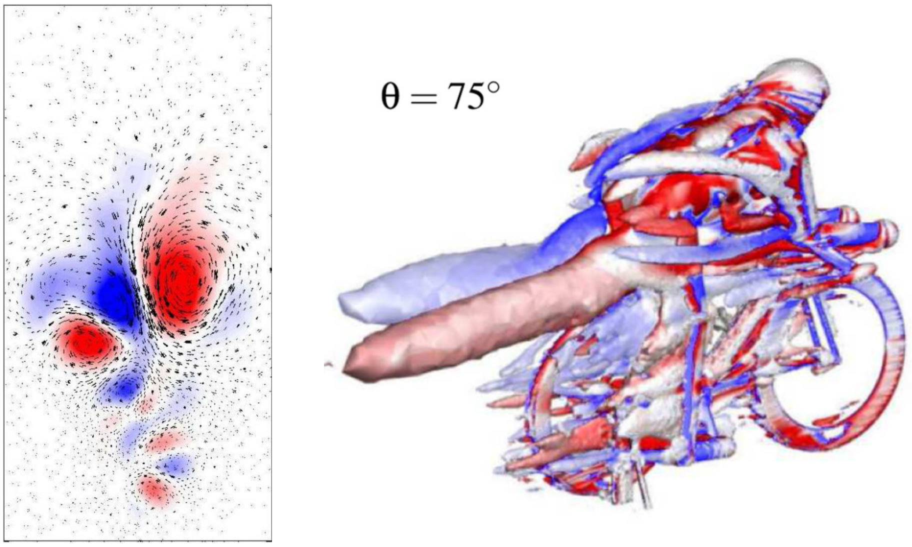

(a) (b)

Figure 1.11: (a) Steady-state results showing streamwise vorticity with cross-stream velocity vectors in the wake of a cyclist in the time-trial position with asymmetrical leg position (Right leg down). (b) Transient averaged results showing isosurfaces of Q *criterion (Eq. 4.11). Reproduced from Griffith et.al. [30]*

1.4. Research Objective and Questions

It is clear from the literature that quantitative flow visualization can aid in quicker optimization of the design due to the availability of flow information. It also presents the opportunity to innovate different solutions to minimize the drag with this added information, which is not available with the conventional balance measurements. Moreover, with the present state-of-the-art of the advanced flow measurement techniques, such as Laser diagnostics (primarily PIV and PTV), it is possible to obtain reliable and useful flow information in great detail. In light of this, the aim of this thesis is to develop an accurate and repeatable procedure for performing large-scale PIV/PTV wake measurements which enable quantitative flow visualization with minor changes in the geometry or flow parameters. Further, it is also aimed to assess the accuracy of such an approach for drag determination based on PIV/PTV.

Limited availability of the velocity flow field information around the cyclist certainly poses a problem to compare and validate the results from this thesis. Nevertheless, the reliability of the results can be tested and verified by comparing the forces, particularly the drag force, obtained from the PIV measurements with those obtained from the more conventional technique - Balance measurements. This method of verification necessitates the PIV measurements to be performed in the wake of the cyclist in order to derive the drag force using the wake survey method [9, 36] or the more generic control-volume approach [73]. Thus, the primary objective of this project is to develop a procedure to conduct accurate and repeatable wake measurements on full-scale using Laser diagnostic techniques, such as the PIV/PTV, at the standard time-trial speeds. Motivation for testing speeds and size scales for this measurement comes from the previous literature in order to achieve consistent and comparable results.

Laser diagnostics is a library of flow measurement techniques with a range of PIV techniques depending on the number of dimensions and velocity components required. While, the wake measurements require the volume to cover the complete wake (in X and Y) the computation of the drag force requires the measurement of the streamwise velocity (in Z). The first condition, by default, gives us 2 velocity components (U and V respectively) and the second condition requires the measurement to be a 3 component (3C) one. Michaelis and Wieneke [50] studied the comparison between Tomographic PIV (3D-3C) and Stereoscopic PIV (2D-3C) and concluded *"Tomographic PIV seems to be a more accurate measurement technique than stereo PIV, when applied for thin volumes and turbulent flow"*. Furthermore, Tomographic PIV allows for the evaluation of velocity and pressure gradients even within a thin volume which are important for the contribution of the pressure term in the total drag [73]. The review paper by Scarano [58] clearly demonstrates the advantages and the versatility of the Tomographic PIV in the modern day quantitative flow visualization experiments. Particularly in the case of bluff-body aerodynamics, such as cylinders, Tomographic PIV has shown to produce results with exceptional detail [22, 51]. Thus, the aim to achieve sufficient accuracy and reliability of the drag force motivates the need for 3D-3C measurements.

Recent developments in the Laser diagnostic techniques such as the Tomographic Particle Tracking Velocimetry (4D-PTV) also show immense promise in this direction. "Shake The Box" (STB) [61], a novel 4D-PTV method, has received increased attention from the scientific community in the field of laser based techniques in the recent times because of the unprecedented processing speeds and accuracies that it presents. Advantages of this technique over the Tomographic PIV are further elaborated in Chapter 2. Therefore, this technique has been carefully evaluated in the context of large-scale measurements and implemented in this thesis.

Objective

The objective of this research project is *to use the theory of drag estimation from Large-scale PIV/PTV measurements by measuring the flow field in the wake of a full-scale cycling mannequin with 4D-PTV techniques and to evaluate the drag force from the velocities and pressures obtained from the statistically converged time averaged flow-field measurements*. Further, it is intended *to test the sensitivity of the technique in order to measure minute drag variations by comparing the drag value obtained from PIV/PTV with the drag obtained from balance measurements upon changing the velocity within a small range.*

Research Questions

The thesis aims at answering the following research questions:

1. What is the accuracy of the drag measurements from PIV/PTV in order to resolve drag variations due to minor changes in the flow parameters such as the incoming wind speed?
2. In the context of large-scale laser based measurement techniques, which technique, PIV or PTV, is better suited for obtaining the flow-field measurement most accurately?
    a. What are the major advantages and disadvantages of each of the technique, especially in the case of large-scale measurements?
    b. With regards to the choice of the measurement technique and the required statistical convergence criteria, what parameters should be considered in the design of the experiment?
3. Which components of drag are most dominant in this case and how should they be derived from the flow-field obtained in the wake of a cyclist? What are the expected trends for drag force from analytical solutions or literature, how should the derived drag force compare with them?

Relevance

Most practical aerodynamic applications ranging from bluff bodies like a cyclist to a streamlined body such as an aircraft are large in scale. Traditionally, these bodies are scaled down in order to perform wind tunnel measurements. Typically, scaling of a model is done based on Reynolds numbers in the case of low-speed flows. It can be argued that scaled-down measurements do not always yield the true response of a full-scale body as Reynolds number similarity does not always guarantee the similarity of other parameters, such as the vortex shedding frequency in this case. Moreover, in practice, the scaling of surface roughness cannot be ensured, leading to a change in the boundary layer properties and separation locations. This causes the flow features in full-scale to be significantly different from those observed in the scaled-down measurements. Therefore, it is required that the advanced measurement techniques, such as the PIV, are developed to measure on a large-scale, ensuring reliability and accuracy of the measured flow-fields.

This thesis not only serves as a demonstration for full-scale wake measurements on the cyclist but also contributes towards the effort of developing the state-of-the-art to incorporate the large-scale measurements. Such large-scale application of Laser diagnostic techniques would be particularly relevant for the automotive, aerospace and performance sports industries. Current industrial effort towards development of sustainable means of transport largely revolves around reduction of fuel consumption. Drag measurement by means of flow visualization provides an exciting opportunity to develop novel solutions for drag reduction and thereby contribute towards that goal. Furthermore, accurate full-scale wake measurements are vital for the determination of drag and drag differences through the Ring of Fire [64] concept.

Thesis Outline

Chapter 2 describes the theory and benefits various techniques that have been utilized during the experimental campaigns for this thesis. The experimental setup used for performing the PTV and balance measurements is described in Chapter 3, followed by the data reduction techniques in Chapter 4. Chapter 5 shows the qualitative and quantitative results obtained from the measurements, and the final conclusions are addressed in Chapter 6.

2

Experimental Techniques

As argued in Chapter 1, 3D-3C laser diagnostic techniques such as Tomographic PIV or the 4D Tomographic Particle Tracking Velocimetry with Shake The Box [61] are expected to be the most suitable quantitative flow visualization techniques for large-scale measurements. This chapter further delineates the reasons for the choice of these techniques, their working principles and the results that are expected to come out of the experiments.

The choice between PIV and PTV is made on the basis of results from another experiment with a transiting sphere through a tunnel filled with Helium-filled Soap Bubbles ("Ring of Fire" concept [64]). These results can be found in Appendix A. Further, both the techniques have been compared on numerous aspects, such as processing speeds and accuracy, to enable this choice.

The experimental setup for Tomographic PIV and 4D-PTV are similar. Sections 2.1, 2.2 and 2.3 describe the imaging system, tracer particles and the illumination systems respectively. Sections 2.4 and 2.5 discuss the working principles of Tomographic PIV and 4D-PTV respectively. The data processing techniques used for each measurement techniques is also explained in the subsections of the respective sections. Section 2.6 discusses the methodology to determine the forces from the PIV/PTV data using the control volume approach [73]. Finally, section 2.7 briefly describes the working principle of a wind tunnel balance and its applicability to measure load variations which is particularly relevant for cycling aerodynamics.

2.1. Imaging System

The tomographic imaging system typically consists of 3 or more CCD or CMOS cameras. It is preferable to use higher number of cameras for higher seeding densities [22]. All cameras are equipped with objectives (lenses) which allow the light from the measurement space to be focused on the sensor of the camera (see Fig.2.1).

Magnification of the system is expressed as

$$M = \frac{z_0}{Z_0} = \frac{l_X}{L_X} \tag{2.1}$$

In case of large-scale PIV experiments it is common to encounter magnification as low as 0.01. This also means that the cameras have to be placed almost 100 times further than the focal length of the objectives as the focal length (f_c) is given by:

$$\frac{1}{f_c} = \frac{1}{Z_0} + \frac{1}{z_0} \Rightarrow Z_0 = f_c\left(1 + \frac{1}{M}\right) \tag{2.2}$$

Another critical parameter in the case of large-scale PIV measurements is the depth of field (ΔZ). Typically, in large-scale measurements it is difficult to achieve a large measurement depth as the laser intensity drops drastically. Therefore, a thin measurement volume needs to be chosen which is just enough to resolve the three dimensional flow-field. The focal depth (δz) needs to be at least equal to the measurement depth. The f-number ($f_{\#} = f_c/D$) controls this optical depth. Thin measurement volumes and low magnifications require smaller values for $f_{\#}$ and larger aperture diameters (D).

$$\delta z = 4.88 \cdot \lambda \cdot f_{\#}^2 \cdot \left(\frac{M+1}{M}\right)^2 \tag{2.3}$$

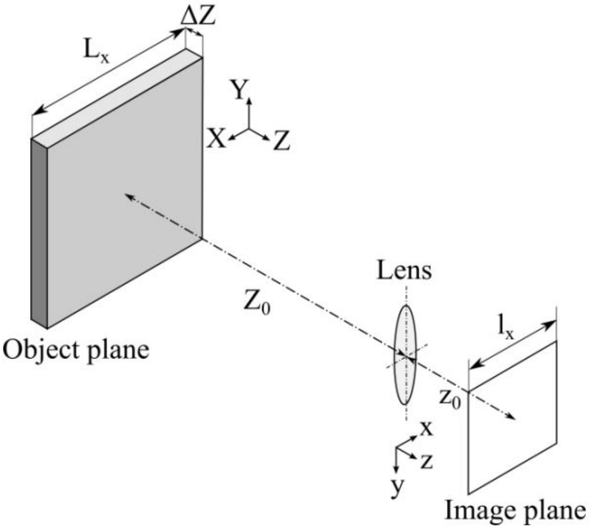

Figure 2.1: Imaging system for PIV. Reproduced from Sciacchitano 2014 [63]

The viewing angles in the range 15° to 45° are found to be optimum from previous studies of Elsinga et.al. Larger viewing angles increase the length of line of sight which leads to an increase of the number of ghost particles [22].

2.2. Tracer Particles

The choice of the tracer particles is the most critical for PIV since the ability of the tracer particle to follow the ambient flow and yet allow themselves to be tracked with the cameras determines the accuracy of the result. Firstly, properties like density and particle size are of foremost importance for the particles to have low response time (τ_p) (see Eq. 2.4, [57]).
Particle response time τ_p is given by: [57]:

$$\tau_p = \frac{d_p^2 \cdot (\rho_p - \rho_f)}{18 \cdot \mu} \tag{2.4}$$

The term $\rho_p - \rho_f$ is very small for particles having comparable densities with the working fluid. This allows for large particle diameters d_p while still keeping a low response time.

The response time of a particle is required to be lower than the flow characteristic time (τ_f) so that the velocity lag is minimized and the particle is able to follow the motions of the surrounding fluid. The Stokes number defined as $S_k = \tau_p/\tau_f$ determines the suitability of a tracer particle for a particular flow measurement. For a reliable tracing particle the Stokes Number (S_k) should be of the order of 0.1 or lower. Here, the flow characteristic time is defined as the ratio of a characteristic length scale and a velocity scale.

Secondly, the particles must also scatter the light, when illuminated, in order to capture their motion with the help of the cameras. The scattering cross-section of the particle and the scattering regime determines the amount of light a particle scatters. These parameters are directly related to the particle size, among other parameters, for spherical particles [65]. Typically, for particle sizes much greater than the wavelength (Mie's parameter $X_M = \pi d_p/\lambda >> 1$) of the illuminating light, the scattering occurs in the geometrical regime (Fig. 2.2). When the particle sizes are comparable to the wavelength, Mie scatter occurs. Further, for $d_p >> \lambda$, the scattering is stronger in 0° direction (forward scattering)[70].

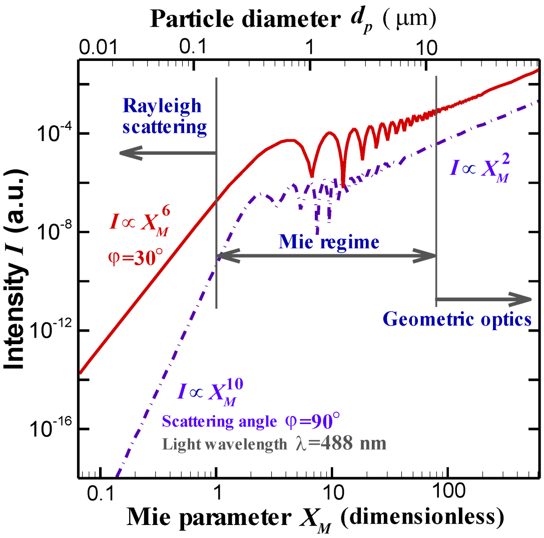

Figure 2.2: Scattering intensity as a function of Mie's parameter. Reproduced from Tu et.al. [70]

Helium-Filled Soap Bubbles (HFSB)

Earliest references to HFSB date back to 1936 [27] when they were used for flow visualization. Nowadays, the HFSB are regarded as one of the best tracer particles for PIV given their high scattering cross-section and low response time [59]. HFSB have been used in a wide variety of flow measurements, ranging from vertical axis wind turbines, delta wings and sports aerodynamics, and measurement volumes as large as $45000 cm^3$ [67]. Scarano et.al. [59] quantified the response times of the HFSB for a range of volume flow rates of the Bubble Fluid Solution (BFS) and they were typically in the order of $10\mu s$ to $40\mu s$. In the case of this setup, if the diameter of the limbs of the cyclist (roughly $0.1m$) is assumed as the characteristic length and the wind speed ($V_\infty = 14m/s$) as the characteristic velocity. This yields the flow characteristic time τ_f = 7.14ms. Thus, the Stokes number (S_k) is much lower than 0.1 in this case which makes HFSB suitable tracer particles. Moreover, the density ρ_p of the HFSB are very close to that of air, which allows these particles to be as large as sub-millimetre scales ($300\mu m$ to $400\mu m$) while maintaining a low response time (see Eq. 2.4).

More than its tracing fidelity characteristics the light scattering properties of HFSB make it attractive for the large-scale measurements. Given their large particle diameters (at least 100 times larger than DEHS), the HFSB have a tremendously high scattering cross-sections as compared to DEHS or other tracer particles. In this regime, the scattering cross-section is proportional to the square of the particle diameter and so is the scattered intensity (Fig. 2.2). This motivates the choice of the HFSB tracing particles for the large-scale measurements performed during this thesis. Bosbach et.al. [6] have shown the applicability and generation methods of HFSB for large-scale applications.

2.3. Illumination

Illumination of the measurement volume is typically achieved with Nd:YAG (Neodymium:Yttrium-Aluminium-Garnet, $\lambda = 1064nm$) or Nd:YLF(Neodymium:Yttrium-Lithium-Fluoride, $\lambda = 1053nm$) solid-state lasers since they have high pulse energies and short pulse durations [58]. They are equipped with a frequency doubler to obtain the emitted radiation in the visible regime ($\lambda = 532nm$ for Nd:YAG, $\lambda = 526nm$ for Nd:YLF). The energy carried per pulse, repetition rate and pulse durations are the critical parameters for the choice of a laser. Typically the pulse energy decreases with increasing repetition rates as shown in Fig. 2.3 [57]. Moreover, the light intensity in the measurement volume is inversely related to the thickness of the volume [58]. These factors have been reported to be the limiting ones for large-scale tomographic measurements [58]. This further adds support to the earlier statement that the measurement volumes for large-scale PIV should be restricted to volumes just thick enough to capture the three-dimensionality of the flow.

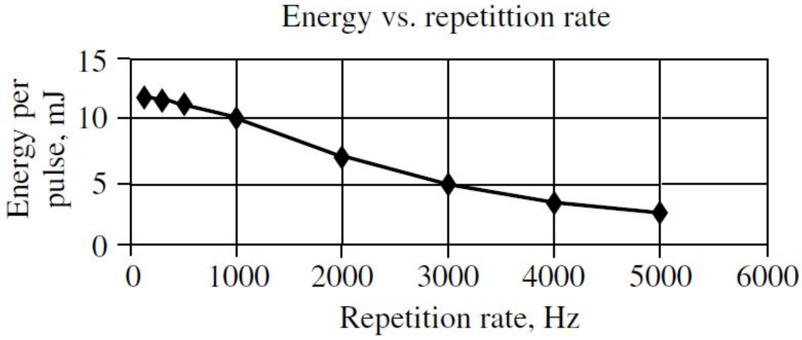

Figure 2.3: Variation of pulse energy with repetition rate of high speed PIV lasers. Reproduced from Raffel et.al. [57]

The laser system produces a circular beam of approximately $1cm$ diameter. The beam is allowed to pass through multiple spherical and cylindrical lenses and angled mirrors to illuminate the measurement volume at the required location. Spherical lenses expand (if focal length is negative, or contracts, if focal length is positive) the beam in all directions, whereas cylindrical lenses expand the beam in only one direction. Given the large FOV with relatively low thickness for large-scale PIV, large expansions of the beam are required in one direction as compared to another. Furthermore, the expansion (in both directions) is appreciable throughout the measurement volume and it affects the intensities of the particles captured at farther ends of the volume.

2.4. Tomographic Particle Image Velocimetry

Particle Image Velocimetry (PIV) is a quantitative flow measurement technique, developed in 1980's, which allows velocity measurements by illuminating and imaging tracer particles in a fluid [28]. Flow visualization in air, like all transparent fluids, is achieved by seeding the air-stream with small ($1\mu m$ to $400\mu m$ in diameter) particles and illuminating them, typically with a high powered laser. The seeding particles are chosen such that they have a relatively low time-response and can follow the surrounding fluid's motion more precisely. The motion of the illuminated particles is captured by means of one or more digital cameras (depending on the number of dimensions and velocity components required) and the displacements of the particles in subsequent frames is obtained by a cross-correlation algorithm.

Recent developments in PIV have enabled 3D-3C measurements, known as the Tomographic PIV (Tomo-PIV) [22], on the lines of the principles of tomographic reconstruction. Moreover, the development of the helium-filled soap bubbles (HFSB) [59] as tracer particles allows for large-scale Tomo-PIV measurements due to their larger scattering cross-section as compared to the conventional Di-Ethyl-Hexyl-Sebacat(DEHS) particles.

2.4.1. Working Principle of Tomographic-PIV

A tomographic measurement system consists of multiple cameras, (typically 3 or 4) for capturing different views of the measurement volume at different angles. The apertures are set such that the entire depth of the volume is in focus. Tilt adapters are used to account for the misalignment between the object midplane and the image plane (Scheimpflug condition). Geometrical calibration is performed by placing the calibration plate at several positions in the depth of the measurement volume. Further, the self-calibration procedure [78] helps to fine-tune the calibration (disparity less than 0.1 pixels). The calibration makes an accurate relation between the *object space and image space* [58]. With this imaging setup and a laser to illuminate the volume, several sets of images are acquired in double-pulsed mode or time-resolved mode as the tracer particles are flowing through the measurement volume. Each set of images is then used to reconstruct the positions of the particles based on the calibration. Once the particle positions are obtained in the 3D space at each time instant, a 3D cross-correlation algorithm yields the velocity vectors by finding 'average' displacements in each interrogation window.

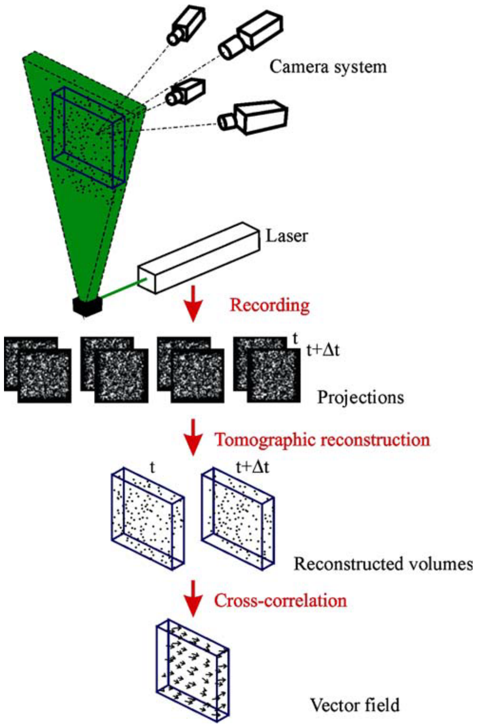

Figure 2.4: Working principle of Tomographic PIV. Reproduced from Elsinga et.al. [22]

Reconstruction Algorithms

Tomographic reconstruction is the key term here which refers to the solving of the inverse problem of generating a 3D object from a set of 2D projections [22]. Currently used tomographic reconstruction algorithms for PIV belong to the category of Algebraic methods. In this approach the measurement volume is divided into cubic elements known as 'voxels' typically with the same dimensions as of the pixels. The intensity of the light falling on the camera sensor ($I(x_i, y_i)$) is expressed as a weighted sum of the intensities of all the voxels (N_i) ($E(X_j, Y_j, Z_j)$) in the *line of sight* of the pixel as given in Eq. 2.5. The weighting coefficient ($w_{i,j}$), as shown in Fig. 2.5, is the contribution of intensity of the j^{th} voxel along the line of sight to the i^{th} projection on the sensor.

$$\sum_{j \in N_i} w_{i,j} E(X_j, Y_j, Z_j) = I(x_i, y_i) \tag{2.5}$$

A variety of tomographic reconstruction algorithms have been developed to solve Eq. 2.5. MART (Multiplicative Algebraic Reconstruction Technique) [22, 31], one of the earliest and one of the most widely used algorithm, is an iterative algorithm with a multiplicative update based on the ratio of the recorded intensity ($I(x_i, y_i)$) and that integrated along the line of sight [58]. Eq. 2.6 gives the update for k^{th} iteration of the MART algorithm. μ is a relaxation parameter.

$$E(X_j, Y_j, Z_j)^{k+1} = E(X_j, Y_j, Z_j)^k \cdot \left(\frac{I(x_i, y_i)}{\sum_{j \in N_i} w_{i,j} E(X_j, Y_j, Z_j)^k} \right)^{\mu w_{i,j}} \tag{2.6}$$

This type of reconstruction suffers from a problem of triangulating 'ghost particles' (artificial particles) which decrease the quality of the reconstruction. These ghost particles are

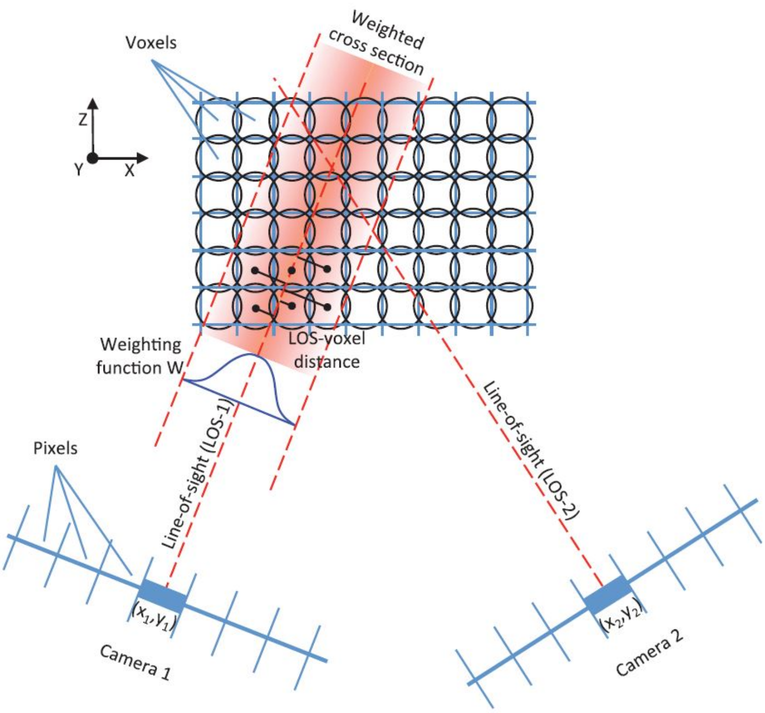

Figure 2.5: Imaging model used for tomographic reconstruction. Reproduced from Scarano 2013 [58]

formed at the intersections of the lines of sight of the cameras corresponding to the actual particles [58]. Further developments in MART algorithm such as Simultaneous-MART (SMART [4]), Motion Tracking Enhancement (MTE [53]) and Spatial Filtering (SFIT-MART [21]) provide an increase in the accuracy of the reconstruction. However, the quality of reconstruction and computational cost varies according choice of the method and they are, usually, directly related. Coupling the MART algorithm with some initiation techniques, such as the Multiplicative First Guess (MFG, [82]) and the Multiplicative Line of Sight (MLOS, [4]) provide a significant boost to its computational efficiency.

2.5. Particle Tracking Velocimetry

Particle Tracking Velocimetry (PTV) is a Lagrangian particle tracking method that was developed along with PIV, but only for low seeding densities. The experimental setup for 4D-PTV is very similar to that of Tomographic PIV, the only change being the acquisition frequency. With this technique it is possible to track the individual tracer particles by taking snapshots at a high frequency and triangulating the matching particle at each time-step. This provides increased positional accuracy and spatial resolution as compared to PIV (Fig. 2.6(b)). However, traditional PTV techniques allowed only for very low seeding densities (of the order of 0.005 ppp) since higher seeding concentrations led to a significant increase in the number of ghost particles causing positional errors [62]. One such example from an earlier PTV application to measure the wake of the cylinder is shown in Fig. 2.6(a). It shows low spatial resolution due to very low seeding concentrations.

Current developments in 3D-PTV are, therefore, largely focused on tracking particles at higher seeding concentrations. In this regard, novel particle reconstruction techniques such as Iterative Particle Reconstruction (IPR) [79] have been successfully applied for particle densities as large as 0.2 ppp. Although IPR was able to detect a high number of true particles, the number of ghost particles increased with increasing particle image density. The development of Shake-The-Box by Schanz et.al. [61] provides a solution to this problem and marks the beginning of a new era for 4D-PTV techniques (*time* being the fourth dimension).

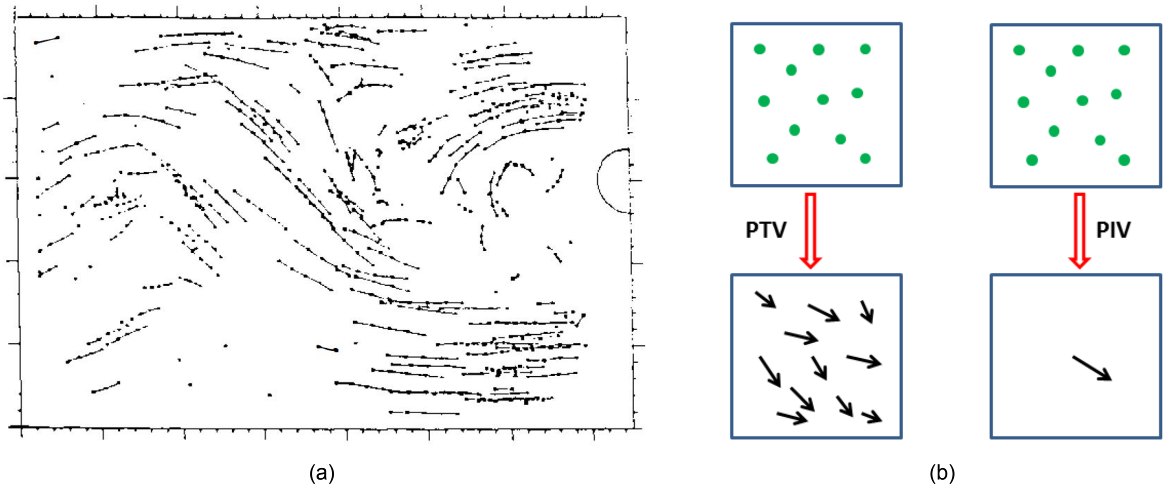

Figure 2.6: (a) Streaks of particles in the wake of a cylinder measured using PTV (multiframe/single pulse). Adapted from Adrian 1991 [1], original work by Perkins and Hunt 1989 [55]. (b) Schematic representation of spatial resolution obtained from PTV and PIV (originally published in [54]).

2.5.1. Shake-The-Box

Shake-The-Box, unlike other particle reconstruction algorithms like MART and IPR, makes use of the time-resolved information to predict the positions of the particles in subsequent time instances [61] (hence the term 4D-PTV). This approach of predicting the particle distributions and then correcting them provides a massive increase in the computational efficiency as well as accuracy as compared to traditional 3D-PTV or Tomo-PIV methods. STB works in three different phases, each of them consisting of multiple steps, to arrive to the final particle tracks. A brief description of these steps is given below. Details can be found in Schanz et.al. [62]. Prior to these steps, STB requires the generation of a calibrated Optical Transfer Function (OTF) [60]. The OTF can be computed during the Volume Self Calibration (VSC) procedure [78] using the steps described by Schanz et.al. [60].

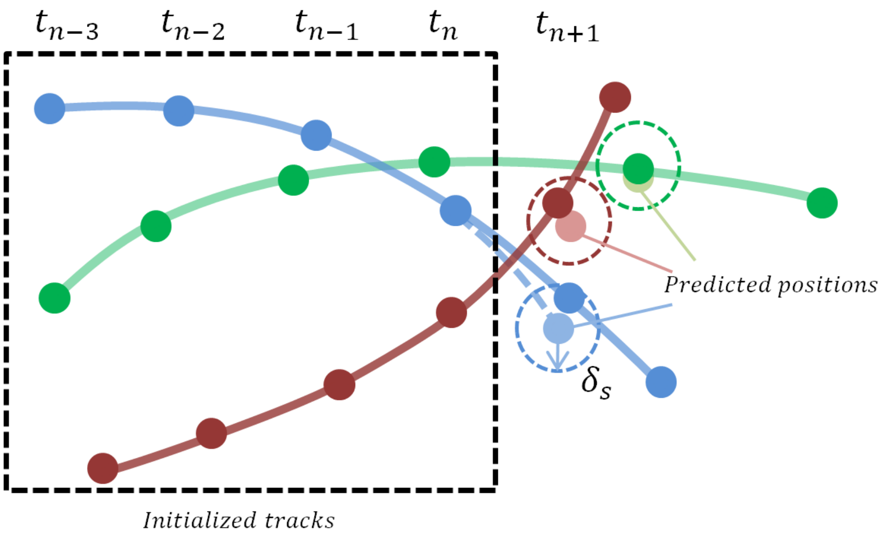

Figure 2.7: Schematic of working of Shake-The-Box after initialization.

In the (first) *initialization* phase, the particles are identified for first 4 snapshots (t_{n-3} to t_n, Fig. 2.7) using an extended IPR technique. Tracks are developed from these identified particles from consecutive frames by a matching process with the help of a search radius. Once these tracks (track length = 4) are identified, they are filtered based on velocity and acceleration limits (sanity check).

The (second) *convergence* phase consists of six important steps:

1. Prediction: The filtered track information from the initialization phase is used to predict the position of the particle at next time instant (t_{n+1}) as shown in Fig. 2.7. This step is performed using a Weiner filter [80] that extrapolates the polynomials to the next time-step.

2. Refinement: The predicted particle positions are quite close to the actual positions (within 1-2 pixels or less). This small error is corrected by using a modified version of the IPR technique ([62, 79]). This step involves moving ("shaking") the predicted particle in different directions inside a small sphere around the predicted position (shake delta δ_s) in a pre-defined manner. For each position, the particles are 'back-projected' using an *Optical Transfer Function* [60] (Fig. 2.8(a)) which yields a virtual image along with an added particle that is under consideration (I_{proj}) (see Fig. 2.8(b)). The residual intensities between the recorded image (I_{rec}) and the back-projected image ($I_{res} = I_{rec} - I_{proj}$) is minimized using the IPR algorithm as the particle is shaked in small steps. Particle position where an absolute minimum of the residual intensities is obtained corresponds to the *true* location of the particle.

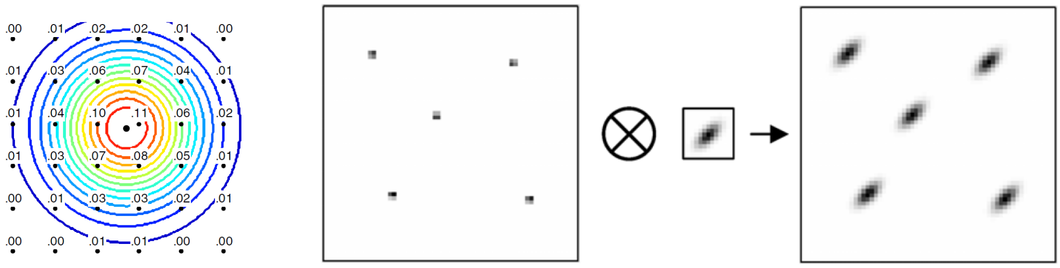

(a) (b)

Figure 2.8: (a) Optical Transfer Function: Shape of weighting functions. (b) Back-projection of particle positions through OTF to obtain virtual images. Reproduced from Schanz et.al. [60]

3. Intensity correction: Once the true locations are identified, the intensity of the new particle ($I_{P,new}$) is corrected (previously back-projected through OTF, I_P) by applying an update as in Eq. 2.7. The summations are done over a chosen window around the projected location on a particular camera.

   $$I_{P,new} = I_P \cdot \sqrt{\frac{\sum_{px}(I_{res+p})}{\sum_{px}(I_{Part})}} \tag{2.7}$$

   Ghost particles usually occur on a single camera and produce bright spots. Therefore, this step accounts for such occurrences by eliminating such locally present bright spots from the update equation, reducing the intensity of the ghost particles which are deleted in the next step.

4. Deletion: Particles are deleted if their intensity falls below a specified threshold expressed in terms of average particle intensity. In this step, most of the ghost particles having much lower intensity than the true particles are deleted.

5. Identifying new particle candidates: Most of the particles are identified and tracked using the above steps, but not all. The residual images (I_{res}) contain additional particle images . These particles are identified in this step using a triangulation procedure.

New particles lying within $1px$ radius of the existing particles are discarded. Once all the particles are triangulated, the shaking procedure is resumed to refine the positions and intensities of the newly triangulated particles as well as the existing particles. Ghost particles are simultaneously identified and deleted during these iterations.

6. Adding and deleting tracks: With the new particle candidates, additional particle tracks (of track length = 4) are identified using a predictor. The predictor is constructed from the tracked particles by computing a Gaussian-weighted average of the velocities of tracked particles found in a specified neighbourhood. Tracks are terminated at a particular time instant if the prediction for next time instant lies outside the measurement volume.

Finally (third) the *converged* phase is achieved during which all the true particles are identified and tracked until they leave the measurement volume.

2.6. Determination of drag from PIV/PTV

The integral form of the momentum equation, used by NACA (National Advisory Committee for Aeronautics) to measure the drag characteristics of airfoils during the 1930s [3], is frequently used nowadays to estimate drag forces using PIV/PTV. For this approach, a control volume needs to defined as in Fig. 2.9 surrounding the body under consideration (in this case, the cyclist).

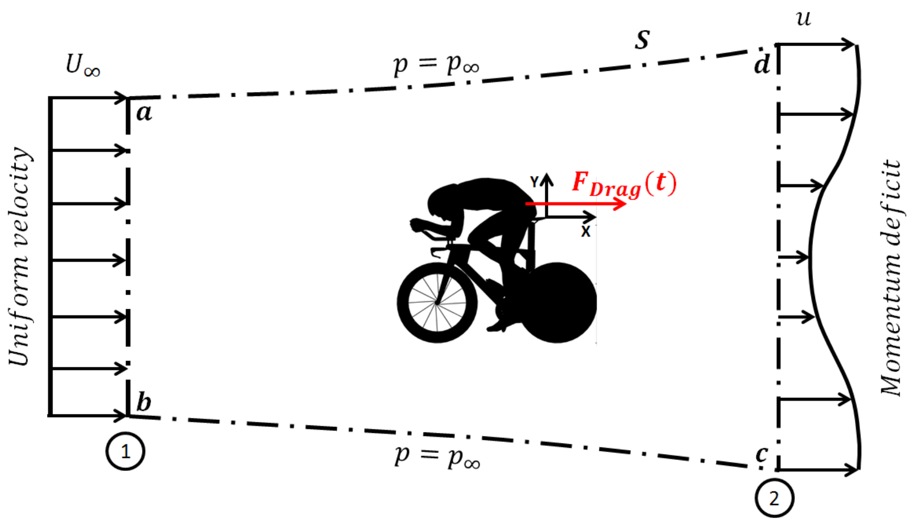

Figure 2.9: Schematic of the control-volume approach to determine drag on the cyclist.

The criteria for defining this control volume is as follows:

1. Lines ab and cd must be far upstream and downstream respectively and must be perpendicular to the flow velocity.
2. Lines ad and bc must be streamlines far away from the body such that the pressure on those lines is equal to the freestream pressure (p_∞)

2.9 only shows the control volume in 2D (with X axis aligned along the streamwise direction) but the above criteria must be satisfied in all three directions.

Since the drag force is of primary interest here, the instantaneous conservation of momentum in the control volume $abcd$ is considered along the x direction:

$$F_{Drag}(t) = -\rho \oiiint_V \frac{\partial u}{\partial t} dV - \rho \oiint_S (\vec{v}.\vec{n}) u dS - \oiint_S ((p\vec{n} - \vec{\tau} \cdot \vec{n}) dS)_x \tag{2.8}$$

Here, V is the control volume and S is the contour of the control volume as shown in Fig. 2.9. $\vec{n}$ is the outward normal vector on each side of the contour S. The incoming flow is assumed to be uniform with a velocity U_∞ and pressure p_∞. The outflow velocity profile ($\vec{u}$) is not uniform due to the formation of the wake. ρ is the density of air, $\vec{\tau}$ is the shear (viscous) stress tensor and p is the static pressure.

The viscous forces are dominant close to the body. As the control surface is taken far away in this case the contribution from the viscous terms is likely to be negligible as compared to the other terms [41].

The normal vector $\vec{n}$ is normal to the velocity $\vec{v}$ along the boundaries ad and bc. Thus, $(\vec{v} \cdot \vec{n})_{ad,bc} = 0$. Furthermore, pressure force ($\iint pdS$) is negligible along the streamlines ad and bc. Thus, Eq. 2.8 is simplified to:

$$F_{Drag}(t) = -\rho \oiiint_V \frac{\partial u}{\partial t} dV + \rho \left(\oiint_{ab} U_\infty^2 dS - \oiint_{cd} u^2 dS \right) + \left(\oiint_{ab} p_\infty dS - \oiint_{cd} p dS \right) \tag{2.9}$$

Using the conservation of mass equation for control volume (since ad and bc are streamlines), $\iint_{ab} \rho U_\infty dS = \iint_{cd} \rho u dS$. Thus, multiplying both sides by U_∞, $\iint_{ab} \rho U_\infty^2 dS = \iint_{cd} \rho U_\infty u dS$. Thus Eq. 2.9 is further simplified to:

$$F_{Drag}(t) = -\rho \oiiint_V \frac{\partial u}{\partial t} dV + \rho \oiint_{S_{wake}} (U_\infty - u) u dS + \oiint_{S_{wake}} (p_\infty - p) dS \tag{2.10}$$

Eq. 2.10 represents the instantaneous drag force acting on the cyclist. In order to derive the time-averaged force on the cyclist, which is of greater importance for deriving the drag forces in a stationary position as in this case, Eq.2.10 is subjected to Reynolds averaging.

u is decomposed as $u = \overline{u} + u'$, $\overline{u}$ is the mean flow component and u' is the fluctuating component of the velocity in the streamwise direction. The time average of the fluctuating components u' is zero by definition. The instantaneous (unsteady) term $\frac{\partial u}{\partial t}$ drops out yielding:

$$\overline{F}_{Drag} = \rho \iint_{S_{wake}} (U_\infty - \overline{u}) \overline{u} dS - \rho \iint_{S_{wake}} \overline{u'^2} dS + \iint_{S_{wake}} (p_\infty - \overline{p}) dS \tag{2.11}$$

Eq. 2.11 represents the time-averaged equation for the drag force consisting of three major components:

1. Momentum term: $\rho \iint_{S_{wake}} (U_\infty - \overline{u}) \overline{u} dS$
2. Reynolds Stress term: $-\rho \iint_{S_{wake}} \overline{u'^2} dS$
3. Pressure term $\iint_{S_{wake}} (p_\infty - \overline{p}) dS$

The Reynolds stresses, produced as a result of the Reynolds decomposition, are a way of expressing the stresses arising due to the turbulence in the flow. The wake being a turbulent region, the contribution from this term is expected to be considerable. Out of all the components in the Reynolds stress tensor, only the shear stress component along the streamwise direction contributes towards reducing the drag force.

2.6.1. Pressure Reconstruction

Since direct pressure measurements are not performed the computation of the pressure term involves the reconstruction of pressure in the wake of the cyclist from the velocity measurements made through PIV/PTV. Pressure reconstruction is performed using the methodology described by van Oudheusden [73, 74]. This methodology has been previously used in several works involving PIV measurements in thin volumes. [19, 76]

The Navier-Stokes equation used to estimate the pressure gradient reads as:

$$\nabla p = -\rho \frac{D\vec{v}}{Dt} + \mu \nabla^2 \vec{v} \tag{2.12}$$

where $\frac{D\vec{v}}{Dt}$ is the material acceleration obtained as:

$$\frac{D\vec{v}}{Dt} = \frac{\partial \vec{v}}{\partial t} + (\vec{v} \cdot \nabla)\vec{v} \tag{2.13}$$

Substituting Eq. 2.13 in Eq. 2.12, the pressure gradient is obtained as:

$$\nabla p = -\rho \left(\frac{\partial \vec{v}}{\partial t} + (\vec{v} \cdot \nabla)\vec{v} \right) + \mu \nabla^2 \vec{v} \tag{2.14}$$

Reynolds averaging of Eq. 2.14 results in a time-averaged pressure gradient and gives rise to the Reynolds Stress terms (fluctuating terms):

$$\nabla \overline{p} = -\rho(\overline{\vec{v}} \cdot \nabla)\overline{\vec{v}} - \rho \nabla \cdot (\overline{\vec{v}'\vec{v}'}) + \mu \nabla^2 \overline{\vec{v}} \tag{2.15}$$

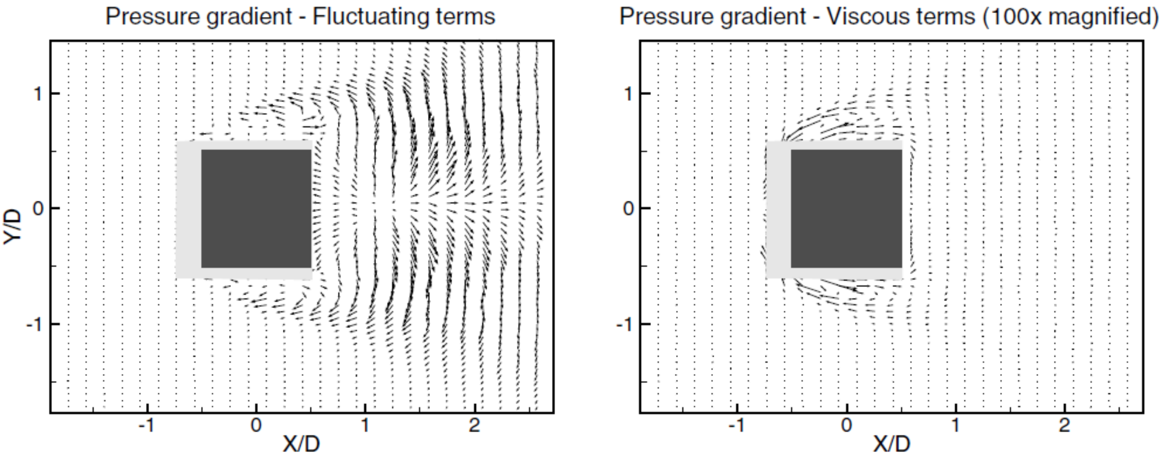

Figure 2.10: Contribution of the fluctuating terms and the viscous terms to the time-averaged pressure gradient for a bluff-body, $Re_D = 20000$. Reproduced from van Oudheusden [74] (Side of square = D)

van Oudheusden [73, 74] observed that the contribution of the viscous terms to the time-averaged pressure gradient was negligible as shown in Fig. 2.10. Note the magnified scale for the viscous terms. Thus, neglecting the viscous terms in Eq. 2.15 and taking the divergence on both sides:

$$\nabla^2 \overline{p} = -\rho \nabla \cdot (\overline{\vec{v}} \cdot \nabla)\overline{\vec{v}} - \rho \nabla \cdot \nabla \cdot (\overline{\vec{v}'\vec{v}'}) \tag{2.16}$$

Eq. 2.16 represents the *Pressure Poisson Equation* (PPE).

The PPE is an elliptic partial differential equation and requires four Boundary conditions (BCs) (two each in X and Y directions) for the problem to be well-posed. Specifying the BCs (either Dirichlet or Neumann) on the boundaries of the measurement volume, the PPE is solved numerically on a Cartesian grid to reconstruct the pressure in the entire domain following the methodology given by Hoffmann [33].

This is done by discretizing the PPE ($\overline{p}_{xx} + \overline{p}_{yy} = RHS$) on the Cartesian grid using a second-ordered finite difference scheme and expressing the pressure at each location using a five point method as shown in Fig. 2.11.

Thus,

$$\nabla^2 p_{i,j} = \frac{1}{\Delta x^2}\left(p_{i+1,j}+p_{i-1,j}+p_{i,j+1}+p_{i,j-1}-4p_{i,j}\right) = RHS_{i,j} \tag{2.17}$$

where Δx is the grid spacing (assumed equal in both directions). RHS is a $m \times 1$ column vector consisting of the gradients of the mean velocities and Reynolds stresses. Eq. 2.17 simplifies to the form $ap = RHS$, where p is a $m \times 1$ column vector consisting of pressures in the domain. a is an $m \times n$ coefficient matrix known as the Poisson matrix. Elements of RHS are evaluated by taking the gradient of the time-averaged pressure gradient equation (Eq. 2.15). The details for evaluating this time-averaged pressure gradient can be found in Section 4.4.

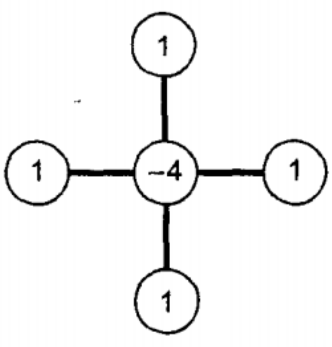

Figure 2.11: Five point method for the finite difference scheme for pressure reconstruction. Reproduced from Hoffmann 2001[33]

2.7. External Force Balance

Force balances are the most common devices to measure the aerodynamic forces and moments on a test object in a wind tunnel. Usually, the model is mounted on the balance with the help of struts. The balance consists of sensitive electrical elements called the strain gages (shown as A to F in Fig. 2.12). Forces can be measured by pre-calibrating the change of the electrical resistances of these strain gages (due to stretching of the gages) in the respective directions. Moments are measured by using the distance between the two strain gages (a to c). In the adjoining sketch the drag force in the direction of the flow is given by summing the strain gages $D + E$.

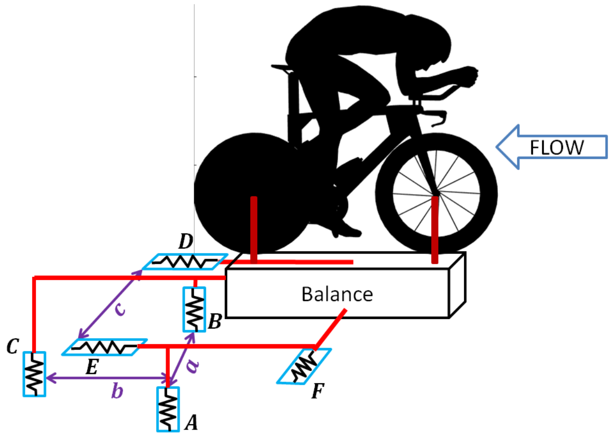

Figure 2.12: Schematic arrangement of strain-gages inside an external force balance. Original sketch from Glenn Research Center, NASA https://www.grc.nasa.gov

3

Experimental Setup

Two experimental campaigns were carried out at the High Speed Laboratory of the Delft University of Technology. This chapter delineates the experimental facilities, equipments and the model of the cycling mannequin used during these experiments in section 3.1 and the various factors considered to design the experiment in section 3.2

In the first campaign 4D-PTV wake measurements were performed at wind speeds in the range $13 m/s$ to $15 m/s$ at increments of $0.5 m/s$. The second experiment was performed to achieve statistically converged flow field results only at one speed of $14 m/s$.

3.1. Facilities and models

3.1.1. Wind Tunnel Facility

The experiments were carried out at the Open Jet Facility (OJF) at the High Speed Laboratory, TU Delft. The OJF is a closed loop wind tunnel with an open test section. The cross-section of the tunnel exit is octagonal with dimensions $2.85 \times 2.85 m^2$. The tunnel is run by a fan coupled with a 500kW electric motor and wind speeds upto 35m/s are achievable. The OJF is equipped with a settling chamber placed just before the contraction that consists of a honey comb structure and five fine mesh screens to reduce the turbulence levels. It is also equipped with a cooling radiator placed after the test section so that a constant air temperature is maintained throughout the test. The turbulence levels have been previously quantified to be 0.5% of the wind speeds [32]. Fig 3.1 shows a schematic of the OJF.

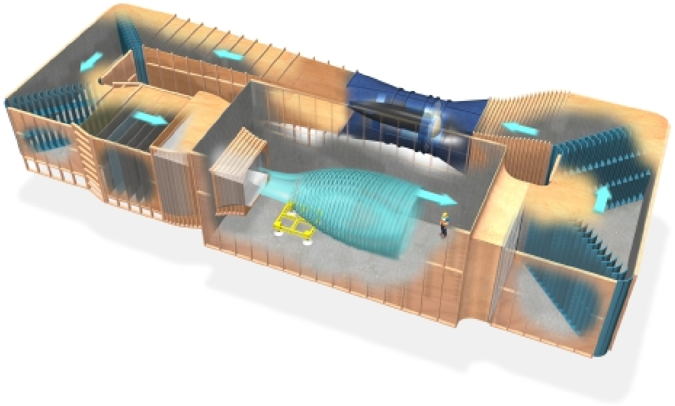

Figure 3.1: Schematic of the Open Jet Facility [32]

The open test section of the OJF measures roughly 7 metres in width and 13 metres in length. As depicted in Fig 3.1, the air-stream expands as it flows into the test section room.

3.1.2. Cycling Mannequin and Bike

A full scale 3D printed mannequin was constructed by 3D scanning a Dutch professional cyclist Tom Dumoulin (Team Sunweb, previously GIANT-Alpecin) [75]. The mannequin was previously used in a previous study by Terra et. al.[67] at TU Delft. It resembles the athlete in the time-trial position with the legs positioned asymmetrically at 75 deg crank angle (Fig 3.2). The same mannequin dressed with a skin-suit from GIANT-Alpecin has been used in this study. The bike used is a Rio edition of Giant Trinity Advanced Pro TT (3.5(b)) equipped with Shimano Dura Ace 9070 group set, Giant AeroDrive TT handlebars and Giant 45 deg extensions. A spoked tubular front wheel and a rear disc wheel are from Shimano PRO, with Vittoria Corsa Evo CX 25mm wide tires. A Giant AeroVault bottle is mounted on the down tube. The wheelbase of the bike is 1m and wheels have a diameter of 28 inches, amounting to a total length of 1.71m The total weight of the mannequin is approximately 12kg and the bike weighs 8.8kg. Table 3.1 shows the dimensions of the mannequin.

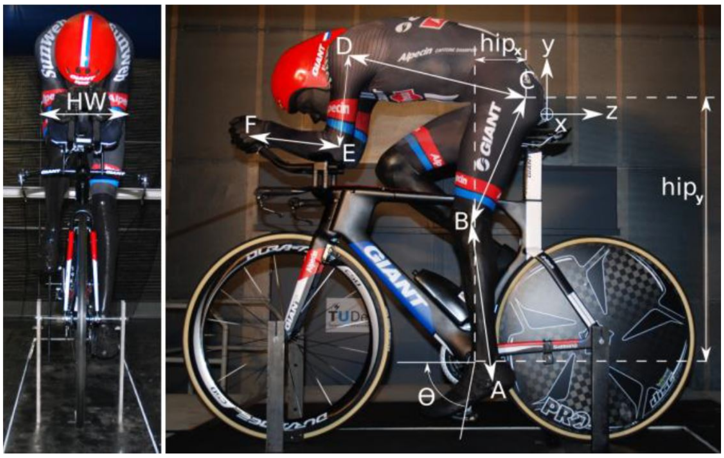

Figure 3.2: Dimensions of the mannequin (Reproduced from Terra et. al. [67])

Name	Symbol	Dimension	Name	Symbol	Dimension
Crank Angle	θ	75°	Lower Leg	A-B	475mm
Hip Width	HW	365mm	Upper Leg	B-C	460mm
Shoulder Width	SW	380mm	Torso	C-D	600mm
Hip Location x	hip_x	180mm	Upper Arm	D-E	326mm
Hip Location y	hip_y	850mm	Lower Arm	E-F	290mm

Table 3.1: Dimensions of mannequin. Refer Fig 3.2 for notations. Reproduced from Terra et.al.[67]

3.1.3. Test Bench

The OJF is equipped with a large testing table which was aligned with the stream-wise direction. The test bench consisting of the wind tunnel balance, bike support stand and metal frame with a wooden floor was mounted on the testing table (Fig 3.4). The coordinate system of the balance was oriented such that the axial direction (X-axis) was aligned with the stream-wise direction (Z-axis of the defined coordinate system). The bike support plate was mounted on the wind tunnel balance with a wooden connecting plate in between. Four vertical steel struts, which are approximately 29 inches high from the base of the bike support plate, have grooves at the ends to clamp the axles of the wheels.

A metal frame with adjustable supports was mounted on the testing table surrounding the bike support plate. A wooden floor with slots cut-out for the passage of the four vertical struts was fixed on top of the metal frame covering all the equipments below it. Sufficient gap was maintained between the wooden plates of the floor and the support plate structure connected to the balance so to eliminate any chances of contact during the experiments. The testing table was adjusted so that the wooden floor started at the tunnel exit plane and was approximately $5cm$ above the lower side of the tunnel exit. The forward-most point on the front wheel was approximately $0.5m$ from the tunnel exit plane in the first experiment. In the second experiment an additional wooden floor was added between the tunnel exit plane and the model amounting to a total distance of $1.75m$. Leading edge of the ground plate was shaped into a knife edge.

3.1.4. 4D-PTV setup

The 4D-PTV setup consists of three high speed cameras, a Nd-YAG high repetition rate Laser, a programmable timing unit, an acquisition computer with DaVis software for controlling the actions and a seeding system for seeding the air-flow with Helium-Filled Soap Bubbles. A detailed list of the instruments and their specifications is given in Table 3.2.

Imaging and Illumination

The field of view required to capture the total wake of the cyclist (stream-wise velocities extending to the free-stream values on the sides and top) is estimated to be 1m in width and 1.6m in height from the results of Terra et. al. [67]. The cameras are mounted on tripods placed downstream of the field of view (outside the expanding air-stream to minimize vibrations as well as to be non-intrusive) directed towards the entire field of view (Fig 3.3). The apertures of the cameras are set to a value of $f/4$. All cameras were equipped with fixed focal length objectives as mentioned in the Table 3.3. The cameras were also equipped with tilt adapters to account for the angle between the image place and the subject plane (Scheimpflug condition). The Laser was placed on the side (as seen in the background of Fig 3.3(c)) illuminating a thin volume of 50mm thickness at the centre-plane of the model with a combination of spherical and cylindrical lenses. Following the suggestion by Terra et.al. [69] the Laser sheet is positioned approximately $800mm$ (more than 2 times Hip Width) behind the saddle of the bike. Due to the expansion of the light sheet, a thickness of approximately $45mm$ to $55mm$ (in the direction of expansion) was available throughout the domain.

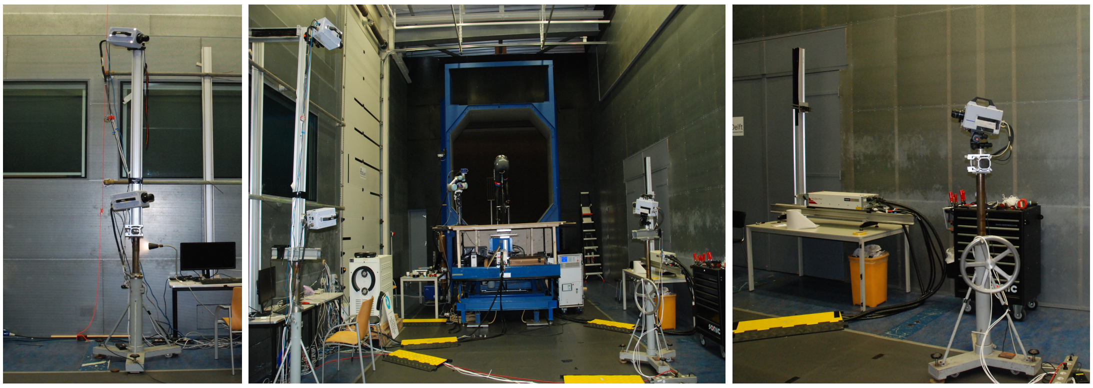
(a) (b) (c)

Figure 3.3: (Left) Two cameras positioned on the right side (Right) and one camera on the left side (looking in the downstream direction). (Middle) Experimental Setup as seen from behind

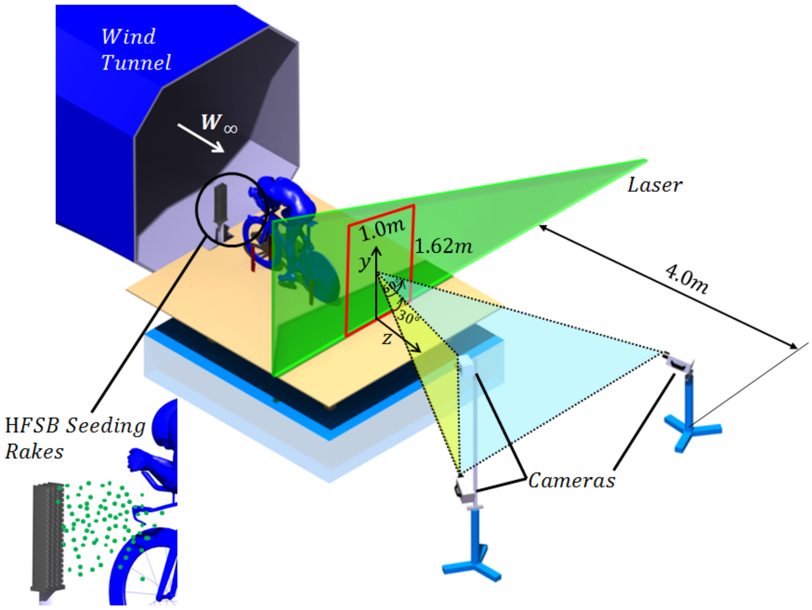

Figure 3.4: Schematic diagram of the experimental setup showing the camera, laser and seeding system position with respect to the model.

Purpose	**Instrument**	**Specifications**
Imaging	High Speed Cameras	Photron Fast Cam SA1 (CMOS), 1MegaPixel (pixel pitch $20\mu m$), 5400 fps at full sensor size
	Objectives	Nikon $f = 35mm$ and $f = 50mm$
	Schiempflugs (Tilt adapters)	$\pm 15^\circ$
Illumination	Laser	Mesa-PIV, Nd:YAG, 532nm, upto 6kHz, ($2 \times 18mJ$ at 1kHz)
	Optics	Cylindrical and spherical lenses, 45° mirrors, supports
Seeding	Helium-Filled Soap Bubble generator	HFSB Generator - LaVision [47]
	Seeding Rakes	Developed at TU Delft, 4 vertical rakes with 20 nozzles each.
Timing	Programmable Timing Unit	High Speed Controller LaVision [48]
Data collection	Software	DaVis - LaVision [46], v8.4.0
	Computer	Acquisition computer - LaVision

Table 3.2: Instruments required for Large scale 4D-PTV measurements

Seeding

The HFSB generator consisting of a Fluid Supply Unit, Helium gas cylinder, pressurized air supply and a seeding rake mounted on a traversing system was used to produce the bubbles. The equipments and the traversing system were placed under the wooden floor(see Fig.3.4). The seeding rakes were mounted on an aerodynamically shaped support structure, which enclosed the tubing for the fluids, in order to minimize its intrusion (Fig 3.5(b)). The seeding rakes made from polymer were aerodynamically shaped with sharp trailing edges with the

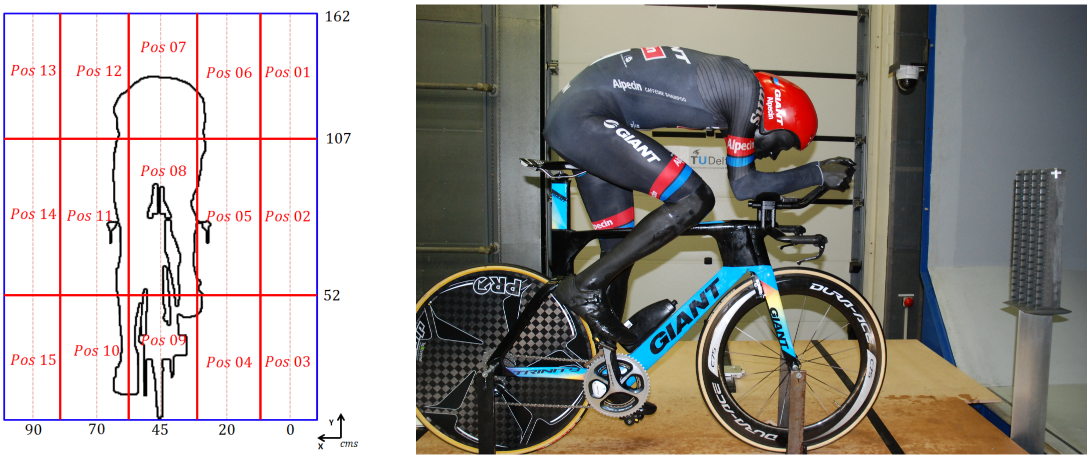

(a) (b)

Figure 3.5: (a) Positions of the seeding rakes as seen from the back of the model. (b) Side view of Mannequin and bike with seeder positioned at Pos 08

nozzles placed in gaps of 2.5cm in the vertical direction. The rakes had a gap of 5cm between them. The total external dimensions of the seeding rakes were 50$cm \times 15cm$ in height and width respectively.

Owing to these dimensions of the seeding system, the seeding of the entire wake of the cyclist was carried out by traversing the seeding rakes to different locations. A total of 15 positions (5 stations in width-wise direction and 3 stations in height-wise direction) were required to seed the entire wake. (see Fig 3.5(a))

Acquisition

Time resolved data was acquired in short bursts of 11 images captured at a frequency of 4kHz. Each burst (called "Cycle") was acquired with a gap of 0.1 seconds between successive bursts to obtain multiple uncorrelated samples. In the first set of experiments 480 Cycles (5280 images) were acquired at every position of the seeder. In the second set of experiments, 1560 Cycles were acquired at the positions closer to the wake and 780 Cycles in the positions closer to the freestream. Overview of the settings is available in Table 3.3.

	Cameras			**Seeding** [bar]			**Acquisition**			
	Distance	θ_x	θ_y	Air	He	BFS	f_{acq}	f_s	Cycles	Images
Expt. 1	4.2m	$-15°$	$-25°$	3	1.8	2.4	4kHz	10Hz	480 All Positions	11
	4.2m	10°	$-25°$							
	3.2m	15°	30°							
Expt. 2	5m	$-5°$	$-30°$	3	1.8	2.4	4kHz	10Hz	780 [Pos $1-3$ &$13-15$] 1560 [Pos 4-12]	11
	5m	10°	$-30°$							
	5m	10°	30°							

Table 3.3: Settings for 4D-PTV Experiments

A schematic of the setup and detailed design calculations for the choice of these parameters are available in section 3.2. Note, due to practical considerations some parameters have been chosen slightly different than those obtained theoretically in Table 3.4.

3.1.5. Wind Tunnel Balance

The OJF External Balance is a six-component wind tunnel balance designed, manufactured and calibrated at the National Aerospace Laboratory, Netherlands (NLR). The balance measures the three force components and the three moments. Under simultaneous loading of all six components the balance is capable of measuring loads up to 25kg in the stream-wise direction with a maximum uncertainty of 0.06% [2]. The balance was mounted directly under the ground plate and connected only to the bike support plate as shown in Fig 3.3(b).

Balance measurements were recorded for all positions of the seeding rakes (Pos 1-15; see Fig 3.5(a)). Due to the presence of a blunt edged aerodynamic fairing under the seeding rakes, some loss in momentum of the incoming flow was directly observed through the resulting drop in the drag force. In order to have comparable drag measurements with the 4D-PTV result a separate set of balance measurements was acquired without the presence of the seeding system upstream of the model. The balance was biased (zeroed at no wind speed) before acquiring these set of measurements without the presence of the seeding system.

3.2. Design of experiment

This section briefly describes the parameters that have been considered for setting up the large-scale 4D-PTV experiment.

Length and velocity scales

Field of view is estimated from the dimensions of the model (Fig. 3.2) and previous experiments by Terra et. al. [67]. Typical time-trial speeds are chosen yielding a Reynolds Number of 5.74×10^5 based on the torso chord length.

Imaging

With the $1MPx$ high speed cameras a magnification of 0.0125 and a digital image resolution of $1.6mm/px$ can be obtained. It is important to note that the particle image size is much smaller than the digital resolution. Based on the depth of field, $f_{\#}$ of 1.96 is estimated as a limiting value.

Seeding concentration

The seeding system produces in the order of 30000 bubbles per second and the nozzles seed a cross section area of approximately $5 \times 5cm^2$ [11]. This allows a sufficient seeding concentration of $0.8 bubbles/cm^3$. Based on this value and a window size of $0.5 \times 0.5 \times 5cm^3$ we can obtain 1 bubble/window.

Sample collection for statistics

The torso of the cyclist can be approximated as a cylinder with diameter equal to the hip width. The vortex shedding frequency is obtained from the constant Strouhal Number of 0.2 for a cylinder. In order to have uncorrelated samples, the time separation between the samples needs to be greater than the vortex shedding time. This is obtained by $f_{sample} = Sr \times V_\infty / L_{St}$. The number of samples required to have a statistically converged flow field is determined by aiming to have 500 bubbles within each window.

Acquisition frequency

Taking note of the fact that the particle image size is smaller than the digital resolution, a maximum particle displacement of $2.5px$ ($4mm$) is allowable. The particle can be captured for a maximum of 12 instances before it moves out of the Laser sheet. At the given wind speed this translates to an acquisition frequency of approximately $4kHz$.

Field of View		Velocity	
x (Width)	$1000mm$	$W_{\infty_{OJF}}$	$15m/s$ (Range: $13m/s$ to $15m/s$)
y (Height)	$1600mm$	L_{Re}	$600mm$ (C-D)
z (Thickness)	$50mm$	Re	5.74×10^5
Imaging			
Sensor size	$20mm \times 20mm$	Magnification	0.0125
$f_{\#limit}$	1.96	$f_{\#used}$	4
Objective	$50mm$ | $35mm$	Subject Distance	$4m$ | $2.8m$
Resolution	$1MPx$	Digital Image Resolution	$1.6mm/px$
Acquisition		Seeding Concentration	
Mode	Cyclic	$\dot{N}_{bubbles}$	30000 per second
Max. disp. Δx	$2.5px$ $(4mm)$	Area seeded	$5 \times 5cm^2$/nozzle
N_{images}	12 images/cycle	Concentration	$0.8bubbles/cm^3$
f_{acq}	4 kHz	N_{window}	1 bubble/window (Window size: $0.5 \times 0.5 \times 5cm^3$)
Statistics			
Strouhal Number	0.2	L_{St}	$0.365m$ (HW)
f_{sample}	8Hz	N_{sample}	500 (criteria: 500 bubbles/window)

Table 3.4: Design of experiment and settings

4

Data Reduction and Analysis

This chapter describes the exact steps taken to process the acquired PTV data in order to achieve the qualitative and quantitative results in terms of the flow field and the drag force. Section 4.1 describes the necessary pre-processing and processing steps including calibration procedures and application of the tracking algorithm. Section 4.2 describes the steps to utilize the particle and track information to achieve reliable flow-field results. Finally, section 4.4 delineates the procedure used to evaluate each term of the drag equation in order to achieve the total drag force from PTV.

4.1. PTV: Processing techniques

4.1.1. Calibration

The calibration plate (Fig.4.1) used was a scaled-up version of the Type 30 calibration plate by a factor of 4 in all directions except the thickness. Geometrical calibration was performed with the pin-hole model. Table 4.1 shows the scale of the calibration used with respect to the standard Type 30 plate used for small scale measurements.

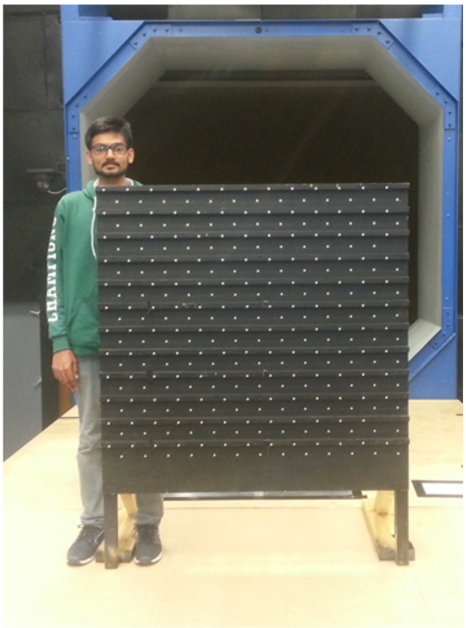

Figure 4.1: Calibration plate used for geometrical calibration.

Parameter	BIG		Type 30	
Width	1200	mm	300	mm
Height	1200	mm	300	mm
Thickness	40	mm	12	mm
Plane to Plane Distance	20	mm	2	mm
Number of Marks	X Y	13 12	X Y	12 12
Mark Size	8	mm	2	mm
Mark to Mark Distance	90	mm	22.5	mm

Table 4.1: Comparison of calibration plate ("BIG") used in this experiment to LaVision Type 30 plate

The volume self calibration (VSC) procedure [78] resulted in a maximum disparity error of 0.2px by dividing the volume in 20×20 sub-volumes on two Z-planes. This was done by seeding the entire region of interest with the HFSB and acquiring a set of 500 images at a frequency of $10Hz$. During this acquisition procedure, a large bluff-body was placed in the upstream region to add turbulence in order to spread the HFSB in the entire field of view. Although this yielded satisfactory results for the disparity errors, it was observed that the corners of the field of view received relatively less seeding with this procedure. Therefore, couple of acquisitions were added by traversing the seeder closer to those locations during the second experiment. The kernel size for self calibration was also increased to 1650 images. The geometrical calibration was corrected once using the self-calibration procedure and the Optical Transfer Function (OTF) was evaluated [60]. Since the maximum particle size is 1-2 pixels a Fit-Area of 5×5 voxels is used to filter the OTF.

4.1.2. Image Pre-processing

The raw images acquired in cycles were preprocessed by masking saturated region formed due to the Laser sheet on the floor and subsequently subtracting the time average to obtain low background noise (less than 10 counts). The averaged light intensity of the brightest particles was found to be in the range of 100 to 150 counts depending on the position in the field of view (Fig. 4.3(b)).

4.1.3. Particle tracking

Each cycle with pre-processed images was processed using the Shake-The-Box algorithm [61]. The OTF was used in the STB algorithm to reconstruct the positions of the particles spatially and temporally. Depending on the position of the seeding in the field of view, different values were required for the parameters which are delineated in Table 4.2. The positions which are closer to the freestream, namely Positions 1 to 3 and 13 to 15 (See Fig 3.5(a)), are expected to have velocities close to the set wind speed in the streamwise direction. Therefore, a Maximum Particle Displacement of 4 Voxels in all directions is used. Positions which are closer to the wake, namely Positions 4 to 12, are expected to have appreciable velocities in all the three directions. Therefore, this parameter has been relaxed to 5 Voxels.

Parameters such as the 'Maximum Relative change in particle shift' and 'Maximum Abso-

Image Pre-Processing			
	Laser sheet on floor	Geometric mask	
	Background	Subtract Time Avg.	
Shake-The-Box			
Property	**Parameter**	**Freestream (Pos 1-3 & 13-15)**	**Wake (Pos 4-12)**
Light Intensity	Threshold Intensity	20-30 counts	30 counts
	OTF Intensity	5 (Maximum)	5 (Maximum)
	OTF Size Factor	1 (Minimum)	1 (Minimum)
Particle Search	Maximum Particle Displacement	4 Voxels	5 Voxels
	Allowable Triangulation Error	1 Voxels	1-2 Voxels
	Shake Delta	0.2 Voxels	0.2 Voxels
Acceleration Limits	Max. Abs. change in particle shift	1 Voxel	1 Voxel
	Max. Rel. change in particle shift	20-40%	30-50%
Iterations	Add Particle Iterations	5	5
	Refine Iterations	5	5
Particle Acceptance	Minimum Track Length	4	4
	Remove Close Distance	1 Voxel	1 Voxel
Polynomial Fitting	Minimum Track Length	4	4
	Order of fit	2	2
	Length for fit	7	7
	Weighting for fit	Gaussian	Gaussian

Table 4.2: 4D-PTV processing parameters

lute change in particle shift' limit the allowable acceleration of a particle from one time step to the next. These parameters are found to be most critical in determining the quality of the tracks. A general observation from Fig.4.2 is that being too generous with these parameters causes an increase in the wrongly triangulated particles. Therefore, this parameter sweep has been used to determine the limits of these parameters particular to the acquired data. Since it is not expected for the flow to have negative streamwise velocities at the location of the measurement volume, a particle having negative streamwise velocity is chosen as a criteria for categorizing the particle as a wrongly triangulated particle. Corresponding track has been categorized as an unwanted track. Based on this parametric study it has been observed that, for a Maximum Relative change in particle shift of up to 40%, a Maximum Absolute change in particle shift of 2 leads to an increase in the number of unwanted tracks by 5% in the Freestream positions and by 2.5% in the Wake positions as compared to a value of 1. Fig. 4.2(a) and 4.2(b) show that the curve for Unwanted Tracks for $A = 2$ is consistently above that for $A = 1$, where A is the Maximum Absolute change in the particle shift parameter.

It can also be observed that the number of total tracks obtained in the Wake positions are much larger than that obtained in the Freestream positions. This can be attributed to two reasons. Firstly, the area covered by the particles in the wake region is larger than the area covered in the freestream positions (see Fig 4.3(a)). This is because the streamtube widens owing to the presence of the model. Secondly, due to this spreading of the particles over a larger area, the particle image density is lower in the wake than the freestream positions. The particle density in the freestream positions is large enough for two particles from different

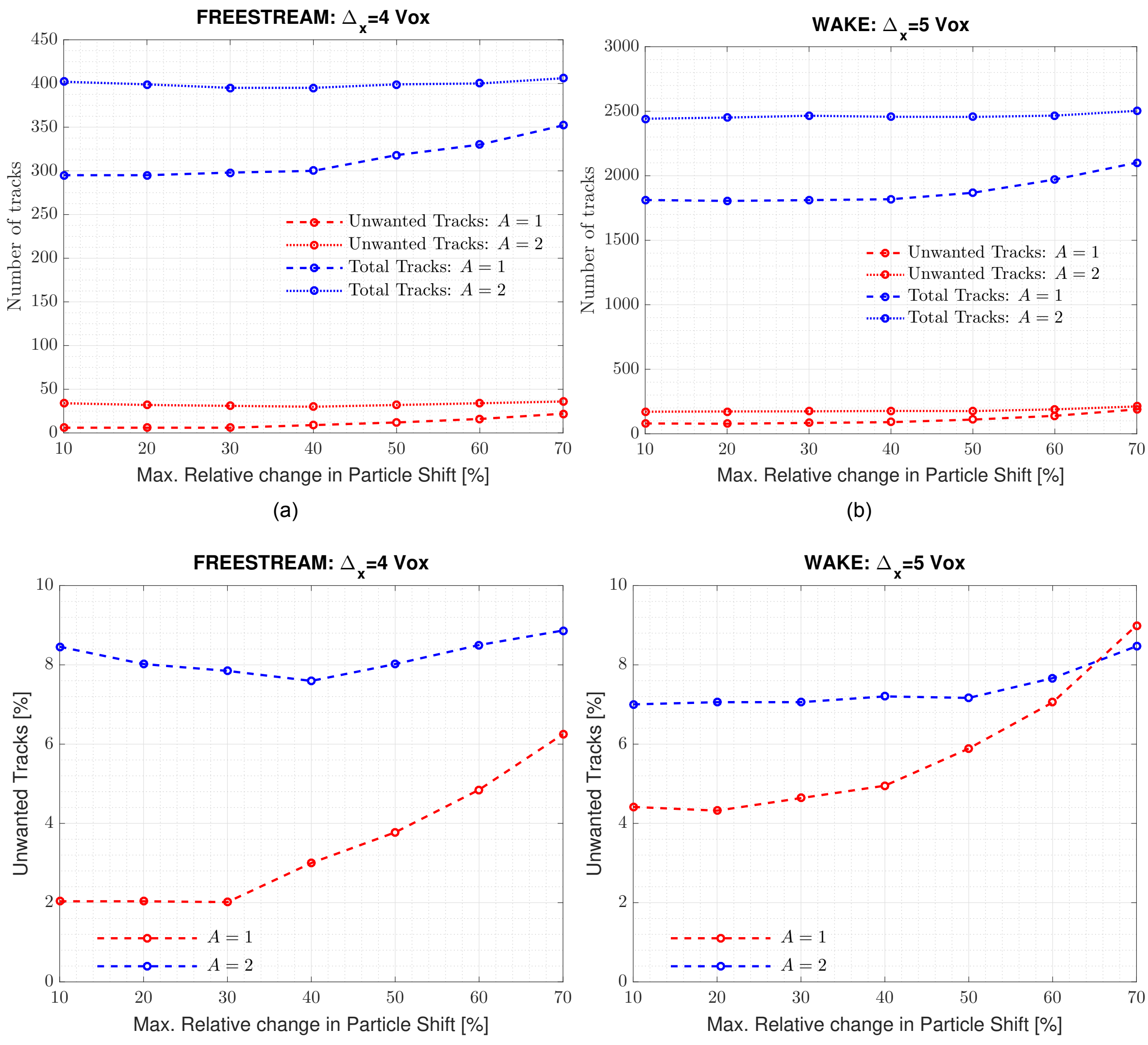

(a) (b)

(c) (d)

Figure 4.2: Parameter sweep of STB Parameters: Maximum Relative change in particle shift and Maximum Absolute change in particle shift. Shows number of total and unwanted tracks at (a) Freestream position - Pos 02 (b) Wake Position - Pos 08. Percentage of unwanted tracks out of total tracks is shown in (c) Freestream position - Pos 02 (d) Wake Position - Pos 08. Δ_x is the Maximum allowed particle shift and A is the Maximum Absolute change in particle shift.

tracks to be close to one another within a distance of 1 Voxel (see Particle Acceptance criteria in Table 4.2). This leads to a rejection of such closely reconstructed particles by the STB algorithm thus leading to a loss of a number of tracks at these positions.

4.2. PTV: Post-processing techniques

This section describes the steps taken to utilize the particle track and velocity information in the Lagrangian format throughout the wake and obtain a velocity field on a Cartesian grid in the complete wake. First, particle tracks from different positions and different samples are integrated into a single volume. Subsequently the integrated particles are arranged into smaller sub-volumes, called as “bins” in this document. Prior to dividing the particle tracks on the Cartesian grid, the particles are filtered according to a set of criteria on acceptable velocities. They are again filtered using an outlier detection criteria for each bin. Finally, a velocity vector is obtained for each bin y averaging the velocities of the particles contained in the bin. The details are given in the following subsections.

4.2.1. Integration of particle tracks

Similar to the traditional wake survey experiments with pressure probes or hot wires, this experiment is performed by scanning the wake with 15 different seeder positions as shown in Fig.3.5(a). Therefore, to visualize the complete wake, data from all the positions are combined into a single volume.

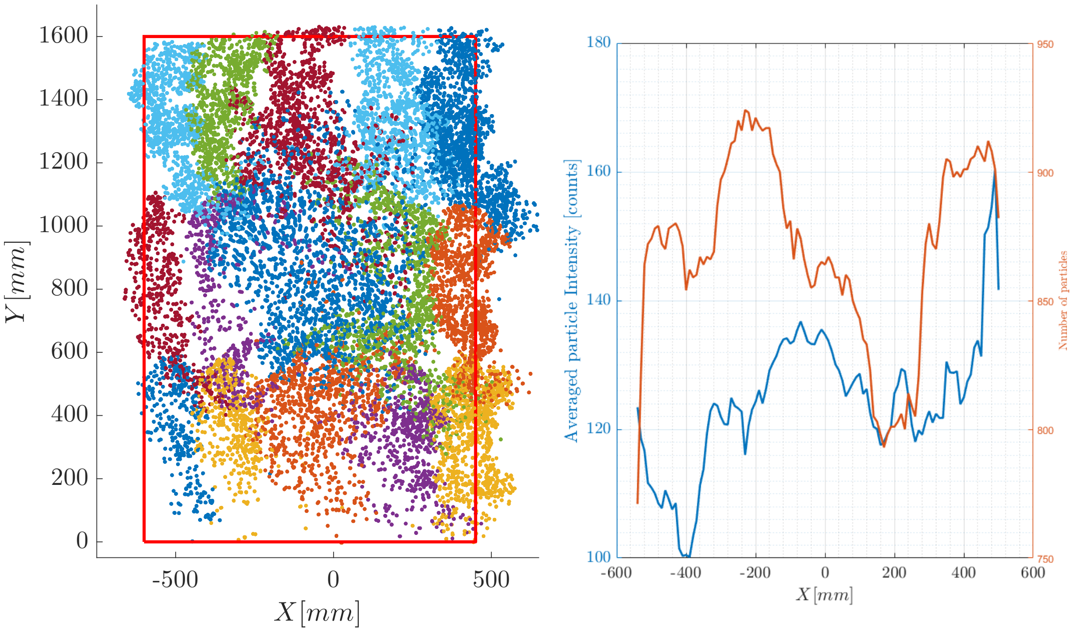

(a) (b)

Figure 4.3: (a) Field of view with particle tracks integrated from all the positions for 1 sample. Red border line shows the measurement volume. (b) Light intensity profile and the number of reconstructed particles obtained through STB. Laser sheet expanding in -X direction.

Furthermore, multiple uncorrelated samples are acquired at each position as shown in Table 3.3. It was found that first combining the Lagrangian particle information from all the samples and then converting this information onto a Cartesian grid gave results free of boundary effects. Fig 4.3(a) shows the particle tracks from different seeder positions (in different colours) integrated into a single volume. This is depicted only for one cycle per position. In practice, tracks from all the cycles have been integrated. Wide white spaces observed in the lower part of the domain in this figure disappear upon integrating tracks from all the samples.

Fig 4.3(b) shows that the average light intensity drops in the direction of expansion of the Laser sheet. This is one of the reasons for a lower number of tracks in the Freestream positions 13 to 15 as compared to the number of tracks found in positions 1 to 3.

4.2.2. Grid conversion techniques

Apart from their position in the volume, each particle has velocity, acceleration, light intensity and a Track ID Number associated with it in a Lagrangian format. Quantitative information such as vorticity, pressure and drag force can be derived from these tracks by first converting them into a Cartesian framework. Therefore, a grid is constructed in the measurement volume ($1000mm \times 1600mm \times 80mm$) shown within Red border in Fig. 4.3(a). Slightly larger depth is considered for the measurement volume to account for the small tilt angle in the Laser sheet. Particles are detected within small windows (called “cells”) of size $80mm \times 80mm \times 80mm$ on the grid and the associated quantities are averaged and assigned to the centre of the cell. The size of the cells might seem very conservative, however, it is smaller than the size of the expected flow structures and hence are chosen. Furthermore, the streamwise gradients are expected to be negligible within the considered thin volume. Fig. 4.4(a) shows one Z-plane for a grid generated on a collection of particle tracks from 100 uncorrelated samples. Fig. 4.4(b) shows a close-up of the grid. Overlap of 75% has been applied between the cells while averaging over the particle quantities to counter inter-cell boundary effects as well as to have a sufficient spatial resolution. Vectors are available every 20mm.

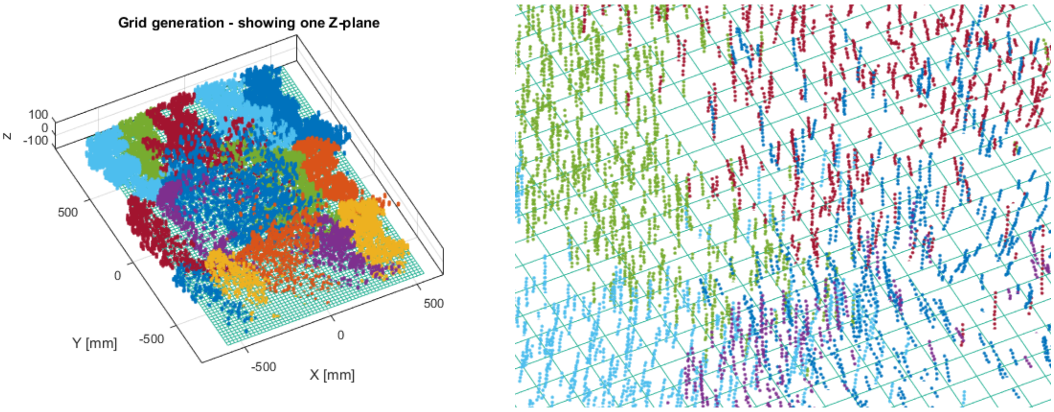

(a) (b)

Figure 4.4: (a) Grid generation on combined particle tracks (b) Close-up of a Z-plane of the generated grid

4.2.3. Filters

Velocity Filter

Raw particle data obtained from Shake-The-Box contains a small portion of wrongly triangulated particle yielding some unwanted tracks (as shown in Fig.4.2). These unwanted tracks (see Fig.4.2) and particles are filtered out by detecting and eliminating them from the dataset. This filter has been referred to as the "Velocity Filter" henceforth.

Velocity Filter	
In-plane	-10m/s ≤u ≤10m/s -10m/s ≤v ≤10m/s
Out of plane	0m/s ≤w ≤$W_{\infty_{OJF}}$+2m/s

Table 4.3: Velocity filtering criteria

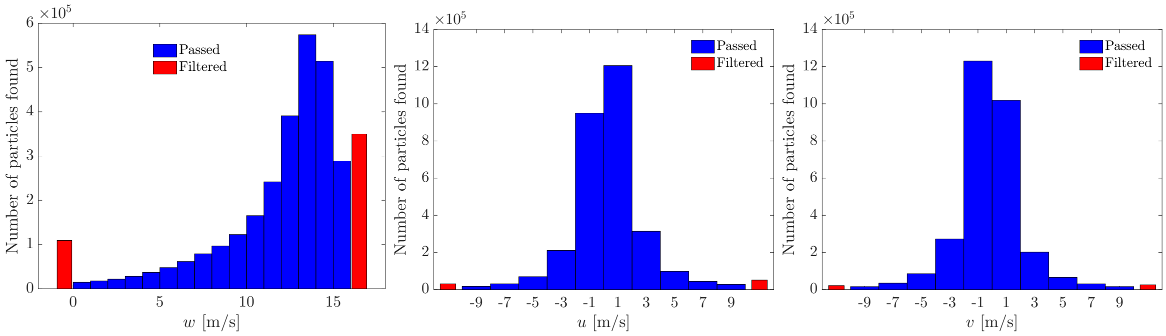

(a) (b) (c)

Figure 4.5: Histograms showing the number of particles found in small range of velocities. Particles filtered according to criteria given in Table 4.3 in the following order (a) W (b) U and (c) V. (Red bars show cumulation of all particles lying outside the limits given in Table 4.3)

Median Filter

While an a-priori velocity filter works on the global limits of the complete dataset, another filter is required to eliminate particle data that lie outside the local limits. Therefore, a median filter developed by Westerweel and Scarano [77] has been implemented to filter particles from each bin. Unlike its implementation on the PIV vector data as shown in [77], here the median filter has been implemented on a single bin consisting of several particles and the associated velocity information. Following equations show the steps taken to identify and eliminate the outliers in every bin. The process is repeated twice for increased accuracy of the final velocity vector.

$$u_m = median\{u_1, \ldots, u_n\} \tag{4.1}$$

where 1, ..., n are the particles in the bin.

Residuals r_i corresponding to each particle are obtained as follows:

$$r_{u_i} = |u_i - u_m| \tag{4.2}$$

Median of the residuals r_m are evaluated for normalization:

$$r_{u_m} = median\{r_{u_1}, \ldots, r_{u_n}\} \tag{4.3}$$

Normalized residual r_o^* for each velocity component is then obtained as:

$$r^*_{o_{u_i}} = \frac{|u_i - u_m|}{r_{u_m} + \varepsilon} \tag{4.4}$$

where $\varepsilon = 0.2$ has been chosen as the minimum normalization level. Similar procedure is followed for the other velocity components V and W to obtain $r^*_{o_{v_i}}$ and $r^*_{o_{w_i}}$ respectively.
Finally, the particle is considered an outlier if the following quantity exceeds a threshold value of 2.

$$\sqrt{{r^*_{o_{u_i}}}^2 + {r^*_{o_{v_i}}}^2 + {r^*_{o_{w_i}}}^2} > 2 \qquad \Rightarrow i = outlier \tag{4.5}$$

Fig. 4.6(a) shows that the median filter rejects about 50% of the particles found per bin in the wake region whereas it rejects about 30% of the particles in the freestream regions. After this filtering, there are enough particles in the domain to obtain the velocity vectors (see Fig. 4.6(b)).

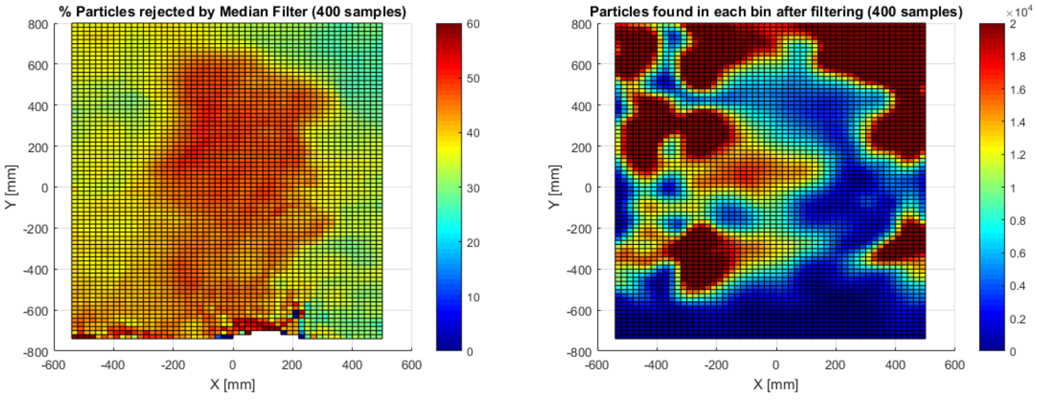

(a) (b)

Figure 4.6: (a) Percentage of particles rejected by the median filter for every bin throughout the volume (b) Particles per bin remained after filtering, averaged over all the Z-planes.

4.3. Vortex identification

As seen in the literature, the wake of a bluff-body such as a cyclist typically consists of three-dimensional vortical structures. The tools used to identify such structures are discussed below.

4.3.1. Vorticity

Vorticity is defined as the curl of the velocity and it gives the tendency of the flow to rotate at any given point in the domain about a rotation axis. Thus, the vorticity $\vec{\omega} = (\omega_x, \omega_y, \omega_z)$ is given by

$$\vec{\omega} = \nabla \times \vec{V} = \begin{vmatrix} \hat{i} & \hat{j} & \hat{k} \\ \frac{\partial}{\partial x} & \frac{\partial}{\partial y} & \frac{\partial}{\partial z} \\ u & v & w \end{vmatrix} \tag{4.6}$$

$$\begin{bmatrix} \omega_x \\ \omega_y \\ \omega_z \end{bmatrix} = \begin{bmatrix} \frac{\partial w}{\partial y} - \frac{\partial v}{\partial z} \\ \frac{\partial w}{\partial x} - \frac{\partial u}{\partial z} \\ \frac{\partial v}{\partial x} - \frac{\partial u}{\partial y} \end{bmatrix} \tag{4.7}$$

Rotational flows may be present either due to swirling motions or shearing motions. Vorticity cannot distinguish between these two types of motions and may not be a suitable choice for vortex identification [39].

4.3.2. Q-criterion

Vortices are formed as a result of the generation of low pressure pockets causing the flow around them to be pulled towards the these pockets. This fact is used for the identification of the vortex in the Q-criterion given by Hunt et.al. [35]. Furthermore, the Q-criterion identifies the structures where the swirling motions dominate over the shearing motions [40]. This makes the Q-criterion a reliable tool to identify the vortices. The Q is defined as the second invariant of the velocity gradient tensor $\nabla\vec{V}$.

$$\nabla\vec{V} = \begin{bmatrix} \frac{\partial u}{\partial x} & \frac{\partial u}{\partial y} & \frac{\partial u}{\partial z} \\ \frac{\partial v}{\partial x} & \frac{\partial v}{\partial y} & \frac{\partial v}{\partial z} \\ \frac{\partial w}{\partial x} & \frac{\partial w}{\partial y} & \frac{\partial w}{\partial z} \end{bmatrix} \tag{4.8}$$

Decomposing the velocity gradient tensor into symmetric (S) and anti-symmetric (Ω) as:

$$S = \frac{1}{2}(\nabla\vec{V} + \nabla\vec{V}^T) = \begin{bmatrix} \frac{\partial u}{\partial x} & \frac{1}{2}\left(\frac{\partial u}{\partial y} + \frac{\partial v}{\partial x}\right) & \frac{1}{2}\left(\frac{\partial u}{\partial z} + \frac{\partial w}{\partial x}\right) \\ \frac{1}{2}\left(\frac{\partial v}{\partial x} + \frac{\partial u}{\partial y}\right) & \frac{\partial v}{\partial y} & \frac{1}{2}\left(\frac{\partial v}{\partial z} + \frac{\partial w}{\partial y}\right) \\ \frac{1}{2}\left(\frac{\partial w}{\partial x} + \frac{\partial u}{\partial z}\right) & \frac{1}{2}\left(\frac{\partial w}{\partial y} + \frac{\partial v}{\partial z}\right) & \frac{\partial w}{\partial z} \end{bmatrix} \tag{4.9}$$

$$\Omega = \frac{1}{2}(\nabla\vec{V} - \nabla\vec{V}^T) = \begin{bmatrix} 0 & \frac{1}{2}\left(\frac{\partial u}{\partial y} - \frac{\partial v}{\partial x}\right) & \frac{1}{2}\left(\frac{\partial u}{\partial z} - \frac{\partial w}{\partial x}\right) \\ \frac{1}{2}\left(\frac{\partial v}{\partial x} - \frac{\partial u}{\partial y}\right) & 0 & \frac{1}{2}\left(\frac{\partial v}{\partial z} - \frac{\partial w}{\partial y}\right) \\ \frac{1}{2}\left(\frac{\partial w}{\partial x} - \frac{\partial u}{\partial z}\right) & \frac{1}{2}\left(\frac{\partial w}{\partial y} - \frac{\partial v}{\partial z}\right) & 0 \end{bmatrix} \tag{4.10}$$

It is interesting to note that the non-diagonal elements in the anti-symmetric tensor Ω are same as those (except the sign) obtained for the vorticity magnitudes in Eq. 4.7. Non-diagonal elements of S are the strain-rates. Thus, the presence of a vortex is where the vorticity magnitudes are greater than the strain-rate magnitudes, given as:

$$Q = \frac{1}{2}\left(||\Omega||^2 - ||S||^2\right) > 0 \tag{4.11}$$

4.4. Drag computation using Control Volume approach

The control volume approach for drag computation from PIV data, developed by Oudheusden et. al. [73], has been used for the computation of drag from the velocity field. Time-averaged drag force has been evaluated from a velocity ensemble of uncorrelated PTV acquisitions. For this purpose, a mean velocity field and pressure field in the wake of the object is found to be sufficient to predict the trend of the drag force in the case of cylinders and spheres from past studies by Terra et.al. [68]. It also suggests that, if the wake survey plane (S_{wake}) is taken sufficiently downstream (greater than five diameters for spheres), the drag force can be solely predicted from the mean velocity field. However, in this case, all the terms in the drag equation (Eq. 4.12) have been evaluated and combined in an attempt to predict the drag force with utmost accuracy.

$$\overline{F}_{Drag} = \rho \iint_{S_{wake}} (W_\infty - \overline{w})\overline{w} dS - \rho \iint_{S_{wake}} \overline{w'^2} dS + \iint_{S_{wake}} (p_\infty - \overline{p}) dS \tag{4.12}$$

where $W = \overline{w} + w'$. $\overline{w}$ is the time-averaged streamwise velocity obtained by averaging the streamwise velocities from different uncorrelated samples, w' is the fluctuating component of the streamwise velocity and is obtained from the Eq. 4.21. W_∞ is the freestream velocity, ρ is the density of air and p_∞ is the static pressure in the freestream. $\overline{p}$ is the pressure in the measurement volume.

Previous studies on cyclists by Terra et. al. [67] suggest that apart from the momentum term, the Reynolds stress term contributes significantly to the total drag force whereas the contribution from the pressure term was found to be less than 5%.

4.4.1. Momentum term

The first term on the RHS of the Eq. 4.12 represents the momentum term. It is solely obtained from the time-averaged velocity field in the wake of an object by integrating the momentum deficit experienced by the flow. The air density ($\rho = 1.225 kg/m^3$) has been assumed to be constant throughout the entire experiment.

The freestream velocity $W_{\infty_{PTV}}$ should be, ideally, equal to the set wind speed of the wind tunnel. Eventhough, the time-averaged velocities obtained at the boundaries of the measurement volume suggest that the freestream conditions have been achieved (Fig. 4.7(a)), this speed is slightly different from that measured at the freestream positions in the PTV measurements. This small difference can largely be attributed to the expansion of the air stream from the tunnel exit as well as the measurement uncertainties of the PTV and the numerical errors induced by converting the Lagrangian particle data to a Cartesian grid. Thus, in order to circumvent this slight mismatch in the velocity, the freestream velocity W_∞ has been computed by taking the mean of the streamwise velocities obtained at the vertical and top boundaries. The presence of a wall at the bottom boundary of the measurement volume negatively affects the this estimate, therefore some part of the vertical boundaries near the bottom has been skipped to exclude the wall effects. The blue dashed line shown in Fig. 4.7(a) shows the part of the boundary that has been used to compute $W_{\infty_{PTV}}$. The optimum skipping distance is the one where $W_{\infty_{PTV}}$ reaches a converged value (Fig. 4.7(b)).

Freestream corrections for incoming flow

The control volume method, ideally, requires two velocity measurements - one at the incoming plane 1 (U_∞) and one at the outflowing plane 2 (u) (see Fig. 2.9). However, it is assumed that the freestream velocity at the outflowing plane 2 is equal to the velocity measured on the incoming plane 1. This may hold true in closed test sections with very low blockage models, however, in case of open jet tunnels this is not true. Due to the expansion of the jet flowing out of a nozzle into an open chamber (shown in the schematic 2.9) the velocity of the flow decreases. These effects are larger in the presence of bluff objects, such as in this case, and lead to large deviations in the loads measured by the control volume method described in

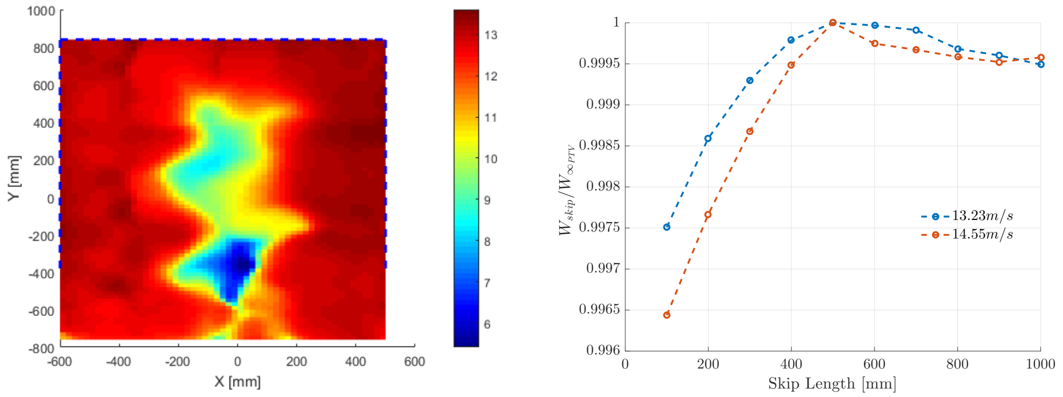

(a) (b)

Figure 4.7: (a) W_∞ obtained by averaging the streamwise velocities shown at the position of the blue dashed line on the boundary. (b) W_∞ converges to a value upon increasing the skipping distance from the floor (shown for two velocities, $13.23m/s$ and $14.55m/s$, normalized by the maximum values obtained).

section 2.6 if left uncorrected. Mercker and Wiedemann [49] have suggested corrections to account for the expansion of the jet that typically occurs in Open-Jet wind tunnels.

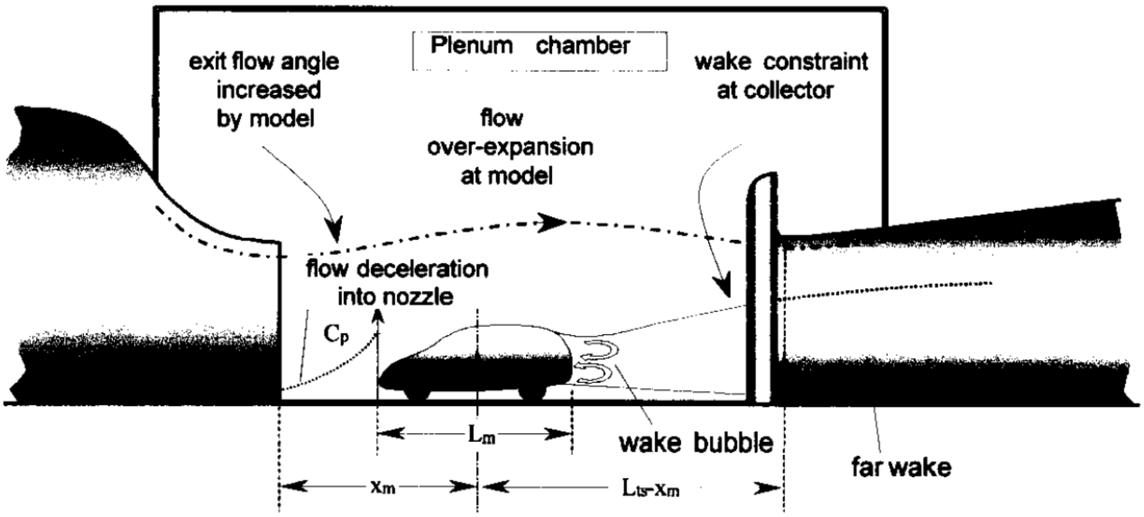

Figure 4.8: Schematic of flow over a model in an Open-Jet Wind Tunnel. Adapted from Agardograph 336 [13].

Out of the four major effects identified in the open jet tunnels, only the Jet Expansion and the Nozzle Blockage corrections are relevant in this case. Other interference effects such as the Collector Blockage and Empty-Tunnel Pressure Gradients are assumed to be negligible due the large distance between between the model centre and the collector ($L_{ts} - x_m$, see Fig. 4.8).

1. Jet Expansion: Large pressure differences between the flow and ambient air in the chamber causes the jet to expand outwards as shown in Fig. 4.8. This causes an increase in the flow cross-section as the flow moves downstream over and beyond the model, thus, causing it to decelerate following the continuity. Thus, the flow upstream to the model (plane 1) is corrected according to the correction factor:

$$\epsilon_S = \tau\sqrt{\frac{V_M}{L_m}}\left(\frac{A_m}{A^{*3/2}}\right) \tag{4.13}$$

where $\tau = -0.206$ is the tunnel shape factor for a circular tunnel obtained from Agardograph 109 [25]. V_m, A_m and L_m are the model volume, frontal area and the length respectively. A^* is the effective nozzle area given by:

$$A^* = \frac{A_N}{(1+\epsilon_{qn})} \tag{4.14}$$

Here, A is the nozzle exit area and ϵ_{qn} is the nozzle blockage factor given by:

$$\epsilon_{qn} = \frac{A_m}{2A_N}\left(\frac{1-x_s}{\sqrt{x_s^2+R_N^2}}\right) \tag{4.15}$$

The two terms x_s and R_N are evaluated as follows:

$$x_s = \frac{x_m + L_m}{2+\sqrt{\frac{A_m}{2\pi}}}, R_N = \sqrt{\frac{2A_N}{\pi}} \tag{4.16}$$

2. Nozzle Blockage: Presence of the bluff model in close proximity to the nozzle decreases the effective nozzle exit area causing the flow to accelerate. The high pressure present upstream of the model causes an increase in the exit flow angle further enhancing the jet expansion effects. This effect increases as the model moves closer to the nozzle. The correction factor for the nozzle blockage corrections is given as:

$$\epsilon_N = \frac{\epsilon_{qn}R_N^3}{(R_N^2 + x_m^2)^{3/2}} \tag{4.17}$$

Table 4.4 shows all the parameters used for the corrections of the freestream velocities in this study.

The time-averaged freestream velocity $W_{\infty_{PTV}}$ measured on the 4D-PTV measurement plane (plane 2) is then corrected to obtain the in the incoming freestream velocity W_∞ on plane 1 as follows:

$$\frac{W_\infty}{W_{\infty_{PTV}}} = 1 + \epsilon_S + \epsilon_N \tag{4.18}$$

Correction Parameters			
τ	-0.206	A^*	$14.652\ m^2$
L_m	$1.71m$	x_s	$0.1786m\ (1.43m^\dagger)$
A_m	$0.629\ m^2$	R_N	$2.183m$
V_m	$1.075\ m^3$	ϵ_{qn}	0.0214
A_N	$14.966\ m^2$	ϵ_S	-0.00183
x_m	$1.35m\ (2.60m^\dagger)$	ϵ_N	$0.01320\ (0.0057^\dagger)$
$\frac{W_\infty}{W_{\infty_{PTV}}}$	1.0114	$\frac{W_\infty}{W_{\infty_{PTV}}}^\dagger$	$1.0039^\dagger$

Table 4.4: Parameters for freestream corrections. † Experimental campaign 2

4.4.2. Reynolds stress term

The Reynolds stresses are a result of the Reynolds decomposition and time averaging of the continuity and the momentum equations. The non-linear convective terms are primarily responsible for the Reynolds stresses [66]. The fluctuating part of each velocity component is used for computing these Reynolds stresses. Since, this operation is performed on an ensemble of all the uncorrelated samples, it results in time-averaged Reynolds stresses, indicated by the overbar on the fluctuating velocity terms in the following equations:

$$RS_{xx} = \frac{1}{n}\sum_1^n \overline{u'^2}, \quad RS_{yy} = \frac{1}{n}\sum_1^n \overline{v'^2}, \quad RS_{zz} = \frac{1}{n}\sum_1^n \overline{w'^2}, \tag{4.19}$$

$$RS_{xy} = \frac{1}{n}\sum_{1}^{n}\overline{u'v'}, \quad RS_{xz} = \frac{1}{n}\sum_{1}^{n}\overline{u'w'}, \quad RS_{yz} = \frac{1}{n}\sum_{1}^{n}\overline{v'w'} \tag{4.20}$$

The fluctuating components of the velocities are obtained as follows:

$$\overline{u'} = \sum_{i=1}^{n_b}\frac{(u_i - \overline{u})}{n_b}, \quad \overline{v'} = \sum_{i=1}^{n_b}\frac{(v_i - \overline{v})}{n_b}, \quad \overline{w'} = \sum_{i=1}^{n_b}\frac{(w_i - \overline{w})}{n_b} \tag{4.21}$$

where n_b are the number of particles found in the bin under consideration.

Eq. 4.12 indicates that the Reynolds stress term generated by the fluctuating streamwise velocity component in the streamwise direction contributes towards a reduction in the drag (note the minus sign). Thus, Re_{zz} is evaluated in every bin and summed up to obtain the total Reynolds stress term in the drag equation.

4.4.3. Pressure term

The third term in Eq. 4.12 represents the pressure term. Simply stated, it is an integration of the pressure difference between the incoming flow and the pressure at all the locations in the wake. In this experiment the pressures were not measured in the wake explicitly. Pressure field in the wake is reconstructed from the velocity field obtained from PTV using the methodology provided by van Oudheusden [74]. This being a three dimensional measurement, the out-of-plane velocity gradients are available. Considering the steady state pressure gradient equations given by van Oudheusden [74] and neglecting the viscous terms owing to the high Reynolds numbers (Murai et. al.[52]):

$$\frac{\partial\overline{p}}{\partial x} = -\rho\left\{\overline{u}\frac{\partial\overline{u}}{\partial x} + \overline{v}\frac{\partial\overline{u}}{\partial y} + \overline{w}\frac{\partial\overline{u}}{\partial z} + \frac{\partial\overline{u'^2}}{\partial x} + \frac{\partial\overline{u'v'}}{\partial y} + \frac{\partial\overline{u'w'}}{\partial z}\right\} \tag{4.22}$$

$$\frac{\partial\overline{p}}{\partial y} = -\rho\left\{\overline{u}\frac{\partial\overline{v}}{\partial x} + \overline{v}\frac{\partial\overline{v}}{\partial y} + \overline{w}\frac{\partial\overline{v}}{\partial z} + \frac{\partial\overline{u'v'}}{\partial x} + \frac{\partial\overline{v'^2}}{\partial y} + \frac{\partial\overline{v'w'}}{\partial z}\right\} \tag{4.23}$$

$$\frac{\partial\overline{p}}{\partial z} = -\rho\left\{\overline{u}\frac{\partial\overline{w}}{\partial x} + \overline{v}\frac{\partial\overline{w}}{\partial y} + \overline{w}\frac{\partial\overline{w}}{\partial z} + \frac{\partial\overline{u'w'}}{\partial x} + \frac{\partial\overline{v'w'}}{\partial y} + \frac{\partial\overline{w'^2}}{\partial z}\right\} \tag{4.24}$$

Equations 4.22-4.24 suggest that the time-averaged pressure gradients can be obtained from time-averaged velocity fields, velocity gradients and the gradients of the Reynolds stresses. The gradients are computed using a finite difference scheme on the generated Cartesian grid according to the following equations:

$$\frac{\partial\overline{V}}{\partial x} = \frac{\overline{V_{i+1,j,k}} - \overline{V_{i-1,j,k}}}{2\Delta x} \tag{4.25}$$

where $\overline{V} = \{\overline{u}, \overline{v}, \overline{w}\}$. i, j and k are the indices of the bins in X, Y and Z directions respectively. $\Delta x, \Delta y$ and Δz is spacing between the vectors in the respective directions.

Similarly the the gradients of the Reynolds stresses are obtained as:

$$\frac{\partial RS}{\partial x} = \frac{RS_{i+1,j,k} - RS_{i-1,j,k}}{2\Delta x}, \tag{4.26}$$

where $RS = \{RS_{xx}, RS_{yy}, RS_{zz}, RS_{xy}, RS_{xz}, RS_{yz}\}$ are obtained from Eq. 4.19-4.20.

The pressure gradients evaluated through Equations 4.22-4.24 are provided to the Poisson solver algorithm which solves the equation $ap = RHS$ iteratively.

Boundary Conditions

Boundary Conditions		
Top Side	Dirichlet	$p = p_\infty$
Left Side	Dirichlet	$p = p_\infty$
Right Side	Dirichlet	$p = p_\infty$
Bottom Side	Neumann	$\frac{\partial p}{\partial y} = 0$

Table 4.5: Pressure boundary conditions

RHS contains the pressure gradients in the domain obtained through Equations 4.22, 4.23 and 4.24. The boundary conditions are specified by substituting the corresponding elements in the RHS column vector by the known values of the pressures and pressure gradients at the boundaries. The boundary conditions used here are given in Table 4.5. These boundary conditions are based on the assumption that the non-bounded boundaries are at freestream conditions (p_∞ is the freestream pressure). The wall bounded boundary (Bottom Side) has been assigned the Neumann boundary condition because of the reason explained as follows:
Consider the steady state momentum equation in the Y-direction (neglecting the viscous terms for high Reynolds Number flows):

$$-\frac{1}{\rho}\frac{\partial p}{\partial y} = u\cancelto{0}{\frac{\partial v}{\partial x}} + \cancelto{0}{v}\frac{\partial v}{\partial y} + w\cancelto{0}{\frac{\partial v}{\partial z}} \tag{4.27}$$

At the wall, the vertical velocity (v) is equal to zero (impermeable wall). Further, the gradients of the vertical velocity in the plane of the bottom wall are zero (since v is zero everywhere on the wall).

The reconstructed pressure $\overline{p}$ in the measurement volume is then used to calculate the coefficient of pressure as follows:

$$C_p = \frac{\overline{p} - p_\infty}{\frac{1}{2}\rho W_\infty^2} \tag{4.28}$$

5

Results and Discussion

This chapter presents the results obtained from the 4D-PTV measurements. As shown in Fig. 5.1, by combining the particle tracks from different locations in the measurement volume and applying the data reduction techniques described in Chapter 4 a time-averaged velocity field is obtained.

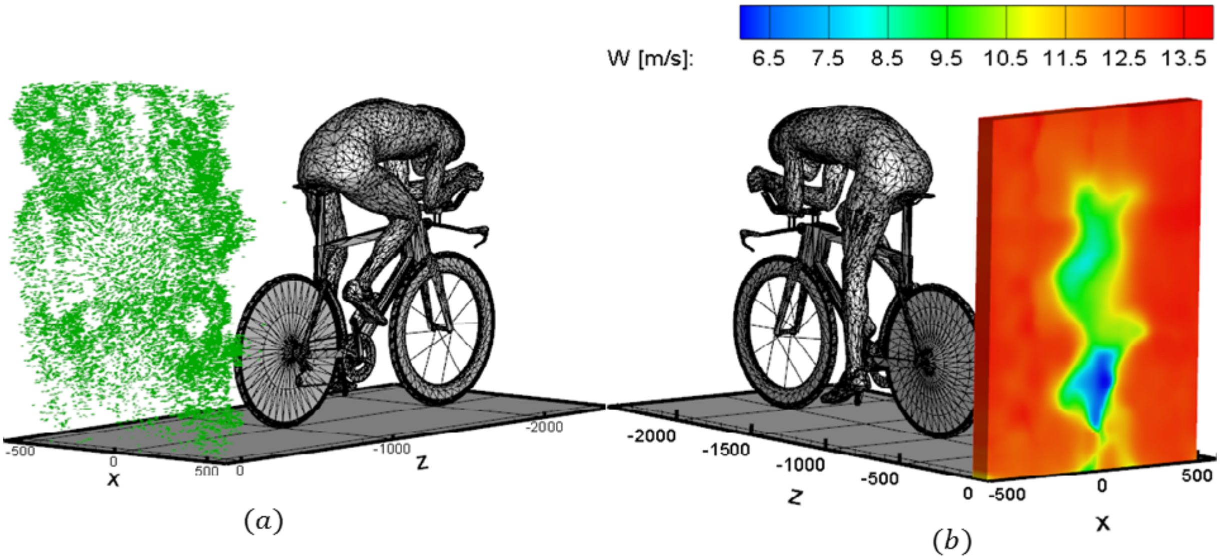

(a)

(b)

Figure 5.1: (a) Particle tracks obtained in the measurement volume. Combination of 1 cycle at each seeder position. (b) Time-averaged streamwise velocity (w) obtained from 480 cycles

The aim of this chapter is to, firstly, validate the flow-fields by comparing them to the literature, especially with the measurements of Terra et.al. [67] and Crouch et.al. [15, 16]. Section 5.1 discusses the flow-field in detail and enables this comparison.

Secondly, the dynamic quantities, such as pressure and the drag force, are evaluated from the three-dimensional velocity fields and presented in section 5.2. A comparison between the drag forces obtained from the PTV measurements and the balance measurements is made later in section 5.3.

5.1. Flow Kinematics

This section discusses the motion of air in the wake of the cyclist in a time-averaged sense. Three-dimensional flow-fields obtained from 4D-PTV at the typical time-trial speeds are presented. Development of vortical structures and their interaction with the flow-field is discussed.

5.1.1. Velocity vector fields

The wake, as schematically shown in Fig. 2.9, is a region where the streamwise velocities are lower than the freestream velocity. It must be noted that the measured velocities are strongly dependent on the distance of the measurement plane from the model. Fig. 5.2(a) shows that the streamwise velocities in the wake of a cyclist can drop to as low as 45% of the freestream velocity at a distance of 800mm from the rear-most point on the saddle. From Fig. 5.2(a), the distinction between the wake and the freestream can be clearly observed. The lowest velocities are obtained directly behind the rear wheel and the casette assembly. Furthermore, low streamwise velocity regions are observed behind the calves of the stretched leg as well as behind the saddle. These observations are in agreement with the observations reported by Terra et.al. [67].

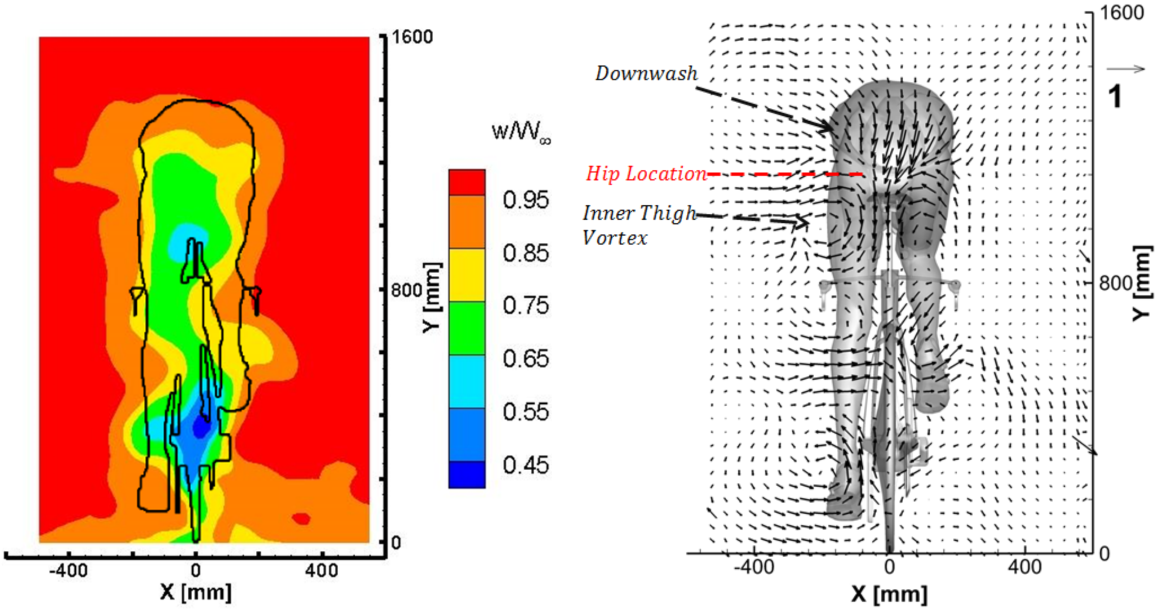

(a) (b)

Figure 5.2: (a) In-plane velocity vectors. (b) Non-dimensionalized streamwise velocity (w/W_∞). Showing time-averaged results over 480 uncorrelated samples on $Z = 0$ plane (located $800mm$ downstream from the saddle).

The magnitudes of the in-plane velocity components (see. Fig. 5.2(b)) are much lower than the out-of-plane (streamwise) component. The *upper hip vortex pair* observed by Crouch et.al. [16] in the near wake is no more visible as a vortex at this location, probably due to decay or ”cross-diffusive annihilation” (Crouch et.al. [16]). However, the figures show the presence of a strong *downwash* arising from the curved back of the cyclist which is at similar locations to that observed by Crouch et.al. Furthermore, it is important to note that the orientation of the upper body significantly affects the flow over the back. The *angle of attack* (acute angle made by the torso with respect to the horizontal) in case of the model used by Crouch et.al. was larger than that for the mannequin used in this study. Lower angle of attack would significantly reduce the strength of the *upper hip vortex pair* on this model.

The *inner thigh vortex* is clearly visible below the location of the hips. Similarly, other flow features such as flow entrainment into the low-pressure wake and formation of vortical structures near both feet are clearly visible from Fig. 5.2(b).

5.1.2. Wake structure

The wake is composed of multiple vortices of varying strengths and sizes. This is observed by using the vortex identification tools described in Chapter 4. Streamwise vorticity (ω_z, Eq. 4.7) shows multiple counter-rotating vortex pairs at the location of the hips, thigh, lower leg and the feet (see Fig. 5.3). The presence of some of these vortices is in agreement with the literature and is discussed in this section.

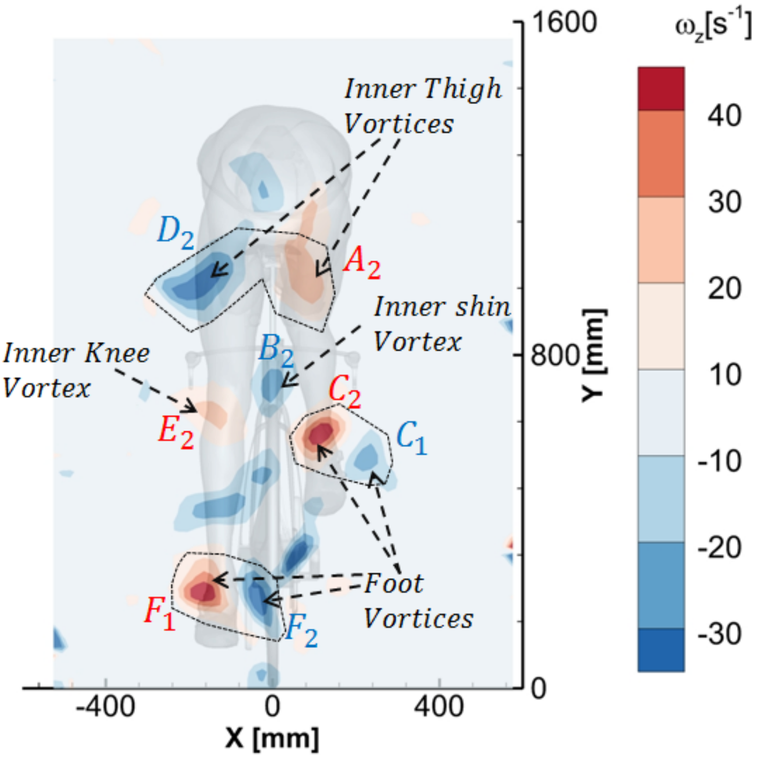

Figure 5.3: Streamwise vorticity (ω_z). Showing time-averaged results over 480 uncorrelated samples on $Z = 0$ plane. Counter-rotating vortex pairs shown in black dashed outline. Labels are defined in Fig. 5.5

The Reynolds Numbers based on the widest diameters of the limbs lie in the sub-critical region resulting in a laminar separation (see Fig. 1.4). Thus, it may be expected that the flow over these limb sections is laminar. The direction of vortices emanating from the limbs may, thus, be explained by the laminar separation mechanism over a cylinder as described in Fig. 1.6(b). As the vortices are formed in the plane of the cross-section of the cylinder the vorticity is oriented in the direction parallel to the axis of the cylinder. This holds true even for the cylinder that is inclined to the direction of the flow. Consider the cylinder inclined to the direction of the flow in two different orientations - inclined *towards* or *away* from the flow direction. Following the above observation and decomposing the vorticity along the streamwise direction (as only ω_z is of interest here) Fig. 5.4 schematically shows the orientation of the streamwise vortices emanating from a cylinder inclined to the direction of the flow. The schematic shows that the laminar separation mechanism leads to a specific direction of the streamwise vorticity ω_z on either side of the inclined cylinder that is solely dependent on the sign of the inclination angle (θ). φ is the azimuthal angle on the XZ plane as shown in Fig. 5.4. Using this sign convention as a rule of thumb and looking in the direction of the flow (Z direction), the direction (sign) of ω_z is derived as follows:

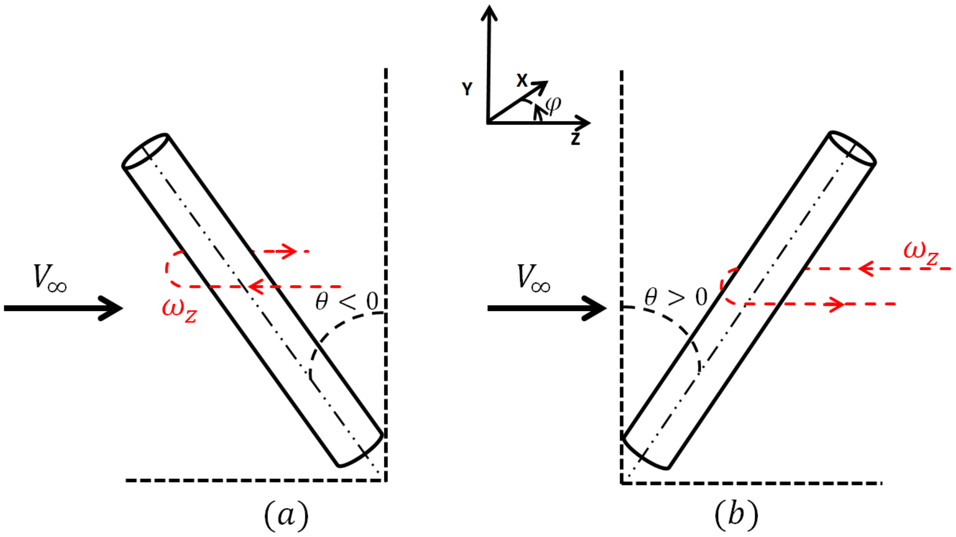

Figure 5.4: Schematic for the direction of the streamwise vorticity (ω_z) depending on the orientation of an inclined infinite cylinder with respect to the freestream velocity V_∞ (a) Inclined away from flow direction ($\theta < 0$) (b) Inclined towards the flow direction ($\theta > 0$)

$$\omega_z = \begin{cases} + & 0 \leq \varphi < \pi, \theta < 0 \\ - & \pi \leq \varphi \leq 2\pi, \theta < 0 \\ - & 0 \leq \varphi < \pi, \theta > 0 \\ + & \pi \leq \varphi \leq 2\pi, \theta > 0 \end{cases} \tag{5.1}$$

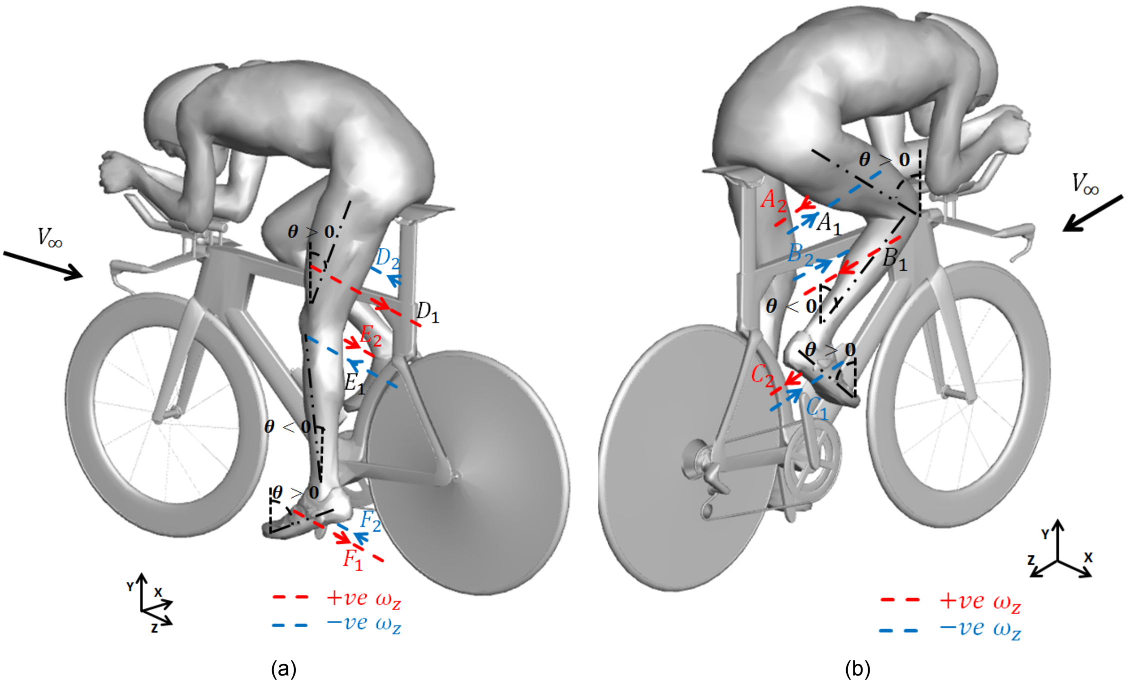

Figure 5.5: Shows the direction of the streamwise vorticity from different parts of the leg as expected according to the schematic shown in Fig. 5.4 (a) Stretched leg (b) Raised leg. Color coding as shown in the figure. Only those labels are colored in Red or Blue which are marked in Fig. 5.3.

Based on this rule of thumb, the directions of the streamwise vortices emanating from the different sections of the leg are shown in Fig. 5.5(a) and 5.5(b). Whether ω_z is positive or negative is directly dependent on the orientation of the different sections of the leg with respect to the flow direction. This fact may yield interesting insights on the points of origination of the vortices observed in Fig. 5.3.

Note that the vortices are considered to originate only from the different sections of the lower body. From Fig. 5.2(b) it has been established that the *upper hip* vortices dissipate until they reach the measurement plane in this study. Other vortices that might originate on the upper body may either merge or annihilate with the vortices originating on the lower body.

Streamwise vortices, as expected due to the laminar separation mechanism, are labelled A through F in Fig. 5.5. Those vortices emanating from the outer sides (away from the bike frame) have the subscript 1 and those emanating from the inner side (close to the frame) have the subscript 2.

Foot Vortices

The feet of the mannequin are inclined in the direction of the flow, thus resulting in the positive ω_z on the left side and negative ω_z on the right side, while looking upstream (see Fig. 5.4(b) for analogy). Thus, streamwise vortices C_1, C_2 and F_1, F_2 are expected from the right and the left foot respectively as shown in Fig. 5.5.

Fig. 5.3 shows the presence of these vortices in the expected locations and according to the expected directions. This also verifies that the foot vortices arise due to the laminar separation mechanisms. Here, it is also important to note that these vortices must not be considered as *horseshoe* vortices originating from the *ankle* as the direction of a horseshoe vortex pair would be opposite to that of the observed vortex pair.

Shin Vortices

It may be observed from the Fig. 5.5 that both the shins of the mannequin are orientated away from the flow direction ($\theta < 0$). Thus, the streamwise vortices emanating from the shins (B_1, B_2 and E_1, E_2) have their directions opposite to the foot vortices.

Fig. 5.3 shows the presence of two of these four predicted vortices. The vortex directly in the wake of the stretched leg has positive vorticity. This suggests that it might be the E_2 vortex as predicted from the inner thigh/knee of the stretched leg. Similarly, the negative vorticity of the other vortex leads to the conclusion that it emanates from the inner portion of the raised thigh (B_2). It is interesting to observe that the streamwise vortices from the outer portion of the shin are absent in all the previous studies (see Fig. 5.10, 5.11) as well as in this study. It must be noted that the consideration of the leg as a cylinder is an approximation. Moreover, the vortex shedding schematic described earlier does not consider the influence of other objects in the neighbourhood, such as other sections of the leg, upper body or the bike. Hence, some of the vortices may not be formed in reality.

Thigh Vortices

Again, Fig. 5.5 suggests that the thighs of the mannequin are orientated in the direction of the flow ($\theta > 0$) leading to the same directionality of the streamwise vortices (A_1, A_2 and D_1, D_2) as of the foot vortices.

Here, again, only two out of the four expected vortices are present. Using the sign convention suggested in Fig. 5.5, it may be concluded that the vortex behind the stretched leg is the one which arises from the inner thigh (D_2) as it has negative vorticity. Similarly, the vortex behind the raised thigh must arise from the inner portion (A_2) since it has positive vorticity. Crouch et.al. [16] too have observed the presence of a vortex originating near the inner thigh of the raised leg [16]. Points of origination of all the aforementioned vortices are observed by Jux 2017 [37].

Q-criterion

Fig. 5.3 shows non-zero vorticity at other locations, such as the back arch and the calf of the stretched leg. Here, the vorticity criteria is misleading for the identification of vortices as the observed velocity gradients are only due to shearing motions (see Fig. 5.6). Therefore, the Q-criterion is used to identify the true vortices ($Q > 0$).

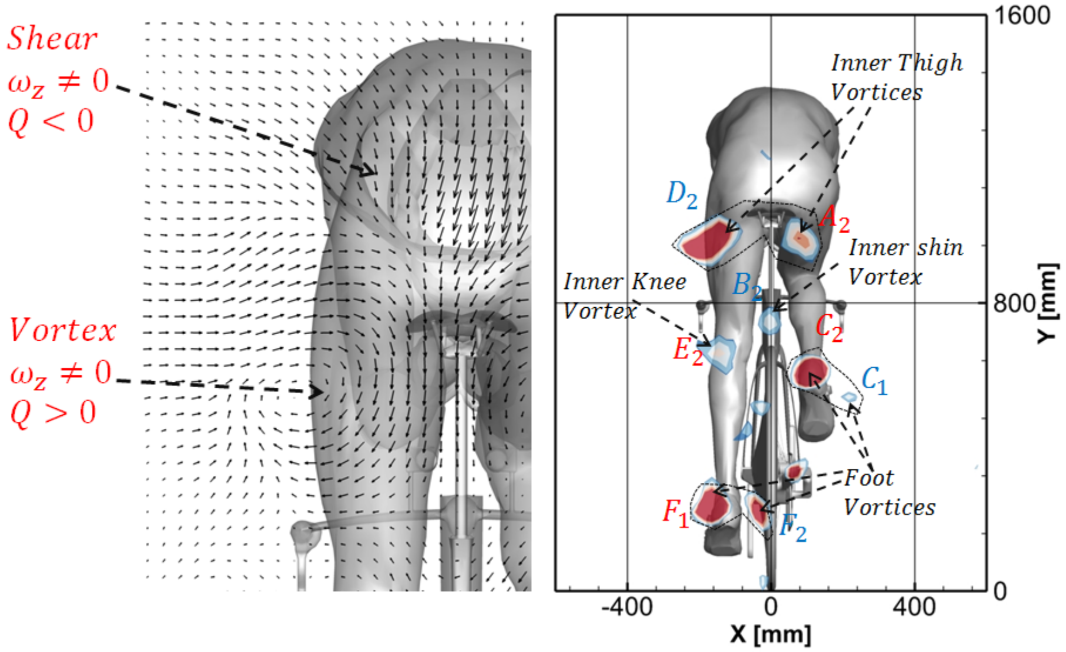

(a) (b)

Figure 5.6: (a) Distinction between swirling and shearing motions. (b) Q (Eq. 4.11) plotted throughout measurement volume. Showing time-averaged results over 480 uncorrelated samples on $Z = 0$ plane.

Fig. 5.6(b) confirms the presence of the vortices marked in Fig. 5.3 as they are associated with the positive value of Q. Furthermore, it also shows presence of tiny secondary vortices that probably originate at various parts of the bike such as the casette (below right foot) and the frame parts.

The downwash from the upper part of the back and the flow going around inner thigh vortex (D_2) cause shearing motions in that region. This is elicited by the absence of positive Q values near the back arch. They, further, validate the absence of the upper-hip vortices at this measurement location.

5.1.3. Pressure fields

Firstly, the static pressure fields are evaluated by solving the Pressure Poisson Equation (Eq. 2.16) using the three dimensional velocity field data. The pressure fields are validated using the vorticity fields. The vortex core must have lower pressure than the ambient pressure. Thereafter, the pressure term is computed using these validated pressure fields.

Fig. 5.7(a) shows the presence of low pressure regions at the locations of the vortices observed from Fig. 5.6. This is consistent with the theory of vortices. Labels from Fig. 5.6 are

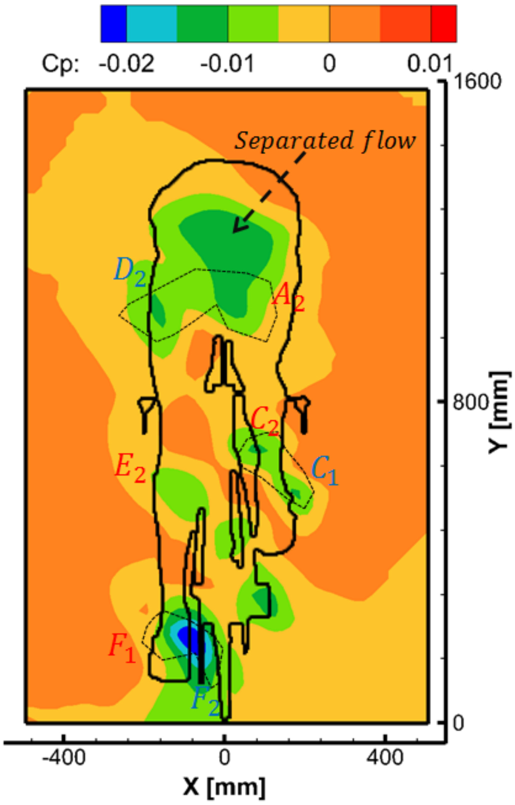

Figure 5.7: Pressure coefficient obtained from current study (Time-averaged over 480 uncorrelated samples on $Z = 0$ *plane)*

marked for validation. For example, the vortex cores for the foot vortices C_1, C_2 are captured separately. However, the same is not true for the foot vortices F_1, F_2. This may be attributed to the close proximity of the vortices F_1, F_2 to each other. Furthermore, the large low pressure region at the lower back is also observed. This low pressure region is likely to arise from the separation of the flow over the back.

The magnitudes of the pressure coefficient are much lower than those obtained in the study by Terra et.al. [67]. It must be noted that the pressure fields are extremely sensitive to the velocity gradients in the measurement domain and the applied boundary conditions. The difference in the pressure fields between the two studies may be attributed to the higher positional accuracy and the absence of boundary effects obtained through 4D-PTV as compared to the Tomographic PIV which results in a more accurate velocity field as well as their gradients.

5.1.4. Comparison with literature

Previous studies by Crouch et.al. [15, 16] and Terra et.al. [67] are used to compare and identify the similar flow features and validate the results obtained from this study. Firstly, the velocity fields are validated by comparing the magnitudes of the streamwise velocities at various locations in the wake. Secondly, large-scale structures are qualitatively validated by comparing the signs of the streamwise vortices and their locations with respect to the model. Note that the left leg is raised (Crank angle 75°) in the case of Crouch et.al. [15, 16] whereas the right leg is raised in the study of Terra et.al. [67] and the current study.

Velocity fields

Fig. 5.8 shows the similarities in the streamwise velocity fields obtained from the current study and the previous study by Terra et.al. [67]. Scales have been made similar to effectuate direct comparisons between the non-dimensionalized velocities.

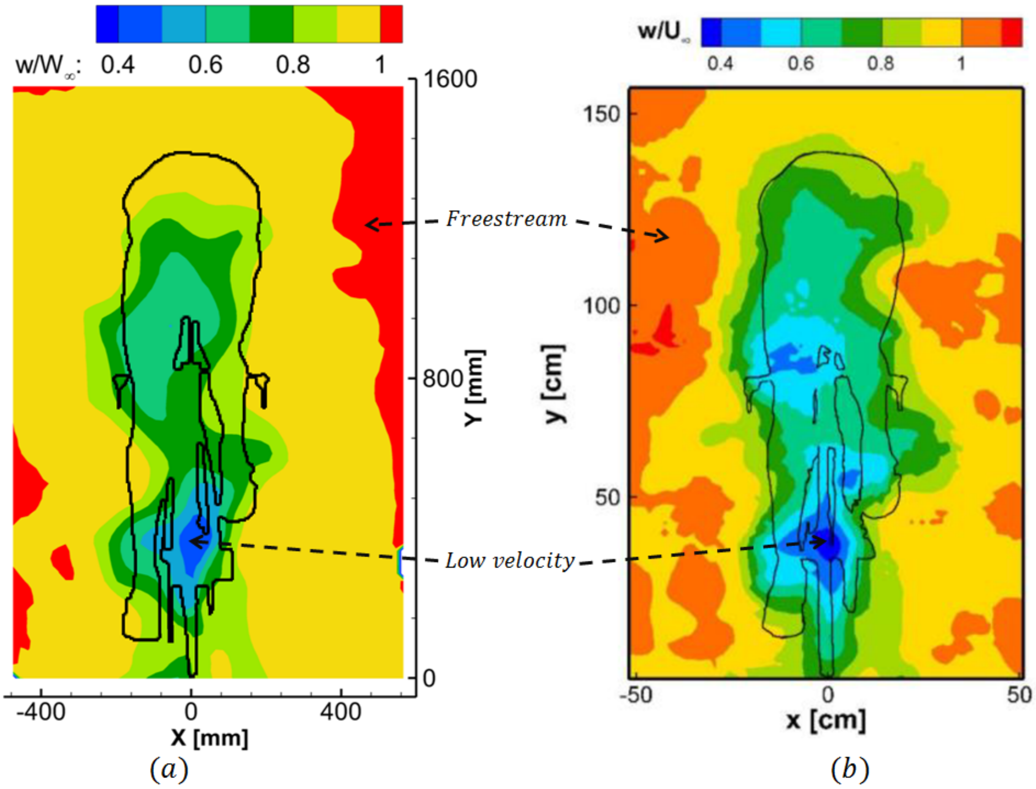

Figure 5.8: Non-dimensionalized streamwise velocity (w/W_∞) obtained from (a) Current study ($Re = 5.74 \times 10^5$) Showing time-averaged results over 480 uncorrelated samples on $Z = 0$ plane. (b) Terra et.al. [67] ($Re = 1.64 \times 10^5$)

Apart from minor differences in the size of the wake at various locations, the overall wake structure obtained from both the studies is similar. These differences may be attributed to the Reynolds number that is 3.5 times larger in the current study. Larger Re may result in an earlier transition, thus, leading to a delayed flow separation towards the rear portion of the back. This causes the momentum deficit to be lower causing the wake to contract. The velocities attain the freestream values towards the boundaries of the measurement plane.

Lowest velocities in the wake have similar locations but slightly different magnitudes. In general, the velocities observed in the current study are about 5% higher than those reported by Terra et.al [67]. This difference is clear at the lowest velocities near the rear wheel. In this study, the lowest velocity is 45% (Fig. 5.2(a)) of the freestream value whereas it is approximately 40% in the case of Terra et.al. This difference can, again, be observed by comparing the low velocity region obtained at the centre of the measurement plane (behind the thigh of the stretched leg) by Terra et.al. In this study, the velocities obtained in that region are about 10% higher than those reported by Terra et.al. Again, these differences are likely to arise from the different Reynolds Numbers used in these studies.

The wake structure in the range of the velocities examined is a close match as observed in Fig. 5.9. Although, minor differences are observable, they are not large enough to cause large variations in the drag areas. This observation is in agreement with the conclusions

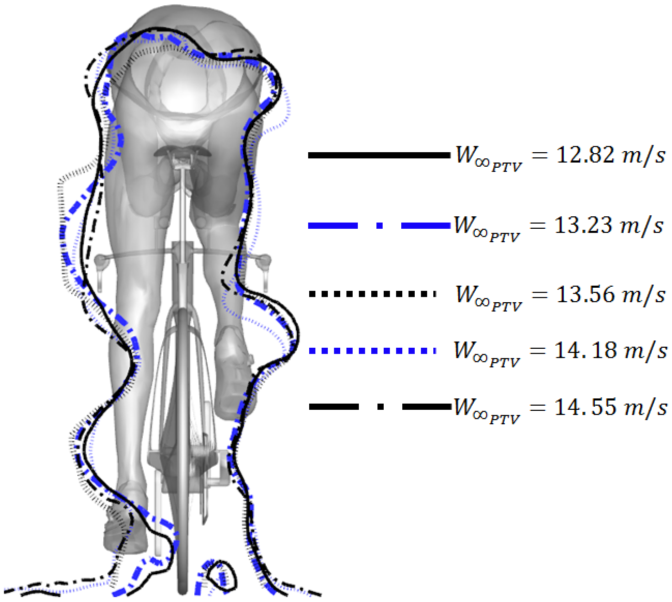

Figure 5.9: Contours of $w/W_\infty = 0.9$ for a range of incoming velocities. Results obtained from time-averaging over 480 uncorrelated samples on $Z = 0$ plane.

of Basset et.al. [5] for the given velocity range. This is confirmed by the C_DA computed in Table 5.1 which shows the maximum variation is within 2% from balance measurements and within 5% from the 4D-PTV measurements.

Vorticity fields

Vorticity fields are compared only qualitatively since the magnitude of the vorticity is dependent on the velocity and the grid sizes. However, the sign and the location of the streamwise vortices are directly comparable.

Crouch et.al. [15] reported the presence of upper and lower *hip vortices* (see Fig. 5.10(a)) as well as vortices from the lower parts of the leg (labelled as 'ankle-calf', Fig. 5.10(a)). In their previous study [16], they reported similar structures as *upper and lower hip vortices* (Fig. 5.11(a)). Additionally, they also observed the *inner thigh vortex* behind the left leg. Similar *hip vortices* were observed in the PIV measurements by Terra et.al. [67] (Fig. 5.10(b)). Furthermore, they clearly observed two large vortices, one from each of the feet.

In the current study (Fig. 5.11(b)), the streamwise vortices have been captured at similar locations in greater detail. Overall, the signs of the vortices are consistent with the previous literature. Firstly, it has been observed that the foot vortices, that were previously reported as a single vortex from each of the feet, are, in fact, two different vortices from each foot with opposite signs. This is consistent with the schematic of the vortex shedding over different leg sections shown in Fig. 5.5.

Secondly, *inner thigh vortex* and the *lower hip vortex* observed by Crouch et.al. [16] (Fig. 5.11(a)) behind the raised leg is also captured in the current study, however it has been labelled as the *inner thigh vortex*. This is because Crouch et.al. have observed the *hip vortices* arising from the lower portion of the back, primarily because of the slightly upright position of the model in their case. In this case, the lower angle of attack of the mannequin may have negatively affected the strength of such vortices from the lower back causing them to dissipate. The remnants of these vortices may still be observed in the form of the strong downwash observed in Fig. 5.2(b) and the non-zero vorticity near the back arch in Fig.

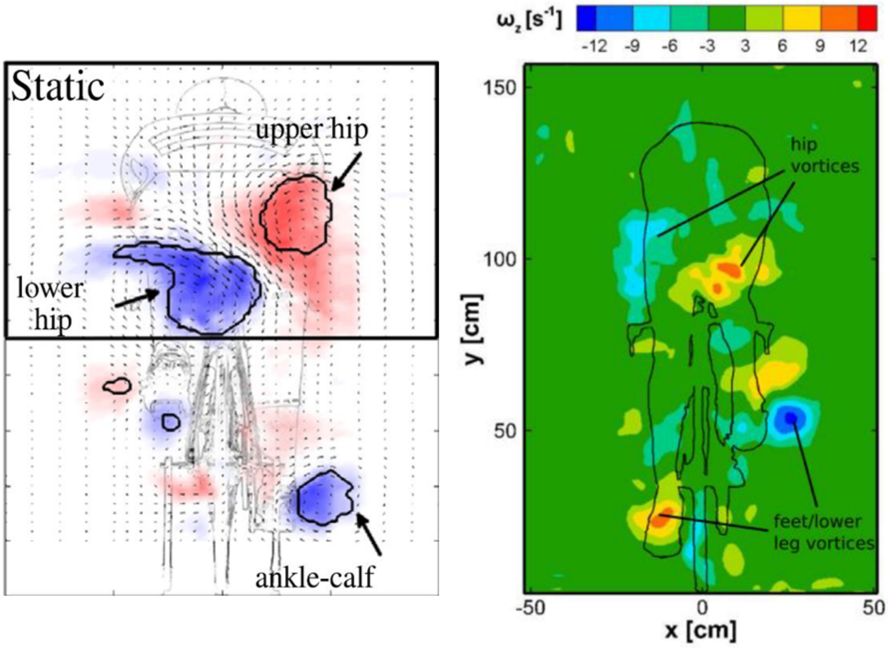

(a) (b)

Figure 5.10: Streamwise vorticity (ω_z) obtained from the studies of (a) Crouch et.al. [15] (Red is positive ω_z) (b) Terra et.al. [67]

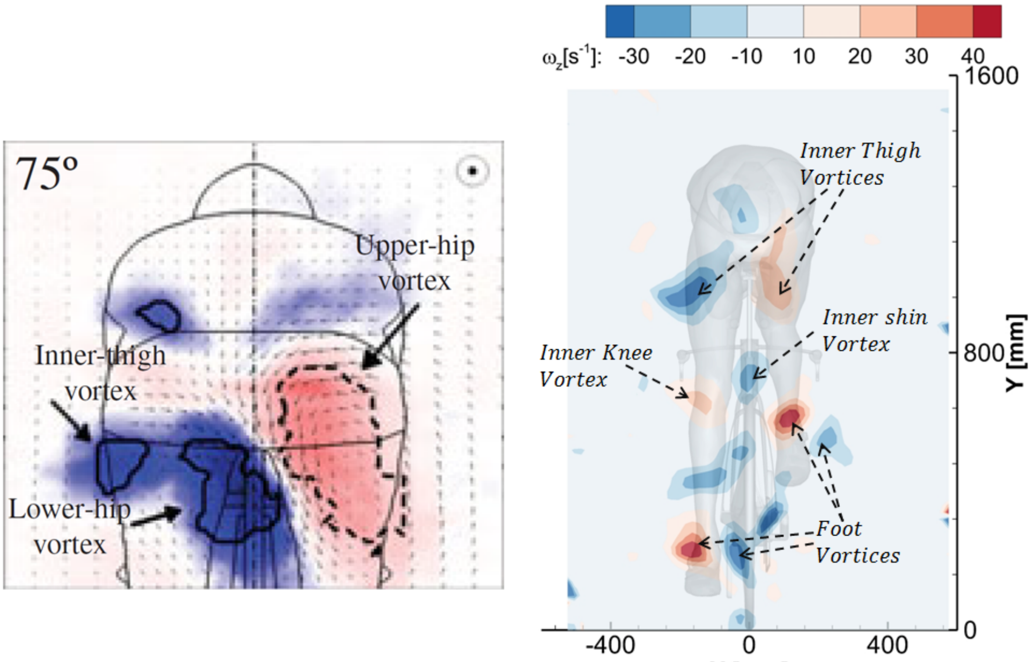

(a) (b)

Figure 5.11: Streamwise vorticity (ω_z) obtained from the study of (a) Crouch et.al. [16] (Red is positive ω_z) (b) Current study

5.11(b). Thus, it is speculated that the vortices labelled as the *inner thigh vortices*, indeed, originate from the inner thigh. Again, this is consistent with the vortex shedding schematic discussed earlier.

The orientation of these vortices is antisymmetric to those observed by Crouch et.al. [16] owing to the opposite leg position. However, the asymmetry caused in the flow near the lower back region due to the asymmetric leg positions compares well in Fig. 5.11.

Thirdly, a pair of counter-rotating vortices is observed at the knee height in the current study. These vortices are weaker than all the aforementioned vortices, which is a probable reason for their absence in the previous studies. Although, the results from Terra et.al. [67] show the presence of these vortices with a small magnitude. As argued in the previous subsection, these vortices emanate from the inner side of each of the shin/knee, hence labelled as *inner shin/knee vortex*. Asymmetry in the flow, with a strong component in the $-X$ direction, in the neighbourhood of these vortices may cause the *Inner knee/shin vortices* to move in that direction until they reach the measurement plane.

Having observed that the observed vortices are a result of the laminar separation mechanism, their points of origination may be located at the widest diameters of each of the leg sections. Note that the shin becomes thinner and, thus, streamlined as it moves from the knee to the ankle. Thus, the *inner shin vortices* are likely to originate closer to the knee, as observed.

Reynolds stress

Fig. 5.12(a) shows a large vertical region with high fluctuating components on the stretched leg as observed by Terra et.al. [67].

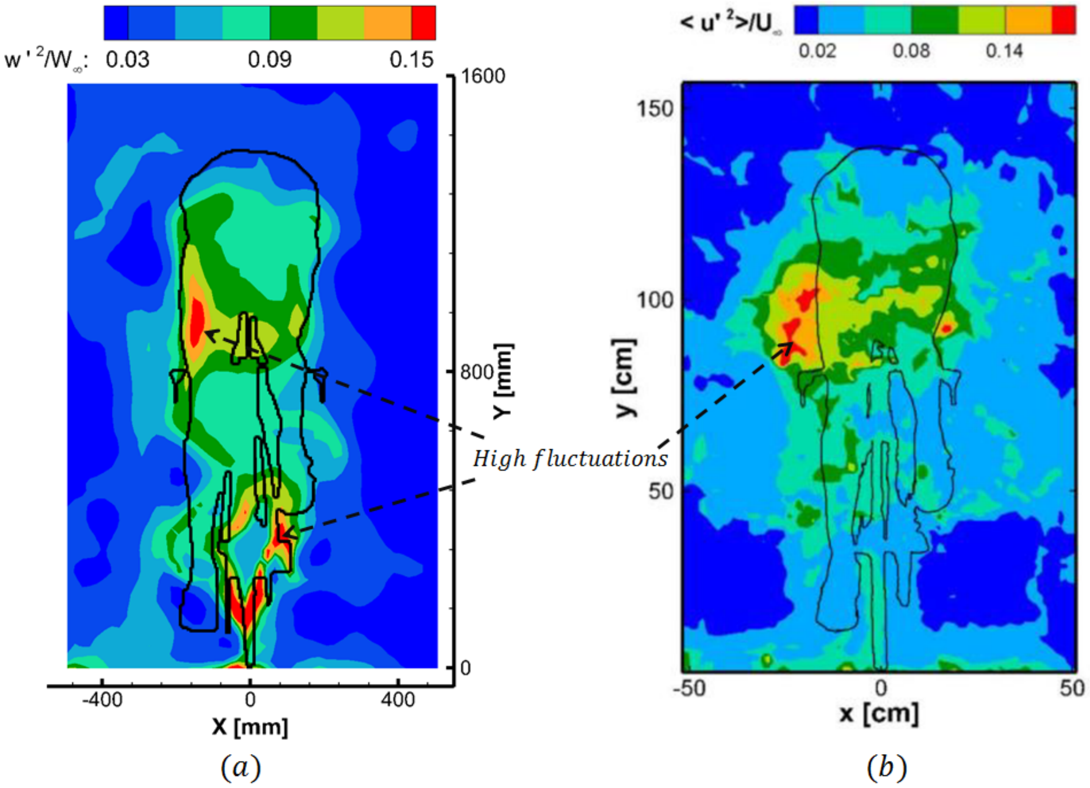

(a) (b)

Figure 5.12: Normalized streamwise Reynolds stress component (Re_{zz}) obtained from (a) Current study (Time-averaged over 480 uncorrelated samples on $Z = 0$ plane) (b) Terra et.al. [67]

The magnitudes of the fluctuations and the size of the fluctuating region is relatively smaller behind the raised leg, owing to the closed hip orientation that forms a smaller shear layer. In addition to this, regions of high fluctuating velocities are observed to arise from either side of the rear wheel as well as the casette. This may, again, be associated to the shear layer formed on these parts. As observed for the velocity fields, the close proximity of the rear wheel to the measurement plane may result in the fluctuations in that region to appear stronger than the those observed closer to the hips. The freestream , as expected, is much more steadier.

5.2. Flow Dynamics

This section presents the results for the dynamic quantities such as the static pressure and drag force. Each term in the drag equation (Eq. 4.12) is discussed separately in the following subsections.

5.2.1. Momentum term

The momentum term contributes the maximum to the total drag. The study of Terra et.al. [67] suggests that the momentum term contributes as much as 85% to the absolute sum of the drag components at a Reynolds Number of 1.64×10^5 (see Table 1.2). Fig. 5.13 shows the velocity deficits at different x-stations behind the stretched leg, raised leg and the centre-plane respectively.

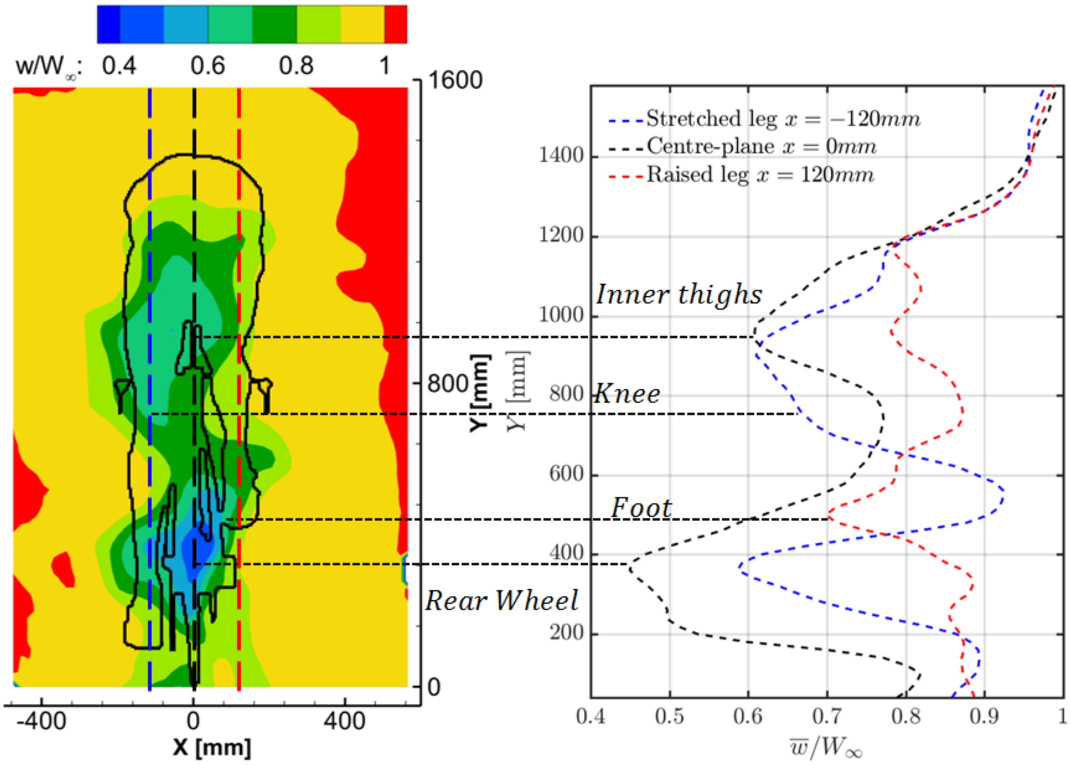

Figure 5.13: Normalized streamwise velocity profiles at different x-stations showing the effect of leg positions on the momentum deficit. (Time-averaged over 480 uncorrelated samples on $Z = 0$ plane)

From the Fig. 5.13 it may be observed that the velocity profiles in the wake of the stretched leg and the raised leg are dissimilar due to the asymmetrical leg positions. The overall shape of the velocity profile at the centre-plane is similar to the one behind the stretched leg, but with larger deficits. Large velocity deficits are clearly observed in the regions of the knees, inner thighs, feet and the rear wheel. These are also the regions that were identified earlier for the presence of vortical structures. The vortices are responsible for energy transfer from the streamwise velocity component to the in-plane components causing large momentum deficits in the streamwise direction thereby contributing to the total drag.

In this study, the momentum term was found to contribute in the range 93.9% to 95.65% to the absolute sum of the components, which is almost 8% to 10% higher than that reported by Terra et.al. This difference could be associated to the lower contribution from the pressure term and the different Reynolds Number used in this case.

5.2.2. Reynolds stress term

The Reynolds stress term is composed of the integral of fluctuating streamwise velocity components Re_{zz}. It contributes about 10% to the absolute sum of the drag components according to the study by Terra et.al. [67]. In that study they observed that the fluctuating components in the streamwise direction arose from the shear layers formed on the stretched leg. The orientation of the hip, open or close, was reported to produce large or small fluctuations respectively.

In this study, for the different freestream velocities the integral of Re_{zz} results in a contribution in the range of 4.1% to 5.75% to the absolute sum of the drag components. This is consistent with the fact that the Reynolds Stress is the second largest contributor, however like the pressure term, their magnitudes are much lower than those obtained by Terra et.al. [67].

5.2.3. Pressure term

The pressure term, one of the least contributors to the drag force, has been evaluated using the methodology described in section 2.6. From the study of Terra et.al. [67], the pressure term contributes about 3.6% to the absolute sum (see Eq. 1.2) of all the drag components at the location of the measurement plane considered. Absolute pressures in the wake are dependent on the distance of the measurement plane from the model. Closer to the model the pressures are much lower than the ambient pressures (P_∞). As the distance from the model is increased the pressures in the wake region gradually increase to P_∞. Thus, the pressure difference that is responsible for the pressure term in the drag equation is lower at a larger distance [68].

In this case, the measurement plane being approximately 2.2 HW (Table 3.1), the static pressures in the wake are found to be lower than the ambient pressures. However, the magnitudes of the associated pressure coefficients found in this study are much lower than those reported by Terra et.al. [67]. This causes their contribution to the drag force to be negligible with respect to the momentum and the Reynolds stress terms.

The pressure term contributes in the range 0.13% to 0.48% to the absolute sum of the drag components. Although it is lower than that obtained by Terra et.al. [67] it agrees with the fact that the contribution from the pressure term is the least at this location. Given such low magnitudes of the pressure term, it is safe to neglect it in the future experiments at this location.

5.2.4. Variation of drag components with velocity

Each component of the drag equation (Eq. 4.12) has been found to vary in a particular range as W_∞ is increased. The variation of these terms is shown in Fig. 5.14(a). Note that the figures show the variation of the drag components and the total drag force with respect to the corrected freestream velocity W_∞. Uncorrected freestream velocities measured by 4D-PTV can be found in Table 5.1 under the column $W_{\infty_{PTV}}$.

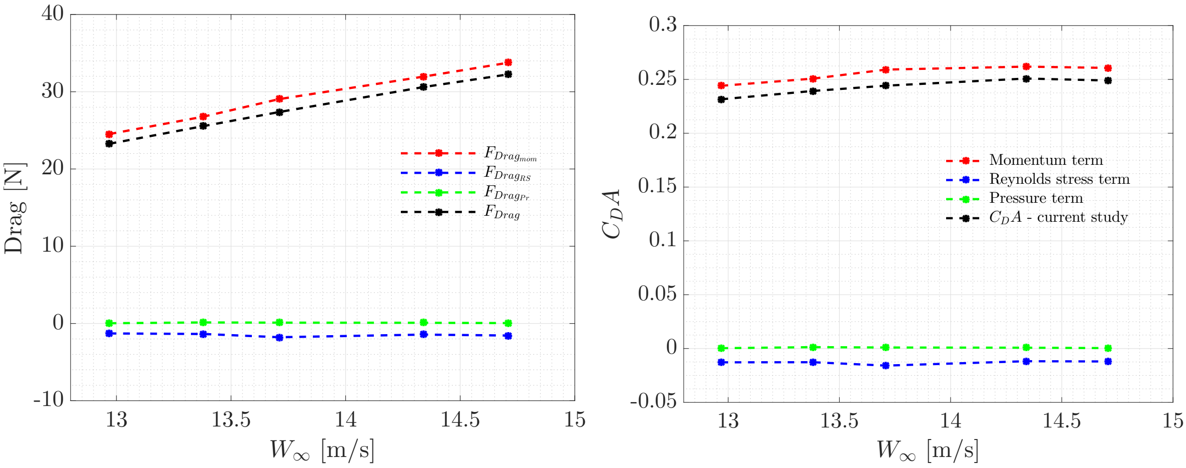

(a) (b)

Figure 5.14: (a) Variation of drag components from Eq. 4.12 with freestream velocity W_∞. (b) Variation of drag area C_DA with freestream velocity W_∞. Obtained from time-averaged results over 480 uncorrelated samples on $Z = 0$ plane after correcting W_∞ in each case.

Fig. 5.14(b) shows the variation of the drag areas corresponding to the respective drag components. Here, the drag areas have been obtained by dividing the respective components with the dynamic pressure measured by 4D-PTV ($q_{\infty_{PTV}}$). Moreover, this enables a comparison of the drag areas obtained in the study by Terra et.al. [67] since they followed a similar procedure (Fig.5.15). It is observed that the value for the drag area predicted by Terra et.al. [67] falls in the range of the values predicted from this study. It must be noted that the Reynolds Number in their case was a factor 3.5 smaller.

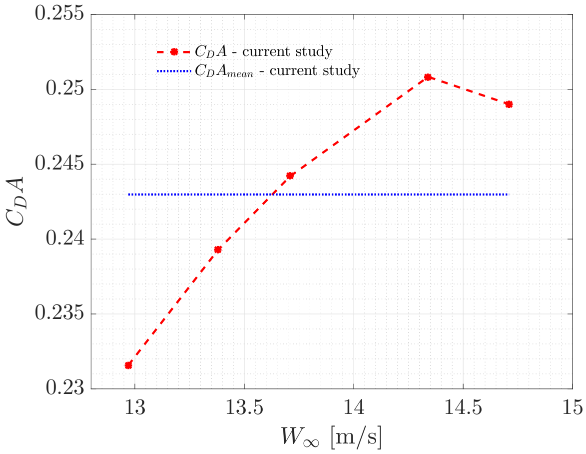

Figure 5.15: Comparison of drag areas obtained in this study. (Result from study of Terra et.al. [67] is shown only for comparison. Note that their study was performed at $4m/s$).

$W_{\infty_{OJF}}$ **[m/s]**	$W_{\infty_{PTV}}$ **[m/s]**	$q_{\infty_{PTV}}$ **[Pa]**	W_{∞} **[m/s]**	$F_{Drag_{mom}}$ **[N]**	$F_{Drag_{RS}}$ **[N]**	$F_{Drag_{Pr}}$ **[N]**	F_{Drag} **[N]**	$C_D A_{PTV}$	$C_D A_{bal}$
12.97 ± 0.01	12.82± 0.006	100.01 ± 0.10	**12.97± 0.006**	24.53	-1.29	0.03	23.23	**0.231**	0.235 ± 0.0015
13.48 ± 0.03	13.23± 0.010	106.80 ± 0.16	**13.37± 0.010**	26.78	-1.36	0.13	25.55	**0.239**	0.238 ± 0.0005
13.99 ± 0.02	13.56± 0.023	112.10 ± 0.38	**13.71± 0.023**	29.05	-1.78	0.10	27.37	**0.244**	0.243 ± 0.0007
14.50 ± 0.03	14.18± 0.007	123.06 ± 0.12	**14.34± 0.007**	31.96	-1.46	0.10	30.61	**0.251**	0.239 ± 0.0038
15.03 ± 0.01	14.55± 0.008	130.40 ± 0.14	**14.71± 0.008**	33.76	-1.56	0.05	32.24	**0.249**	0.236 ± 0.0020

Table 5.1: Results for drag and drag components.

W_{∞} **[m/s]**	$F_{Drag_{mom}}$ [%]	$F_{Drag_{RS}}$ [%]	$F_{Drag_{Pr}}$ [%]
12.97	**94.78**	5.10	0.12
13.37	**94.71**	4.81	0.48
13.71	**93.91**	5.75	0.34
14.37	**95.49**	4.22	0.29
14.71	**95.45**	4.41	0.14

Table 5.2: Contribution of the drag terms to the sum of absolute values in percentage

Table 5.1 shows the mean values of the velocities measured at the tunnel exit $W_{\infty_{OJF}}$ with the variations observed over 15 measurements. $W_{\infty_{PTV}}$ are the velocities obtained in the freestream (see Fig. 4.7) along with the mean of the variations observed in the corresponding bins at a 95% confidence level. These velocities are corrected according to the Open Jet Corrections given by Mercker and Wiedemann [49] to obtain the true incoming flow speeds W_{∞}. Variation in the incoming flow speeds causes a variation on the Momentum term ($F_{Drag_{mom}}$) as shown in Table 5.1. Finally, total drag force (F_{Drag}) and the drag areas (C_DA) along with corresponding variations are obtained.

Fig. 5.14 clearly shows that the contribution from the pressure term is close to zero and the contribution from the Reynolds stresses is almost constant in the velocity range. The total drag force has a similar trend as that of the momentum term. Thus, the entire variation in the drag force is solely captured by the momentum term. Moreover, from Table 5.2 it is observed that the momentum term makes up almost 95% of the absolute sum of all the components. Hence, it may be possible to predict the variation in the total drag of the cyclist by solely computing the momentum term.

5.2.5. Drag reduction based on flow-field

From Fig. 5.13 it may be observed that there are two reqions of large momentum deficits, one above the knee of the stretched leg and one below. The knee is nearly $700mm$ above the floor. Fig. 5.16 shows that the momentum term computed for each of these regions is nearly equal.

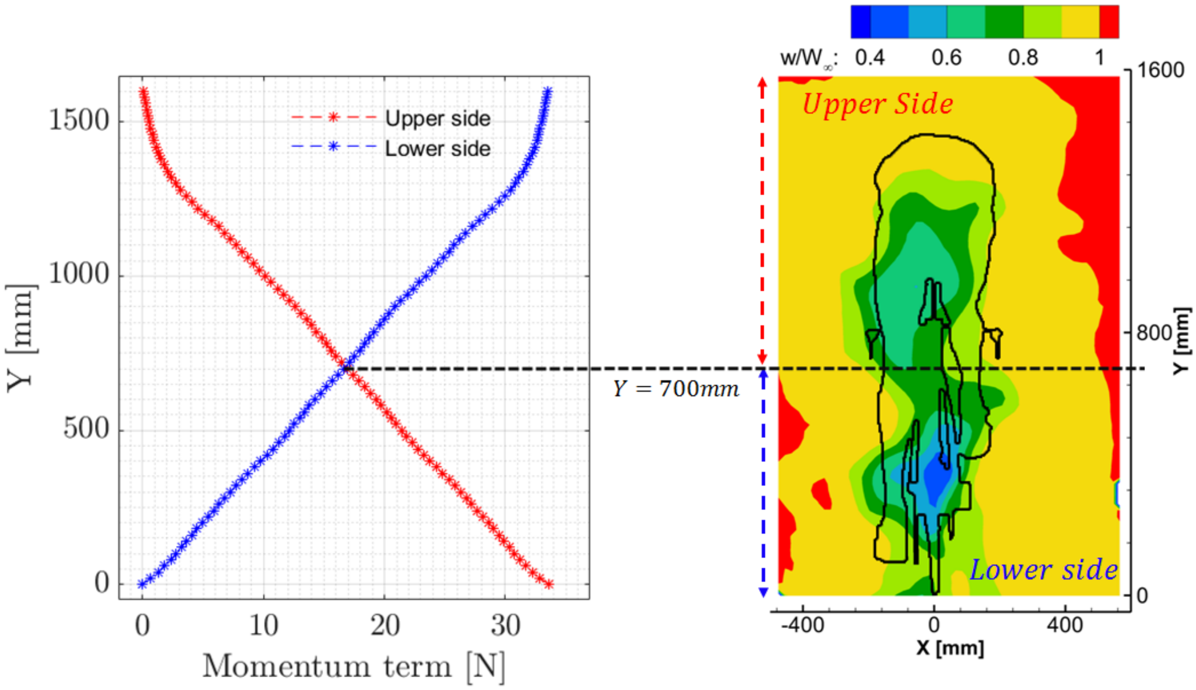

Figure 5.16: Variation of the momentum term for upper and lower sides of the distinguishing line respectively showing crossover at $Y = 700mm$. ($W_{\infty} = 13.71m/s$)

The deficits have been observed to be larger in the lower regions.This is because the rear wheel is closer to the measurement plane as compared to the hips of the cyclist. Thus, the wake from the upper side has enough space to grow and regain velocity until it reaches the measurement plane. Nevertheless, it is clear that almost 50% of the drag force comes from the lower side presenting an opportunity to investigate the reduction of drag from the bike and lower legs.

In this study it has been observed that the regions of the vortices account for almost 30% of the total drag. This was computed by summing up the momentum deficits in the regions where the Q-criterion was observed to be positive. Previously, Crouch et.al [16] reported that $20\% - 30\%$ of the drag came from the vortex regions. Therefore, this result is in fair agreement noting that their study was performed only on the upper section of the wake.

Drag reduction may be possible by dissipating these vortices by means of geometrical changes such as lowering the angle of attack of the torso. One such example may be observed by comparing the strengths of the lower back vortices ('hip vortices') observed in the study by Crouch et.al. where the torso is more upright than the one in the current study. This is in agreement with the observations made by Grappe et.al. [29].

A second possibility to reduce the drag from vortex regions is to trip the flow by strategically placing the roughness elements at the points of origination of the vortices arising from the various leg sections. Since it has been observed that the formation of these vortices follow the laminar separation mechanism, tripping the flow will delay separation and cause a turbulent separation instead of the laminar one. This would result in the lowering the strengths of these vortices and reduction in the size of the wake. Here, all the vortices have been found to arise from the inner sections of the leg. Thus, it is recommended to investigate the application of the roughness elements on the inner side.

Thirdly, the size of the low pressure separated flow region observed near the lower back (Fig. 5.7) may be reduced. Additional investigation is required for reducing the size of the recirculating regions formed under the separated flow either by making geometrical modifications to the soften the curvatures on the lower back or by using passive flow control.

5.3. Comparison of Drag from PTV and Balance Measurements

This section presents the results for the comparisons of the drag force and the drag areas obtained from the 4D-PTV measurements and the Balance measurements. Balance measurements have been recorded for all the 15 positions of the seeder. It was found that the presence of the seeder directly in front of the model caused a large reduction of the drag measured by the balance. Small variations in the drag measurements were observed at other seeder positions relative to each other. Detailed results on these variations can be found in Appendix B.

Here, the drag values from the balance measurements are presented that have been chosen in Appendix B. Two sets of balance measurements are compared for the reasons described in section 3.1.5. The biasing procedure for the measurements performed with the seeder placed upstream of the model is explained in Appendix B.

Further, two sets of results are presented from 4D-PTV - with and without the velocity corrections by Mercker and Wiedemann [49]. Errorbars indicate the variations obtained in the momentum term at 95% confidence level on the freestream velocity measured by 4D-PTV as given in Table 5.1. Errorbars in the balance measurements indicate the standard deviations observed over the range 15 seeder positions excluding the outliers observed in the centre-plane seeder positions (see Appendix B for details).

Fig. 5.17 shows the comparison the two sets of balance measurements (with and without the seeder in front) with the two sets of 4D-PTV measurements (with and without the velocity corrections $W_{\infty_{PTV}}$ and W_{∞} respectively). It is found that the 4D-PTV measurements with uncorrected velocities estimate a much lower drag as compared to the balance measurements (both with and without the seeder).

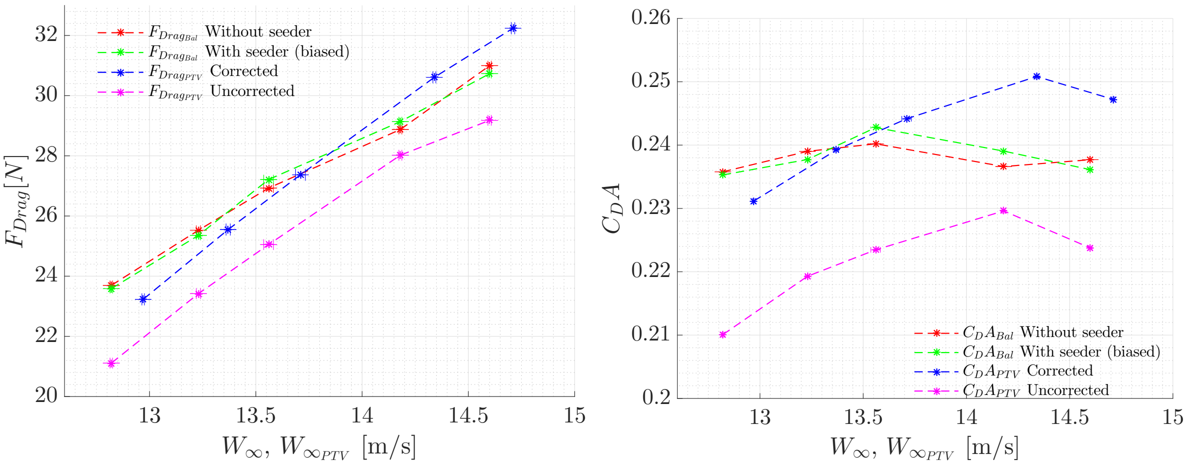

(a) (b)

Figure 5.17: (a) Comparison of the Drag force (F_{Drag}) (b) Comparison of the Drag area (C_DA) obtained from the 4D-PTV measurements and Balance measurements with increasing velocity. PTV results obtained from time-averaged flow-fields over 480 uncorrelated samples on $Z = 0$ plane. Figures show the results from PTV with and without the freestream velocity corrections.

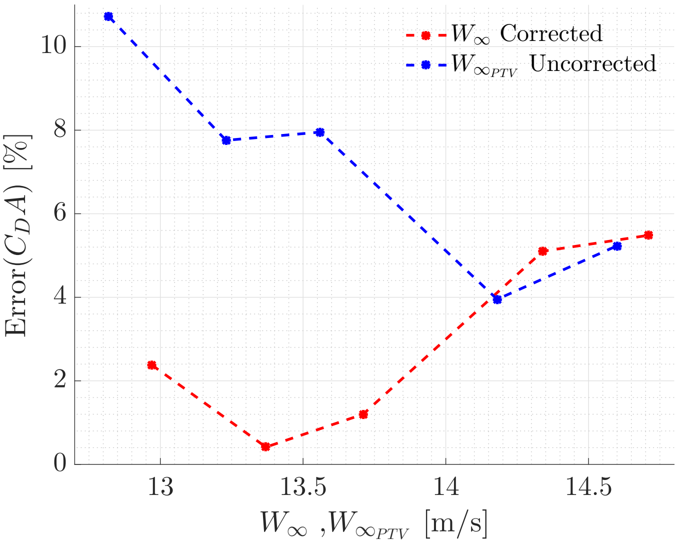

Figure 5.18: Error in the drag areas C_DA observed in the 4D-PTV measurements with respect to the Balance measurements (with seeder in front, biased)

It can be observed that the two sets of balance measurements match well since outliers from the centre-plane seeder positions are removed before averaging over all the seeder positions. This leads to a conclusion that the seeding rakes do not have as much of an effect on the drag of the model as the aerodynamic fairing that support the rakes do.

Further, as stated above, drag estimates from 4D-PTV with uncorrected freestream velocities are much lower primarily due to the lower estimation of the momentum term. This is because the freestream velocities measured at the measurement plane are lower by $2\% - 3\%$ as compared to velocities measured close to the tunnel exit. It was observed that using the velocities measured close the tunnel exit for the computation of the momentum term lead a large overestimation because of the aforementioned reason. Therefore, the velocities measured in the freestream at the 4D-PTV measurement plane are corrected using the procedure delineated in section 4.4.1. From Fig. 5.17(a), it can be observed that drag estimates after making the said corrections are closer to the ones obtained from the balance measurements.

Fig. 5.18 shows the error in the two sets of drag area estimates from 4D-PTV (with and without the corrections). Errors for the velocity corrected case has been computed by taking the differences with the values obtained at the same velocities by fitting a second order polynomial to the C_DA from the balance measurements. It is clear that the velocity corrections reduce the error in the C_DA estimates as compared to balance measurements to under 5%, under 2% for a couple of cases. Coincidentally, for these two cases, centre-plane seeding positions were not used (see Appendix B). On the other hand the estimates from uncorrected freestream velocities are as large as $8\% - 10\%$ in most cases. It is, thus, recommended to use the corrections suggested by Mercker and Wiedemann [49] for future large-scale PIV/PTV applications in open jet wind tunnels.

6

Conclusions and Recommendations

The present work in this thesis is a continuation of the effort at TU Delft towards developing the advanced Laser diagnostic techniques to a large scale. The focus of this thesis is to assess the accuracy of the 4D-PTV technique when applied on a large scale. This has been performed by comparing the drag obtained from 4D-PTV measurements by control volume method with the drag measured by an external balance. Further, it contributes towards extending the understanding of the complex flow in the wake of a cyclist at typical time-trial speeds. This complex nature of the flow has been observed by the presence of a number of vortical structures in the wake of a full scale static mannequin of a cyclist.

In order to arrive at the conclusions the author has, firstly, applied two of the advanced laser diagnostic techniques (Tomographic PIV and 4D-PTV) on the images captured in the wake of a moving sphere in a way so as to replicate the wake-scanning method which would be used on the full-scale cycling mannequin. Results (Appendix A) from this study have shown that the 4D-PTV technique is better suited for such large-scale measurements involving wake-scanning since the results from Tomographic PIV are marred by boundary effects and abrupt velocity gradients in the overlapping regions. Eventhough vortex identification is possible in such cases, inaccurate velocity gradients are likely to affect the pressure reconstruction. Such effects are eliminated by using the 4D-PTV.

A preliminary design of the 4D-PTV experiment with a convergence criteria for the flowfield used similar to the Tomographic PIV measurements suggested a sample size of 500 uncorrelated samples. It is observed that the freestream converges within 100 samples but the variations in the streamwise velocity with the number of samples are large in the vortex regions even with 500 samples. Streamwise velocities in most of the vortices converge to a unique value as the number of samples is increased beyond 1000. The same trend is also observed for the total drag force.

4D-PTV measurements performed in the wake of the cyclist model has revealed that the wake structure is similar to those observed in previous literature. Reynolds number effects were clearly seen between the present results and the results by Terra et.al. [67] in the form of reduction of the wake size. Due to higher Reynolds numbers in this case the flow over the back undergoes a delayed separation forming a smaller wake.

The vortex structures have been found in close resemblance to the study of Crouch et.al. [16], but with greater detail. Differences in observations may be attributed to the differences in the geometries considered in the two studies. This study, although on a static model, shows that the flow in the wake of the cyclist consists of more vortices than previous observations leading to the aforementioned conclusion on the complexity of the observed flow.

Based on the Reynolds numbers based on diameters of different leg sections it may be expected that the flow undergoes laminar separation over these sections. The vortices may, then, originate as a result of laminar separation mechanism over an inclined cylinder. Using this proposition, the vortices may assume specific signs on either side of each of the parts of the leg depending on their orientation with the flow direction. Based on the observed signs of the vortices and their positions, the author has proposed locations for their origination. Further, the proposed model as well as the observations are validated by results of Jux, 2017 [37]. Vortices observed in the thigh regions originate from the inner side of the thighs. Due to a lower angle of attack of the torso, the hip vortices dissipate before reaching the measurement plane but their presence is observed in the form of a downwash and some shearing motions in the hip regions. Vortices observed in the shin regions may originate from the inner side of the knee. The foot vortices are shed as a pair of counter-rotating vortices from each of the feet.

Pressure reconstruction obtained from the time-averaged three-dimensional flow-fields shows the presence of low pressure regions in the vortex cores and separated flows. Combination of the Dirichlet boundary conditions for pressure on the free boundaries and Neumann boundary conditions on the floor are found to be suitable for obtaining these results.

Streamwise component of the Reynolds stresses (Re_{zz}) shows fluctuations as large as 15% of the freestream velocity behind the stretched leg, rear wheel and some parts of the bike frame indicating formation of shear layers on these parts.

Wake structure analysed at different velocities in the range of $12.97m/s$ to $14.71m/s$ shows absence of any Reynolds Number effects as the size of the wake remains, more or less, constant. Drag forces computed from these flow-fields agree with this fact as the variation within the nominal values is observed to be less than 5% from the 4D-PTV measurements and less than 2% from the balance measurements. Drag forces obtained from the time-averaged 4D-PTV measurements, after correcting for the jet expansion and nozzle blockage [49], are within 5% of those obtained from the balance measurements. Without these corrections, the estimates from 4D-PTV are largely under-predicted.

Analysis on various components of the drag force shows that the contribution from the momentum term is close to 95%, Reynolds stress term contributes about 5% and the contribution from the pressure term is a paltry 0.3% to the absolute sum of the drag components. At the measurement location in the study, almost all the variation in the drag force comes from the momentum term. It is, therefore, recommended to neglect the pressure term in future studies focusing on drag differences if measured at a sufficient distance downstream from the model as in this study. In this regard, the Ring of Fire concept [64] is well-suited to obtain the drag forces as well as flow-fields for different positions of the cyclists in the dynamic condition. Measurements from Ring of Fire may not be required to be corrected for jet expansion, unlike the measurements performed in the current study. Open jet wind tunnel corrections are recommended for large-scale PIV/PTV measurements performed in the Open Jet Facility requiring the use of control volume approach for drag determination.

There is a close match between the mean of the time averaged drag areas over 480 samples obtained at different velocities in the range of $12.97m/s$ to $14.71m/s$ with that obtained over 1560 samples at $13.94m/s$. Within the small range of Reynolds numbers that are considered in the first case, variations in the drag areas are not expected. Therefore, the variations that are observed in the drag areas may be attributed to the measurement uncertainty of large-scale 4D-PTV, non-convergence of the flow-field results and uncertainties in the parameters for freestream corrections.

Force measurements through an external balance for all the positions of the seeding system shows that the centre-plane seeding position with a fully exposed aerodynamic support of the seeder caused a reduction in the measurement by approximately 8% ($2N$ to $2.5N$). This reduction of the force was halved when the distance between the seeder and the model was more than tripled (see Appendix B). When the seeder is positioned in the freestream the influence is not as large, but not negligible.

The vortex regions make up approximately 30% of the total drag from the current study. Thus, it is recommended to investigate the possibility of drag reduction by means of flow control applied on the regions in the inner sections of the leg from where these vortices have been observed to originate. Further, investigations on delaying separation over lower back and effects of geometrical modifications are recommended for drag minimization. It is also recommended to conduct these investigations using the 4D-PTV technique and compare the drag results with the balance measurements as done in the current study in order to assess the accuracy of the technique with geometrical changes.

Apart from assessing accuracy of the large-scale 4D-PTV technique with different flow and geometrical parameters, it is recommended to improve the design of the aerodynamic support structure as well as positioning of the seeding system upstream of the model such that its influence is minimized. The settling chamber of the wind-tunnel may be a suitable location in order to achieve this.

The main advantage of 4D-PTV is that Lagrangian particle track (LPT) information available throughout the measurement domain apart from its higher positional accuracy as compared to Tomographic PIV. However, Lagrangian information is lost once the it is converted to a Cartesian framework. This results in averaged velocity vectors over a number of particles available in the individual bins. It is recommended to investigate the possibility of utilizing the Lagrangian particle information in the same form and evaluate the pressure fields and drag forces. Although, it has been observed that the pressure term contributes negligibly to the total drag force, the pressure fields have the potential to reveal valuable information about the flow features. Recent paper by van Gent et.al. [72] shows that highly accurate pressure fields can be obtained from the LPT. Further such investigations are recommended in the case of large-scale 4D-PTV.

A

Ring of Fire with sphere

A separate experiment using the Ring of Fire concept [64] was carried out with a sphere moving through an illuminated volume. Time resolved acquisitions were performed in order to enable both Tomographic PIV as well as 4D-PTV analyses. Further, the acquired images were divided into four parts and each of them was analysed individually using Tomographic PIV and later combined. This is done so as to replicate the large scale acquisitions on the cycling mannequin which necessitates wake scanning due to the limitation of the size of the seeding system. All the analysis presented in this Appendix are performed at 2 diameters in the wake of the sphere. The measurement setup and results from both the analyses are given in the following sections.

A.1. Experimental Setup

A brief description of the setup is given in this section. A sphere of $10cm$ diameter mounted on a cylindrical rod $20cm$ long and $3mm$ in diameter. The rod is covered with an aerodynamic fairing on the trailing side. The sphere assembly is mounted on a carriage which can move over rails. The speed of the carriage is controlled with the help of a string which is pulled by an electric motor. The schematic of this setup is shown in Fig. A.1.

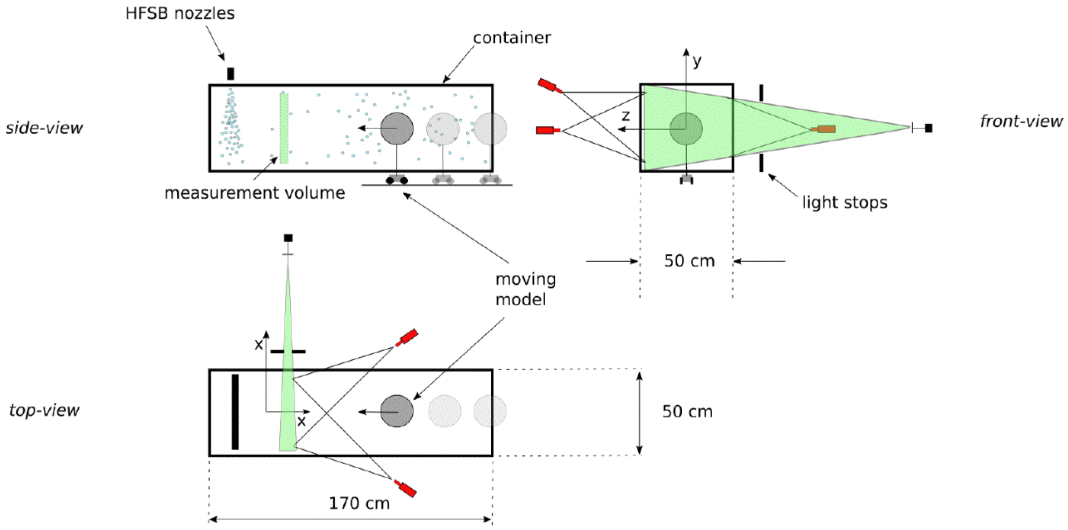

Figure A.1: Schematic of the Ring of Fire setup for moving sphere. Reproduced from Terra et.al. [69].

The speed of the moving sphere is also accurately measured with the help of a high speed camera recording at 1kHz (Cam 4, Fig. A.2). Two markers are placed at the entrance and the exit of the tunnel at a known distance and the time taken by the sphere to move in this distance is obtained from the recordings.

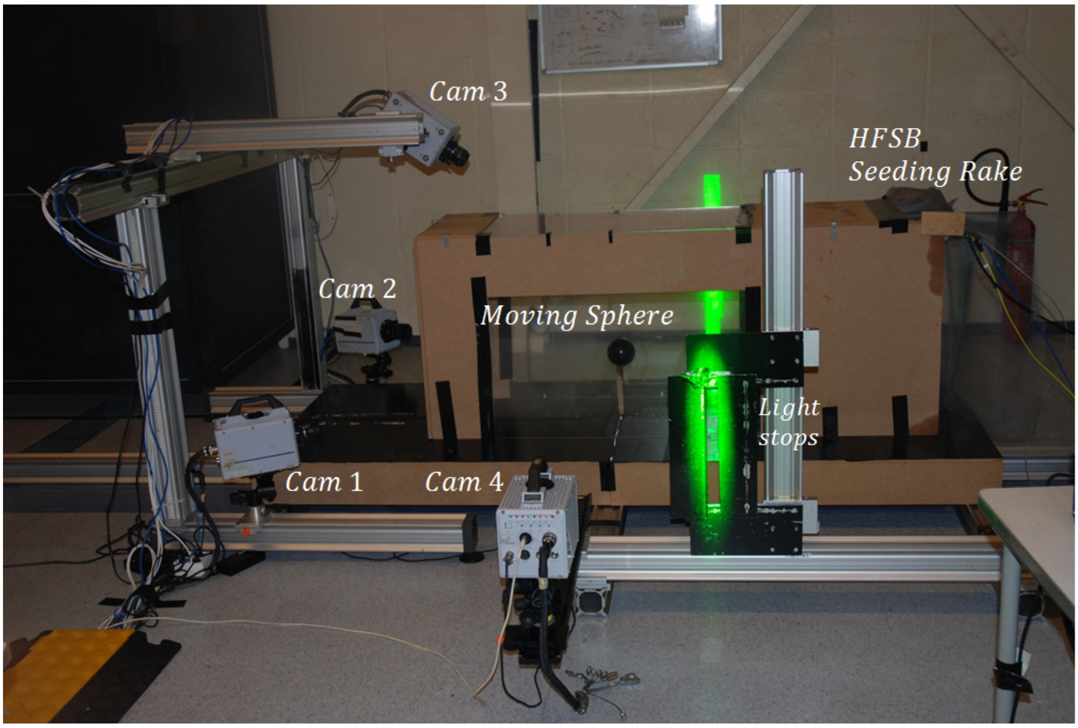

Figure A.2: Experimental setup for the Ring of Fire measurements with a moving sphere.

Time resolved acquisitions at $500Hz$ are performed on a measurement region having a square cross-section of $50cm \times 50cm$. For this purpose, three high speed cameras (Photron Fast CAM SA1) (Cam 1 to Cam 3 , Fig. A.2) are used. The objectives used for these three cameras are $35mm$, $50mm$ and $60mm$ respectively. The magnification obtained is approximately 0.04. The tunnel is seeded with Helium-Filled Soap Bubbles (HFSB) with a single seeding rake consisting of 10 nozzles. The measurement volume is illuminated with a Laser. Specifications of all the instruments used in this experiment can also be found in Chapter 3.

A.2. Data reduction

For the demonstration of the accuracy of Tomographic PIV and 4D-PTV, the data at 2 diameters in the wake of the sphere has been considered. The acquired images are pre-processed by subtracting the averaged image over 300 frames from all the individual frames to eliminate the background noise. The subtracted images are Gaussian smoothed with a kernel of 3×3 voxels and sharpened. Geometrical calibration and the self-calibration procedures [78] are performed that result in a maximum disparity below $0.1px$ for each camera. Digital image resolution of 2.15 pixels/mm is obtained. Thereafter, Tomographic PIV and 4D-PTV algorithms are employed separately as discussed below.

A.2.1. Tomographic PIV

The pre-processed images are analysed with Tomographic PIV in two ways:

1. Full volume reconstruction and correlation:
   Volume reconstructions are performed with FastMART algorithm in a thin volume present at 2 sphere diameters after the sphere has passed the measurement volume. A set of 3 frames is used for reconstruction. A volume of $460mm \times 460mm \times 40mm$ is reconstructed in the X, Y and Z directions respectively with the MLOS initialization method followed by 6 SMART iterations as suggested by Atkinson and Soria [4]. Subsequently, volume

correlation is performed with an interrogation window size of 96 voxels in all three directions and an overlap of 75%. The peak search radius is gradually reduced from 12 voxels to 1 voxel in 4 iterations.

2. Partial volume reconstruction, correlation and recombination:
   In measurements on a scale as large as a human scale, such as the cycling mannequin, it was not possible to achieve seeding in the entire measurement volume simultaneously owing to the limitation of the size of the seeding system. Therefore, the measurements are required to be performed with a wake scanning method as shown in Fig. 4.4(a). This wake scanning imposes several challenges during post-processing such as stitching of the gridded velocity fields at different positions together while ensuring smooth gradients on the boundaries. Due to the slightly different conditions while performing measurements at the different positions of the domain, ensuring such a smoothness in the gradients of velocity fields is difficult. Moreover, the velocity fields from different positions overlap and cause these gradients to become more uneven. Abrupt changes in the velocities in the overlapping regions are very well observed in the vorticity fields. In order to visualize this, the acquired full volume images are masked into four sections as shown in Fig. A.3.

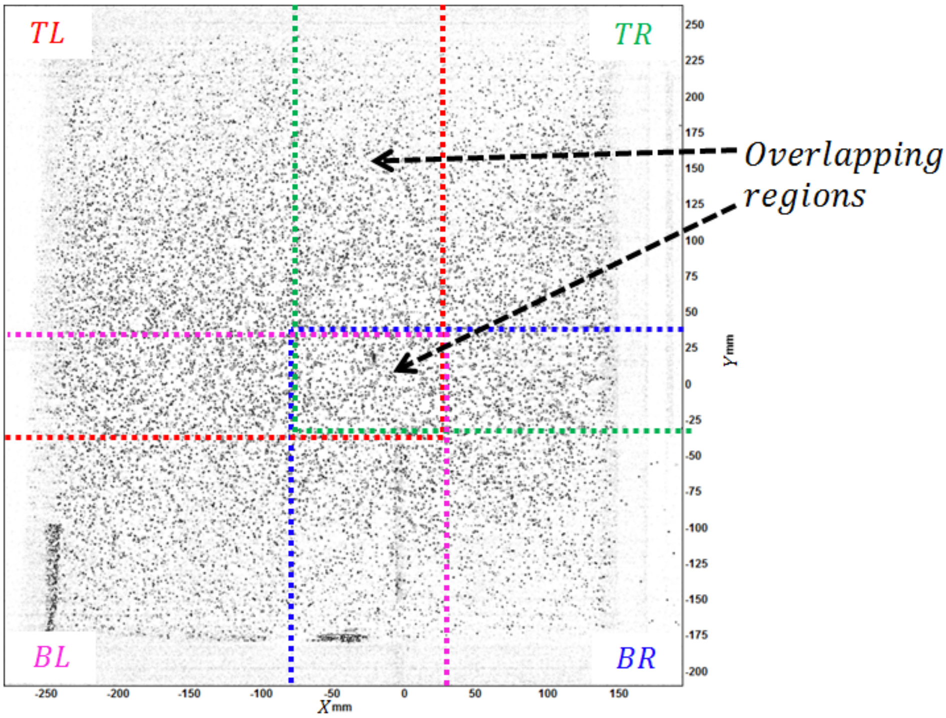

Figure A.3: Four divisions created on the full domain images. Boundaries can be identified using the color coding. TL: Top Left (Red), TR: Top Right (Green), BL: Bottom Left (Pink), BR: Bottom Right (Blue)

These masked domains (TL, TR, BL and BR) are separately processed with the FastMART algorithm using the MLOS-SMART method described above. Vector fields obtained from the volume correlation at the different positions are averaged to obtain a single grid in the entire measurement volume.

A.2.2. 4D-PTV

4D-PTV analysis with Shake-The-Box [61] algorithm is performed on a set of 15 time-resolved images equally spaced before and after the instance of 2 sphere diameters in the wake. For this, an Optical Transfer Function [60] is computed in the entire domain from a set of 275 images and employed within the algorithm to process the pre-processed images. The resulting particle tracks are binned to obtain a velocity field on a Cartesian grid. The bin size used here is 52 × 52 × 52 voxels with an overlap of 75%.

A.3. Results

Results from the Tomographic PIV and 4D-PTV analyses described in the above section are presented here. Our aim is to replicate the large-scale wake scanning technique on the acquired full domain data and observe the differences that arise in the processing.

Fig. A.4 shows the results obtained from a single measurement at 2 diameters in the wake of the sphere processed with the aforementioned Tomographic PIV techniques. It is clearly observed that partial volume reconstruction and recombination technique yields a slightly different result in terms of the velocity fields.

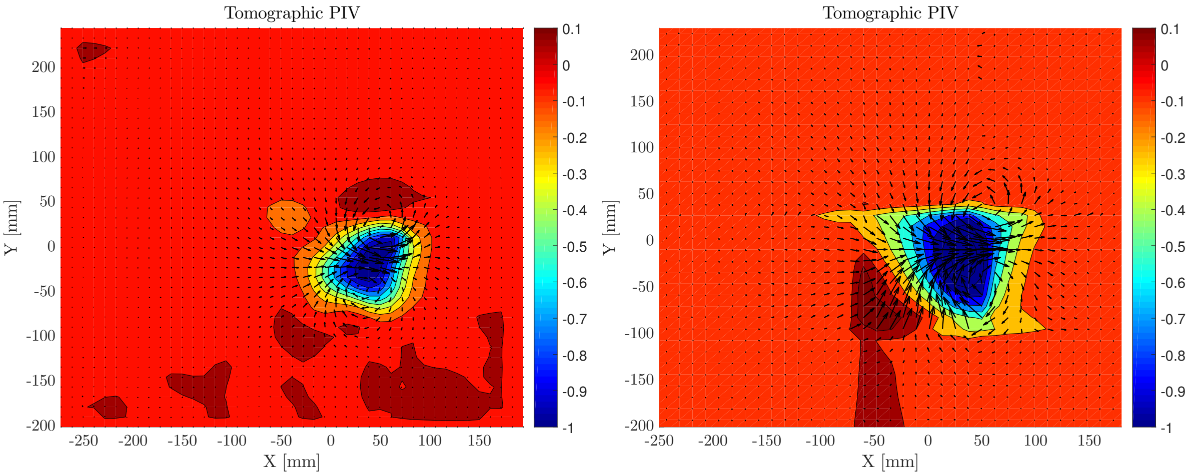

(a) (b)

Figure A.4: Velocity vector fields obtained from Tomographic PIV at 2 diameters in the wake of a moving sphere (a) Full volume reconstruction and correlation (b) Partial volume reconstruction, correlation and recombination. Result obtained from one measurement.

Firstly, the wake of the sphere is well captured in both cases, however there is a difference in the shape of the wake. Here, the wake structure obtained from the full volume reconstruction (Fig. A.4(a)) appears to be more realistic as the velocities are continuous and smooth. Fig. A.4(b) shows that the streamwise velocities do not go the freestream velocities smoothly. This artifact in the velocity fields may be attributed to the boundary effects in the overlapping regions. The boundary effects are clearly seen in the vorticity fields (see Fig. A.5).

Fig. A.5 shows the presence of the counter-rotating vortex pair in the wake of the sphere (vortices A and B). The vorticity field in the freestream is expected to be clean as observed in Fig. A.5(a). In contrast to this, Fig. A.5(b) shows the presence of vorticity along the boundaries of the partial domains (as marked in the figure). These vortices are unphysical and may be attributed to the abrupt velocity gradients occurring at the boundaries from the velocity fields computed at different positions.

Presence of such unphysical vorticity hinders the possibility of detecting the true vortices from vorticity fields. In such cases, the Q-criterion is useful to identify only those vortices which are physical. Fig. A.6 shows the comparison of the Q-criterion obtained in both the cases. The figure shows that the unphysical vorticity observed in Fig. A.5(b) does not appear in the Q-criterion. Thus, vortex identification may still be possible with this method. However, the locations and strengths of the vortices are affected due to the overlapping of fields from different positions.

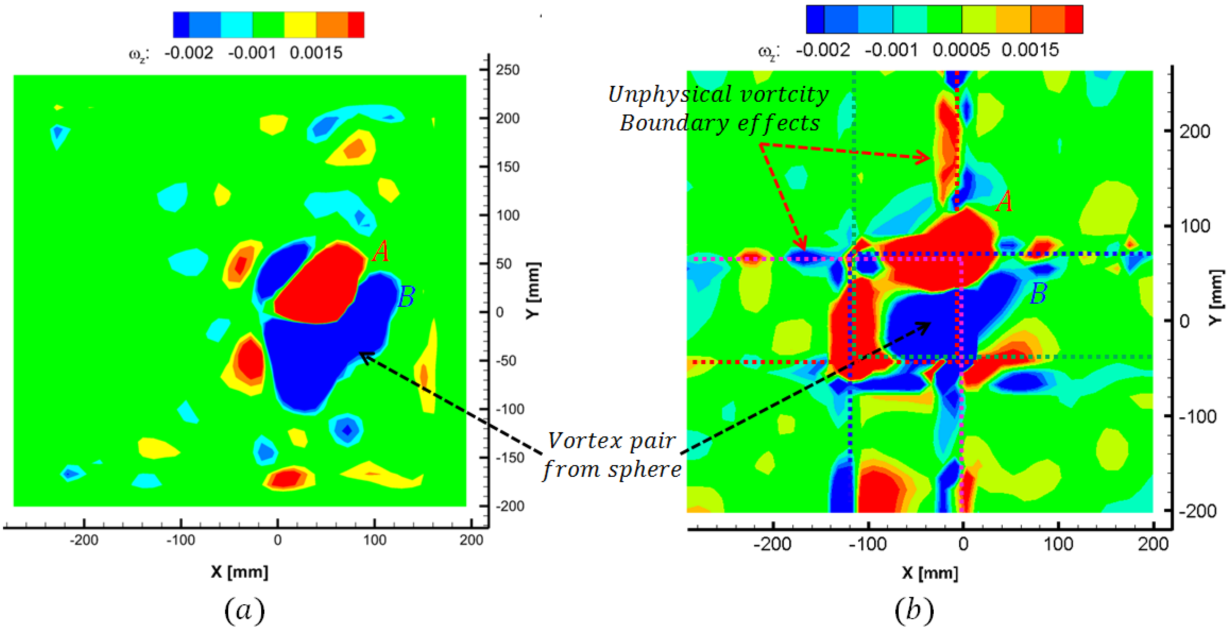

Figure A.5: Streamwise vorticity field obtained from (a) Full volume reconstruction and correlation (b) Partial volume reconstruction, correlation and recombination. Result obtained from one measurement.

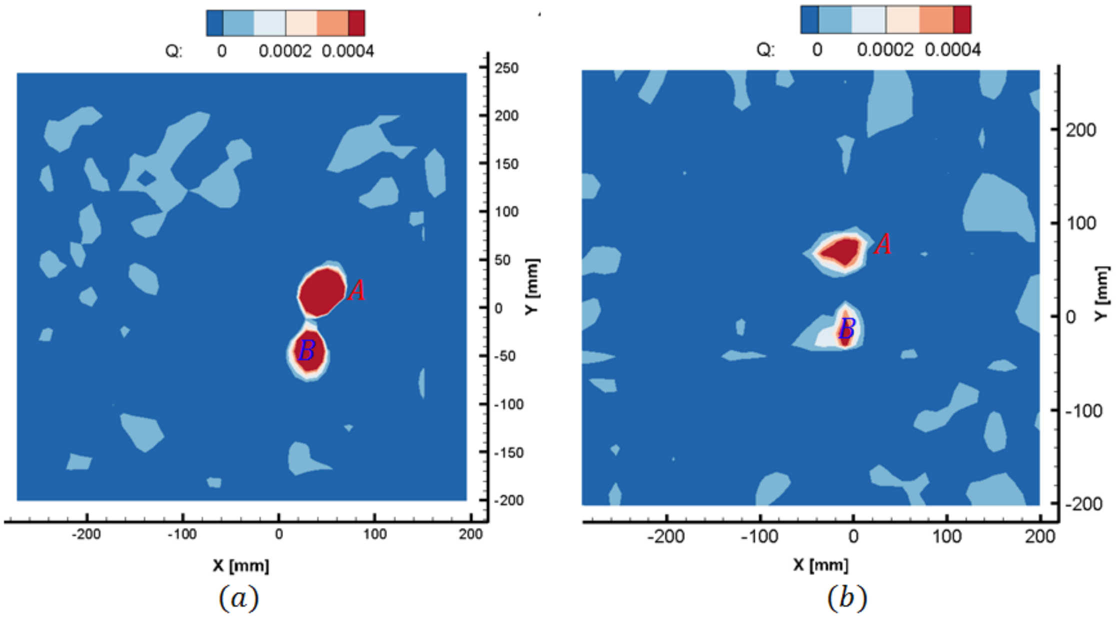

Figure A.6: Q-criterion computed from (a) Full volume reconstruction and correlation (b) Partial volume reconstruction, correlation and recombination. Result obtained from one measurement.

Further, pressure reconstruction is extremely sensitive to accurate velocity gradients in all the directions (see Eq. 2.14). Presence of abrupt velocity gradients at the boundaries may hamper reliable pressure reconstruction. This restricts the use of the partial reconstruction method by means of Tomographic PIV.

Here, the 4D-PTV technique is useful as shown by Fig. A.7. The velocity field obtained from STB are a close match to those obtained from the Tomographic PIV. It must be noted that this result is obtained from a single measurement which yields approximately 1800 tracks in the entire volume. The vector fields appear to be continuous and smooth, unlike

Fig. A.4(b).

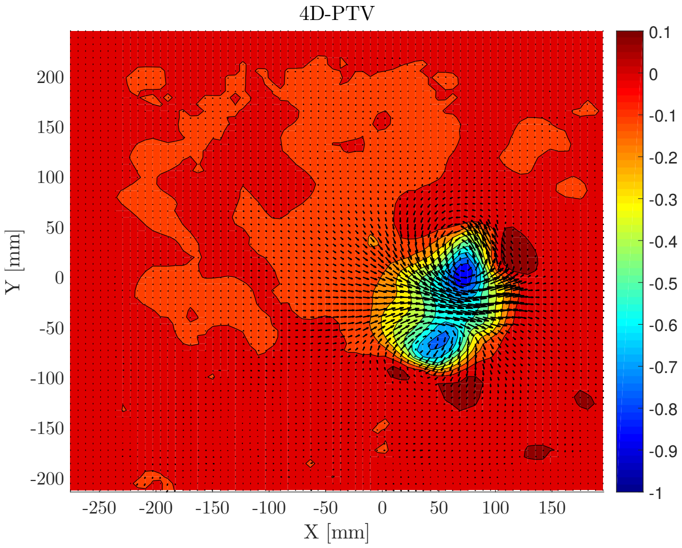

Figure A.7: Velocity vector field obtained from 4D-PTV (STB) applied to 15 images around the instance of 2 diameters in the wake of the moving sphere.

This can be further visualized in the vorticity fields as shown in Fig. A.8(a). Unlike the partial tomographic reconstruction methods (Fig. A.5(b)), the vorticity fields obtained from STB are free of the boundary effects. Even if a similar approach of partial reconstruction is applied using STB, this technique offers the possibility of first recombining the tracks in the entire volume and subsequently proceed with the binning procedure to obtain velocity fields on a Cartesian grid. Thus, the boundary effects are eliminated by using this technique.

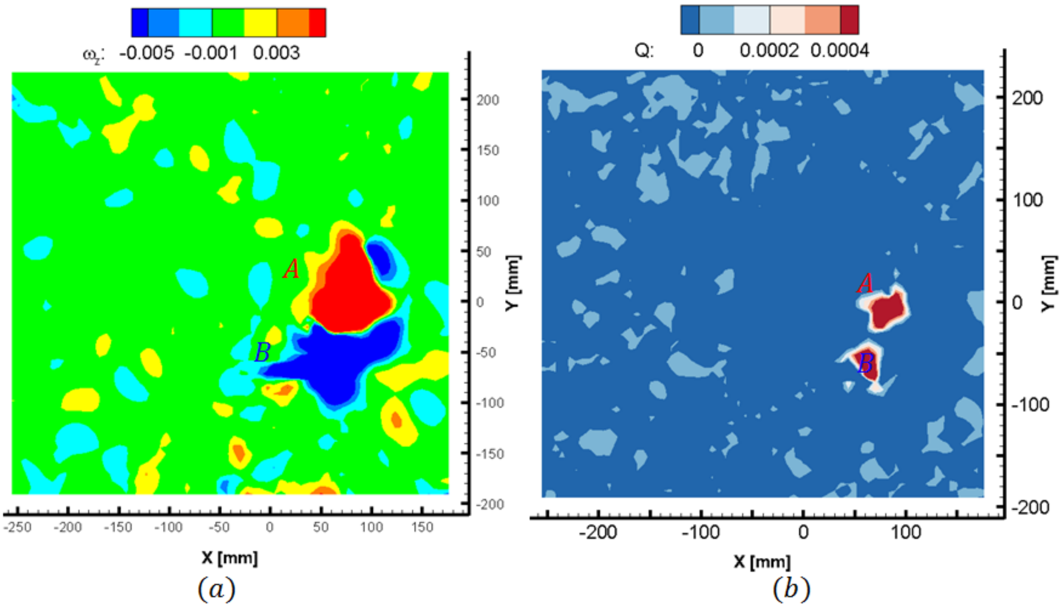

(a) (b)

Figure A.8: (a) Streamwise vorticity obtained from STB (b) Q-criterion for detection applied on the results from STB

Vortex structures (vortices *A* and *B*) are, again, identified using the Q-criterion (Fig. A.8(b))and are a close match with the structures obtained from full domain Tomographic PIV results (Fig. A.6(a)).

A.4. Conclusions

This study with a moving sphere through the Ring of Fire [64] shows that 4D-PTV offers more accurate results as compared to the Tomographic PIV in cases of large-scale measurements involving the wake scanning approach. Unphysical vorticity and abrupt velocity gradients have been observed in the results obtained from Tomographic PIV. These artifacts are likely to occur from the boundary effects arising from the velocity fields obtained on the either side of the boundary. Furthermore, overlap in the velocity fields at different positions seem to affect the vortex strengths and locations as observed by the Q-criterion.

On the other hand, 4D-PTV with STB offers results that are equivalent to those obtained from the Tomographic PIV. Being a Lagrangian particle tracking technique, STB offers the possibility of combining the particle tracks from different positions in the volume and later convert them on to a Cartesian grid using binning procedures. With this method the possibility of producing artifacts such as the boundary effects is eliminated. Furthermore, smooth velocity gradients are obtained which are crucial for obtaining reliable pressure fields. Since we are interested in only the time-averaged results, the velocity fields will improve upon addition of more samples.

These results provide sufficient motivation to use the 4D-PTV technique instead of the Tomographic PIV in the case of the large-scale wake measurements involving wake-scanning.

B

Balance measurements

This appendix presents the balance measurements performed during the two experimental campaigns for different positions of the seeder as shown in Fig. B.1. It has been observed that the presence of the seeding system as a large influence on the balance measurements. Variations have been observed for different positions. Positions $Pos07$ and $Pos08$ (see Fig. B.1) in particular were found to have the maximum reduction in the drag. Further, this appendix shows the values that are considered for the comparison with 4D-PTV results.

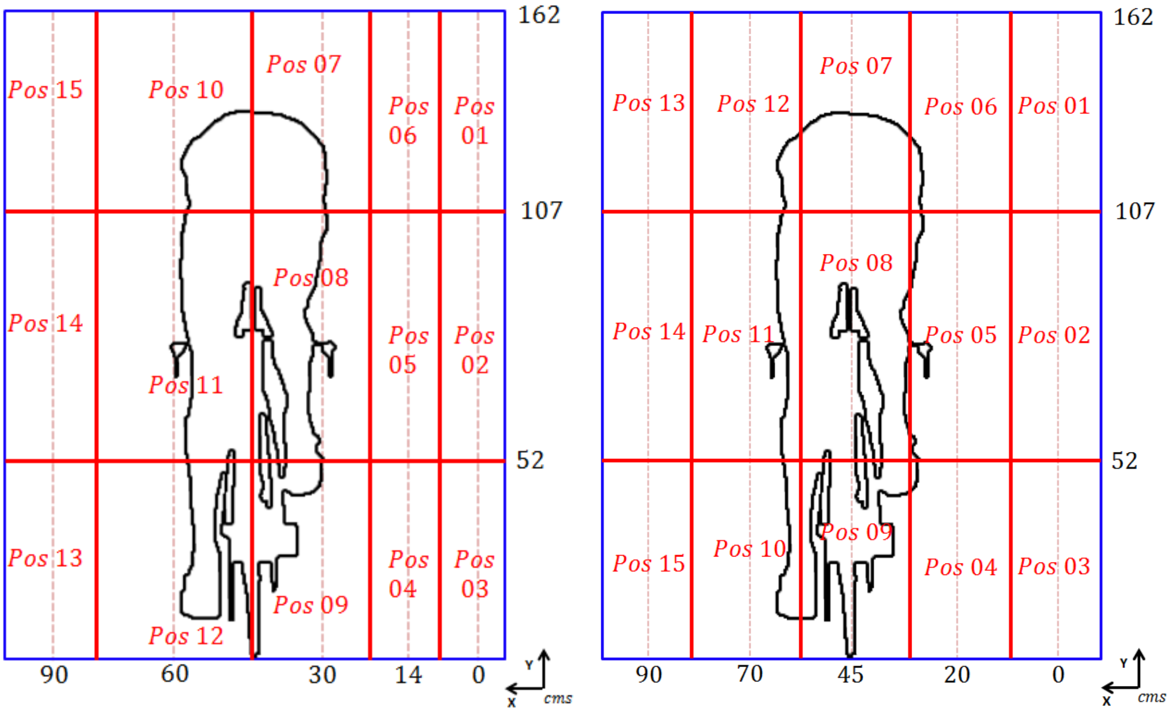

(a)

(b)

Figure B.1: Seeder positions in X and Y for 4D-PTV measurements at (a) $W_{\infty_{OJF}} = 13.48m/s$ *and* $13.99m/s$ *(b)* $W_{\infty_{OJF}} = 12.97m/s$, $14.50m/s$, $15.03m/s$. *Schematic for Experimental Campaign 1 only.*

Fig. B.2 shows the drag measurements over all the seeder positions obtained from the balance during the first experimental campaign. Variations as large as $2N$ are easily noticeable. Furthermore, it is observed that the presence of the seeder on the centre-plane positions ($X = 45cm$), $Pos07$ and $Pos08$ in particular has the maximum influence. This may be attributed to the wake of the aerodynamic support for the seeder.

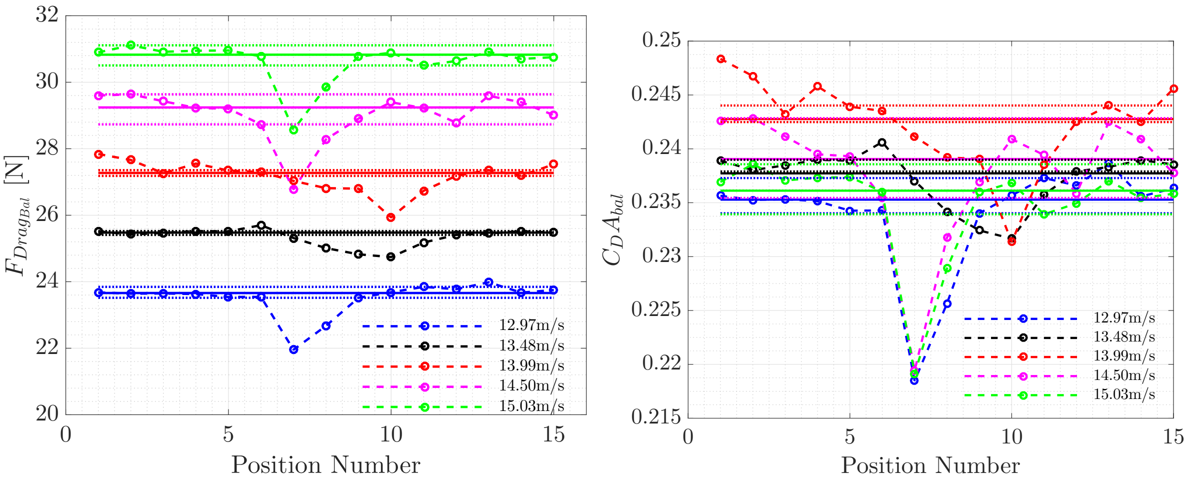

(a) (b)

Figure B.2: Drag force measurements recorded by an external balance ($F_{Drag_{bal}}$). (a) Drag force variation (b) Drag area variation with the position of the seeder. Values outside the dashed lines are considered to be outliers. Solid lines represent the mean values.

Owing to the large variations, choice of a value for the drag measurement from the balance is a challenge. Since the influence of the seeding rakes are inherently present in the results from 4D-PTV measurements, it is important to choose a value that includes the effects from seeding rake but excludes the effects from the aerodynamic support. This is obtained by computing a mean of the recorded values after excluding the outliers. Most of the outliers are present at higher seeding positions where a larger section of the aerodynamic support stands exposed. They are eliminated in multiple iterations using 2 standard deviations limits. The mean values from this procedure have been marked on Fig. B.2 with solid lines, whereas the dashed lines indicate the controls for the outliers.

Note that the centre-plane seeder positions were not used for $W_{\infty_{OJF}} = 13.48m/s$ and $13.99m/s$ (see Fig. B.1(a)). This can explain the shift in the drag variations observed in the case of these two flow speeds. Here, again, $Pos10$ accounts for the maximum reduction in the measured drag since the seeder is at the top and in front of the stretched leg.

For the second experimental campaign couple of acquisitions were performed at seeder positions $Pos04$ to $Pos12$ and single acquisition was made for $Pos01$ - $Pos03$ and $Pos13$ - $Pos15$. The seeder positions used in this experiment were similar to those shown in Fig. B.1(b) except for the change for $Run25$ (Fig. B.3). This additional Run was performed to fill up the gap observed in the marked region.

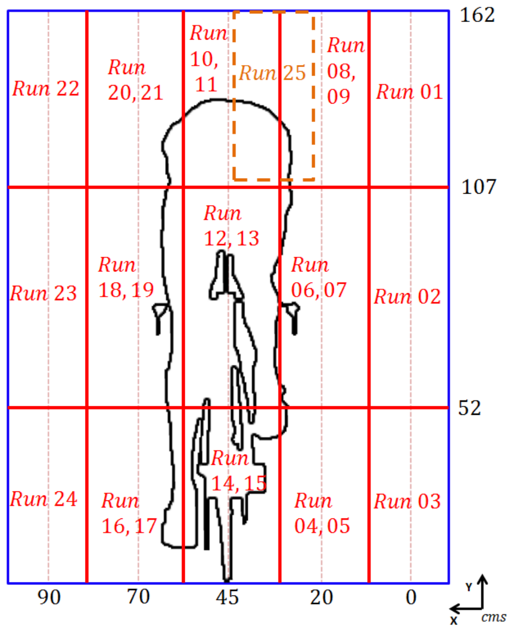

Figure B.3: Run numbers for different seeder positions in X and Y for 4D-PTV measurements during the second experimental campaign at (a) $W_{\infty_{OJF}} = 13.98m/s$

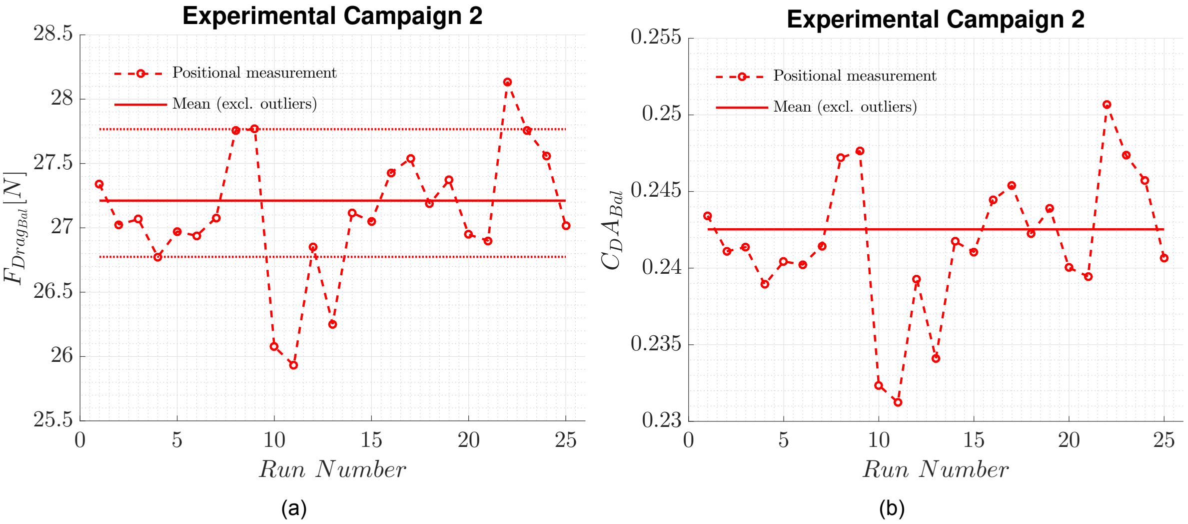

Figure B.4: Drag force measurements for the second experimental campaign (a) Drag force variation (b) Drag area variation with the position of the seeder. Values outside the dashed lines are considered to be outliers. Solid lines represent the mean values.

Similar to the results from first campaign large variations are observed in the measurements made during the second campaign as well. Further, the trend is similar, in the sense that the higher seeder positions closer to the centre-plane influence the measurements by more than $1N$. Again, a mean of the values is taken after eliminating the outliers (controls indicated by dashed lines). Drag area computed from this mean value is marked in Fig. B.4(b) using a solid line. This mean drag area (0.2425 ± 0.0045) matches closely with that obtained from the first campaign for this velocity (see Table 5.1).

Drag forces obtained from Eq.1.1 for the tested velocities assuming a constant drag area equal to 0.2425 are plotted in Fig. B.5. It shows that the balance measurements with and without the presence of the seeding system are lower than these analytical results by a maximum of $0.75N$.

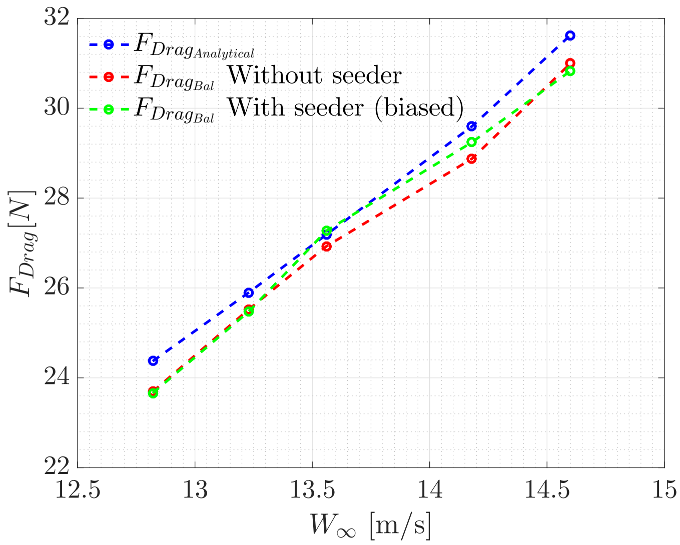

Figure B.5: Comparison of results from balance measurements with analytical results

C

Statistical Convergence

This appendix presents the statistical convergence of the flow field and the drag results. According to the statistical uncertainty formulation, the uncertainty in an averaged measurement decreases with an increase in the number of uncorrelated samples. Here, the averaging is done over a number of uncorrelated samples acquired in time. Results presented in Chapter 5 are time-averaged over 480 such samples. Here, flow-field and drag convergence is shown for a total of 1560 uncorrelated samples by means of damping in the fluctuations observed in the the mean streamwise velocity and drag components.

C.1. Statistical convergence of flow-field

Fig. C.1 shows the variations observed in the standard deviations (σ_w) in the streamwise velocities for different number of samples (N).

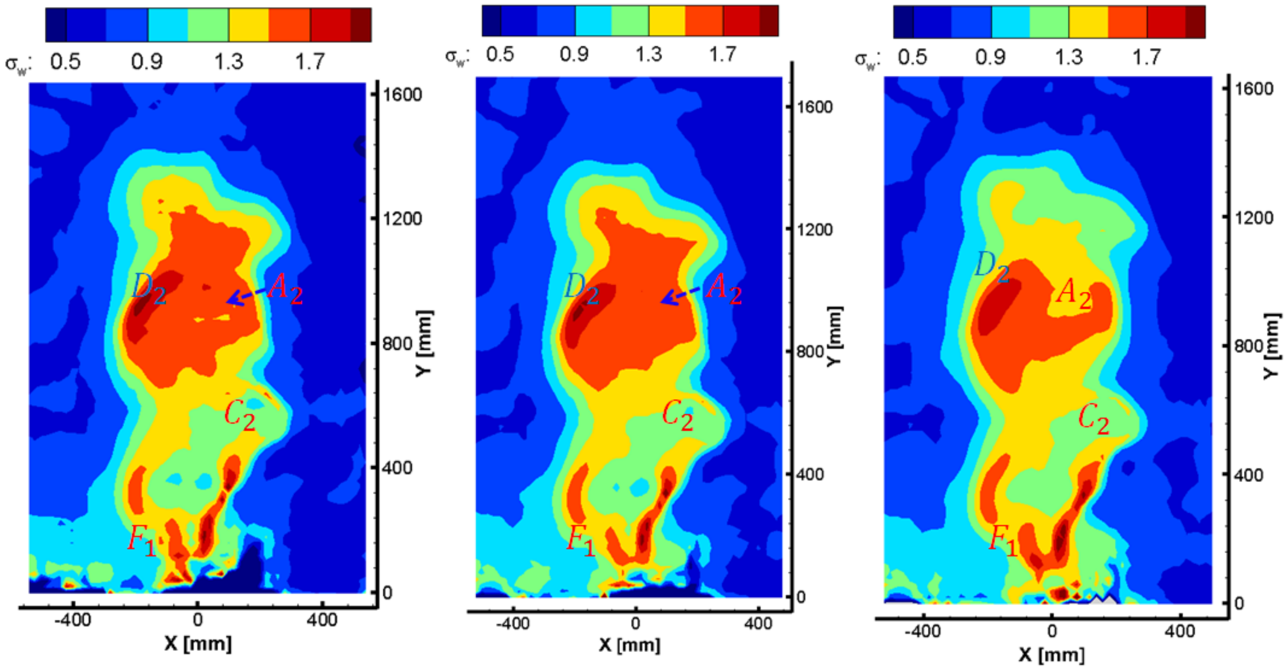

$(a)\ N = 400$ $(b) N = 780$ $(c) N = 1560$

Figure C.1: Standard deviations in the streamwise velocity (σ_w in m/s) computed over particles present in each bin for increasing number of samples N.

Some of the stronger vortices are marked for reference (see Fig. 5.5 for labels). The convergence of the flow-field may be seen in the decreasing values of σ_w in the wake and particularly in the regions of these vortices.

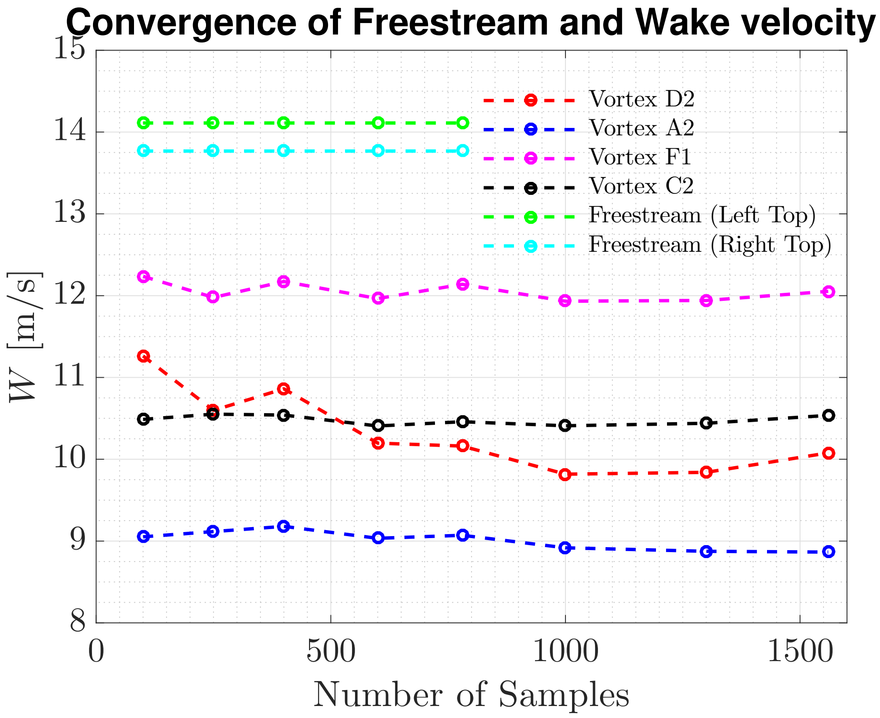

Figure C.2: Time-averaged streamwise velocities plotted in the regions of marked vortices and the freestream for increasing number of samples.

Fig. C.2 shows that the streamwise velocities in the freestream are converged very quickly. However, variations may be observed in the velocities in the regions of the marked vortices. These velocities in these vortex regions achieve a steady state value when N is approximately greater than 1000. The variation in the streamwise velocities beyond this value is less than 2% of the freestream velocity.

C.2. Statistical convergence of drag components

Fig. C.3 shows the variation in the drag components obtained from the time-averaged flow fields with increasing number of samples. Here, the pressure term $F_{Drag_{Pr}}$ is not plotted as it's magnitude is negligible as compared to the variations observed in the other components (Table 5.1). Increasing the number of samples has little effect on the Reynolds stress contributions. Most of the variations stem from the momentum term. It is observed that for lower number of samples the variations in the drag forces are as large as 5% with respect to the value obtained for 1560 samples. Again, variations reduce to less than 2% as the number of samples increase beyond 1000 samples.

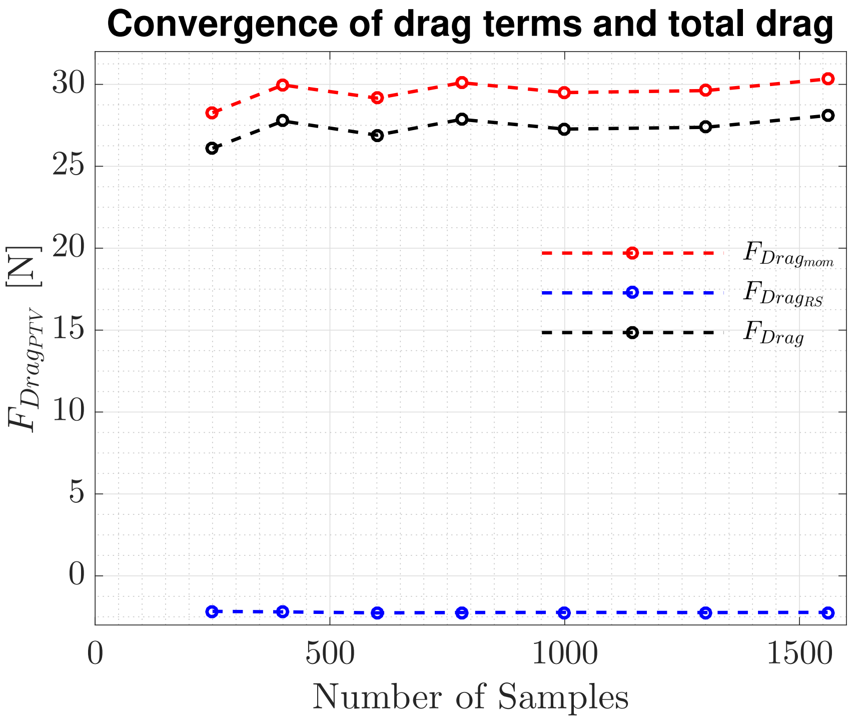

Figure C.3: Variation of the drag components and total drag with increasing number of samples.

The similarity in the trends observed for the variations of the velocities in the vortex regions and the drag forces, particularly the momentum term, for different number of samples provides evidence for the fact found by Crouch et.al. [16] that the observed large-scale vortex structures account for all the variation observed in the drag.

Bibliography

[1] Ronald J Adrian. Particle-imaging techniques for experimental fluid mechanics. *Annual review of fluid mechanics*, 23(1):261–304, 1991.

[2] H.J. Alons. *OJF External Balance*. Nationaal Lucht en Ruimtevaartlaboritorium (National Aerospace Laboratory NLR), 2008.

[3] John David Anderson Jr. *Fundamentals of aerodynamics*. Tata McGraw-Hill Education, 2010.

[4] Callum Atkinson and Julio Soria. An efficient simultaneous reconstruction technique for tomographic particle image velocimetry. *Experiments in Fluids*, 47(4-5):553, 2009.

[5] David R Bassett Jr, Chester R Kyle, Louis Passfield, Jeffrey P Broker, and Edmund R Burke. Comparing cycling world hour records, 1967-1996: modeling with empirical data. *Medicine and Science in Sports and Exercise*, 31(11):1665–1676, 1999.

[6] Johannes Bosbach, Matthias Kühn, and Claus Wagner. Large scale particle image velocimetry with helium filled soap bubbles. *Experiments in fluids*, 46(3):539–547, 2009.

[7] Len Brownlie, Peter Ostafichuk, Erik Tews, Hil Muller, Eamon Briggs, and Kevin Franks. The wind-averaged aerodynamic drag of competitive time trial cycling helmets. *Procedia Engineering*, 2(2):2419–2424, 2010.

[8] LW Brownlie, I Gartshore, A Chapman, and EW Banister. The aerodynamics of cycling apparel. *Cycling science*, 3(3-4):44–50, 1991.

[9] GW Brune. Quantitative three-dimensional low-speed wake surveys. 1992.

[10] Ed Burke. *High-tech cycling*. Human Kinetics, 2003.

[11] Giuseppe Carlo Alp Caridi, Daniele Ragni, Andrea Sciacchitano, and Fulvio Scarano. A seeding system for large-scale tomographic piv in aerodynamics. In *11th international symposium on particle image velocimetry, Santa Barbara, USA*, pages 14–16, 2015.

[12] Yunus A Cengel, Robert H Turner, John M Cimbala, and Mehmet Kanoglu. *Fundamentals of thermal-fluid sciences*. McGraw-Hill New York, NY, 2005.

[13] Kevin Cooper. Bluff-body blockage corrections in closed-and open-test-section wind tunnels. *Wind Tunnel Wall Correction (AGARD-AG-336), BFR Ewald, ed., Advisory Group for Aerospace Research and Development, North Atlantic Treaty Organization, Neuilly-sur-Seine Cedex, France*, 1998.

[14] Timothy Crouch, Mark Thompson, David Burton, John Sheridan, and Nicholas Brown. Dominant flow structures in the wake of a cyclist. In *30th AIAA Applied Aerodynamics Conference*, page 3212, 2012.

[15] Timothy N Crouch, David Burton, Mark C Thompson, Nicholas AT Brown, and John Sheridan. Dynamic leg-motion and its effect on the aerodynamic performance of cyclists. *Journal of Fluids and Structures*, 65:121–137, 2016.

[16] TN Crouch, D Burton, NAT Brown, MC Thompson, and J Sheridan. Flow topology in the wake of a cyclist and its effect on aerodynamic drag. *Journal of Fluid Mechanics*, 748: 5–35, 2014.

[17] TN Crouch, D Burton, JA Venning, MC Thompson, NAT Brown, and J Sheridan. A comparison of the wake structures of scale and full-scale pedalling cycling models. *Procedia Engineering*, 147:13–19, 2016.

[18] C TM Davies. Effect of air resistance on the metabolic cost and performance of cycling. *European journal of applied physiology and occupational physiology*, 45(2):245–254, 1980.

[19] R de Kat, BW van Oudheusden, and F Scarano. Instantaneous pressure field determination in a 3d flow using time resolved thin volume tomographic-piv. In *Proceedings of the 8th international symposium on particle image velocimetry—PIV09, Melbourne, Australia*, 2009.

[20] PE Di Prampero, G Cortili, P Mognoni, and F Saibene. Equation of motion of a cyclist. *Journal of Applied Physiology*, 47(1):201–206, 1979.

[21] Stefano Discetti, Andrea Natale, and Tommaso Astarita. Spatial filtering improved tomographic piv. *Experiments in fluids*, 54(4):1505, 2013.

[22] Gerrit E Elsinga, Fulvio Scarano, Bernhard Wieneke, and Bas W van Oudheusden. Tomographic particle image velocimetry. *Experiments in fluids*, 41(6):933–947, 2006.

[23] Richard GJ Flay. Bluff body aerodynamics. In *Advanced Structural Wind Engineering*, pages 59–84. Springer, 2013.

[24] Juan García-López, José Antonio Rodríguez-Marroyo, Carl-Etienne Juneau, José Peleteiro, Alfredo Córdova Martínez, and José Gerardo Villa. Reference values and improvement of aerodynamic drag in professional cyclists. *Journal of sports sciences*, 26 (3):277–286, 2008.

[25] HC Garner, EW Rogers, WE Acum, and EC Maskell. Subsonic wind tunnel wall corrections (agardograph-109). *Advisory Group For Aerospace Research And Development Neuilly-Sur-Seine (France)*, 1966.

[26] Giuseppe Gibertini and Donato Grassi. Cycling aerodynamics. In *Sport aerodynamics*, pages 23–47. Springer, 2008.

[27] Richard Goldstein. *Fluid mechanics measurements*. CRC Press, 1996.

[28] I Grant. Particle image velocimetry: a review. *Proceedings of the Institution of Mechanical Engineers, Part C: Journal of Mechanical Engineering Science*, 211(1):55–76, 1997.

[29] Frederic Grappe, Robin Candau, Alain Belli, and Jean Denis Rouillon. Aerodynamic drag in field cycling with special reference to the obree's position. *Ergonomics*, 40(12): 1299–1311, 1997.

[30] MD Griffith, T Crouch, MC Thompson, D Burton, and J Sheridan. Elite cycling aerodynamics: Wind tunnel experiments and cfd. In *Proceedings of the 18th Australasian Fluid Mechanics Conference, Tasmania, Australia*, 2012.

[31] Gabor T Herman and Arnold Lent. Iterative reconstruction algorithms. *Computers in biology and medicine*, 6(4):273–294, 1976.

[32] Jacco Hoekstra. *Open Jet Facility Brochure*. TU Delft, Available online at: http://www.lr.tudelft.nl/en/organisation/departments/aerodynamics-wind-energy-flight-performance-and-propulsion/facilities/wind-tunnel-lab/open-jet-facility-hsl/ [Accessed 26 March 2017].

[33] Joe Hoffman. *Chapter 9. Elliptic partial differential equations*, volume 2. McGraw–Hill, ISBN 0-8247-0443-6, 2001.

[34] GM Homsey, H Aref, KS Breuer, S Hochgreb, JR Koseff, BR Munson, and KG Powell. Multi-media fluid mechanics. *AIAA JOURNAL*, 39(6), 2001.

[35] Julian CR Hunt, Alan A Wray, and Parviz Moin. Eddies, streams, and convergence zones in turbulent flows. 1988.

[36] B Melvill Jones. *The measurement of profile drag by the pitot-traverse method*. HM Stationery Office, 1936.

[37] Constantin Jux. Robotic volumetric particle tracking velocimetry by coaxial imaging and illumination. Master's thesis, TU Delft, Delft University of Technology, 2017.

[38] TM Kawamura. Wind drag of bicycles. *Tokyo University, Tokyo, Japan*, 1953.

[39] Shigeo Kida and Hideaki Miura. Identification and analysis of vortical structures. *European Journal of Mechanics-B/Fluids*, 17(4):471–488, 1998.

[40] Václav Kolář. Vortex identification: New requirements and limitations. *International journal of heat and fluid flow*, 28(4):638–652, 2007.

[41] DF Kurtulus, F Scarano, and L David. Unsteady aerodynamic forces estimation on a square cylinder by tr-piv. *Experiments in Fluids*, 42(2):185–196, 2007.

[42] Chester R Kyle. Athletic clothing. *Scientific American*, 254(3):104, 1986.

[43] Chester R Kyle and Edmund Burke. Improving the racing bicycle. *Mechanical engineering*, 106(9):34–45, 1984.

[44] CR Kyle. Wind tunnel tests of bicycle wheels and helmets. *Cycling Science*, 2(1):27–30, 1990.

[45] CR Kyle. Wind tunnel tests of aero bicycles. *Cycling Science*, 3(3):57–61, 1991.

[46] LaVision. Davis software, . URL `http://lavision.de/en/products/davis-software/index.php`.

[47] LaVision. Helium filled soap bubbles generator, . URL `http://lavision.de/en/products/flowmaster/piv-system-components/seeding-devices/index.php`.

[48] LaVision. Programmable timing unit - x, . URL `http://lavision.de/en/products/cameras/programmable-timing-unit-ptu-x/index.php`.

[49] Edzard Mercker and Jochen Wiedemann. On the correction of interference effects in open jet wind tunnels. Technical report, SAE Technical Paper, 1996.

[50] Dirk Michaelis and Bernhard Wieneke. Comparison between tomographic piv and stereo piv. In *Proceedings of the 14th international symposium on applications of laser techniques to fluid mechanics. Lisbon, Portugal*. Citeseer, 2008.

[51] Dirk Michaelis, Christian Poelma, Fulvio Scarano, Jerry Westerweel, and Bernhard Wieneke. A 3d time-resolved cylinder wake survey by tomographic piv. In *12th Int. Symp. on Flow Visualization*, 2006.

[52] Yuichi Murai, Taishi Nakada, Takao Suzuki, and Fujio Yamamoto. Particle tracking velocimetry applied to estimate the pressure field around a savonius turbine. *Measurement science and technology*, 18(8):2491, 2007.

[53] Matteo Novara, Kees Joost Batenburg, and Fulvio Scarano. Motion tracking-enhanced mart for tomographic piv. *Measurement science and technology*, 21(3):035401, 2010.

[54] PK Panigrahi. Particle tracking velocimetry.

[55] RJ Perkins and JCR Hunt. Particle tracking in turbulent flows. In *Advances in Turbulence 2*, pages 286–291. Springer, 1989.

[56] Lewis Griffith Cresswell Evans Pugh. The relation of oxygen intake and speed in competition cycling and comparative observations on the bicycle ergometer. *The Journal of physiology*, 241(3):795, 1974.

[57] Markus Raffel, Christian E Willert, Steven Wereley, and Jürgen Kompenhans. *Particle image velocimetry: a practical guide*. Springer, 2013.

[58] F Scarano. Tomographic piv: principles and practice. *Measurement Science and Technology*, 24(1):012001, 2012.

[59] Fulvio Scarano, Sina Ghaemi, Giuseppe Carlo Alp Caridi, Johannes Bosbach, Uwe Dierksheide, and Andrea Sciacchitano. On the use of helium-filled soap bubbles for large-scale tomographic piv in wind tunnel experiments. *Experiments in Fluids*, 56(2): 42, 2015.

[60] Daniel Schanz, Sebastian Gesemann, Andreas Schröder, Bernhard Wieneke, and Matteo Novara. Non-uniform optical transfer functions in particle imaging: calibration and application to tomographic reconstruction. *Measurement Science and Technology*, 24 (2):024009, 2012.

[61] Daniel Schanz, Andreas Schröder, Sebastian Gesemann, Dirk Michaelis, and Bernhard Wieneke. 'shake the box': A highly efficient and accurate tomographic particle tracking velocimetry (tomo-ptv) method using prediction of particle positions. In *PIV13; 10th International Symposium on Particle Image Velocimetry, Delft, The Netherlands, July 1-3, 2013*. Delft University of Technology, Faculty of Mechanical, Maritime and Materials Engineering, and Faculty of Aerospace Engineering, 2013.

[62] Daniel Schanz, Sebastian Gesemann, and Andreas Schröder. Shake-the-box: Lagrangian particle tracking at high particle image densities. *Experiments in fluids*, 57 (5):1–27, 2016.

[63] Andrea Sciacchitano. *Uncertainty quantification in particle image velocimetry and advances in time-resolved image and data analysis*. PhD thesis, TU Delft, Delft University of Technology, 2014.

[64] Andrea Sciacchitano, Giuseppe Carlo Alp Caridi, and Fulvio Scarano. A quantitative flow visualization technique for on-site sport aerodynamics optimization. *Procedia Engineering*, 112:412–417, 2015.

[65] John C Stover. *Optical scattering: measurement and analysis*, volume 2. SPIE optical engineering press Bellingham, 1995.

[66] Hendrik Tennekes and John Leask Lumley. *A first course in turbulence*. MIT press, 1972.

[67] W Terra, A Sciacchitano, and F Scarano. Evaluation of aerodynamic drag of a full-scale cyclist model by large-scale tomographic-piv.

[68] W Terra, A Sciacchitano, and F Scarano. Drag analysis from piv data in speed sports. *Procedia Engineering*, 147:50–55, 2016.

[69] W Terra, A Sciacchitano, and F Scarano. Aerodynamic drag of transiting objects by large-scale tomographic-piv. In *Proceedings of the 18th international symposium on applications of laser techniques to fluid mechanics. Lisbon, Portugal*. Citeseer, 2016.

[70] Chengxu Tu, Zhaoqin Yin, Jianzhong Lin, and Fubing Bao. A review of experimental techniques for measuring micro-to nano-particle-laden gas flows. *Applied Sciences*, 7 (2):120, 2017.

[71] Milton Van Dyke and Milton Van Dyke. *An album of fluid motion*, volume 176. Parabolic Press Stanford, 1982.

[72] PL Van Gent, D Michaelis, BW Van Oudheusden, P-É Weiss, R De Kat, A Laskari, YJ Jeon, L David, D Schanz, F Huhn, et al. Comparative assessment of pressure field reconstructions from particle image velocimetry measurements and lagrangian particle tracking. *Experiments in Fluids*, 58(4):33, 2017.

[73] Bas W van Oudheusden, Fulvio Scarano, Eric WM Roosenboom, Eric WF Casimiri, and Louis J Souverein. Evaluation of integral forces and pressure fields from planar velocimetry data for incompressible and compressible flows. *Experiments in Fluids*, 43 (2-3):153–162, 2007.

[74] BW Van Oudheusden. Piv-based pressure measurement. *Measurement Science and Technology*, 24(3):032001, 2013.

[75] Verlinden J. Stroober M. Baldewsing R. Van Tubergen, J. Suited for performance: fast full-scale replication of athlete with fdm. In *In Proceedings of SCF '17, Cambridge, MA, USA*, 2017.

[76] Daniele Violato, Peter Moore, and Fulvio Scarano. Lagrangian and eulerian pressure field evaluation of rod-airfoil flow from time-resolved tomographic piv. *Experiments in fluids*, 50(4):1057–1070, 2011.

[77] Jerry Westerweel and Fulvio Scarano. Universal outlier detection for piv data. *Experiments in fluids*, 39(6):1096–1100, 2005.

[78] B Wieneke. Volume self-calibration for stereo-piv and tomographic-piv 7th int. In *Symp. PIV (Rome, Italy)*, 2007.

[79] Bernhard Wieneke. Iterative reconstruction of volumetric particle distribution. *Measurement Science and Technology*, 24(2):024008, 2012.

[80] Norbert Wiener. *Extrapolation, interpolation, and smoothing of stationary time series*, volume 7. MIT press Cambridge, MA, 1949.

[81] Wikipedia. Tour de france records and statistics. URL `https://en.wikipedia.org/wiki/Tour_de_France_records_and_statistics`.

[82] NA Worth and TB Nickels. Acceleration of tomo-piv by estimating the initial volume intensity distribution. *Experiments in Fluids*, 45(5):847, 2008.